Catalysis for CO_2 Activation Reactions with Light Alkanes

Xian Du

St Anne's College, University of Oxford

Supervisor

Prof. Peter P. Edwards FRS ML

A thesis submitted to the Department of Chemistry, University of Oxford for the Degree of Doctor of Philosophy in Inorganic Chemistry

Michaelmas Term 2016

Catalysis for CO_2 Activation Reactions with Light Alkanes

Xian Du, St Anne's College

A thesis submitted to the Department of Chemistry, University of Oxford for the Degree of Doctor of Philosophy in Inorganic Chemistry

Abstract

CO_2, without question, the most famous greenhouse gas, is known to have an increasing concentration in both the atmosphere and oceans. To slow down the pace not only of global warming but also the ocean acidification, several routes are proposed to effectively reduce the net emission of CO_2. Compared to Carbon Capture and Sequestration/Storage (CCS), Carbon Capture and Utilisation (CCU) has much more potential because of the lower costs of scale up and higher profitability to potentially attract capital investment.

Different from the conventional CCU route which is to reduce CO_2 to fuels with hydrogen generated via renewable-energy-driving electricity, two processes are investigated in this thesis; that of Dry Methane Reforming (DMR) and the DeHydrogenation of Propane by CO_2 (DHP by CO_2). The projects on these two processes not only develop catalysts which would be suitable for the reaction performance, but also the ultimate aim is to link the processes with a renewable energy source (in the thesis we chose Solar Thermal Heating). Thermodynamic calculations and process simulations were also evaluated.

The results of DMR unfortunately did not indicate a promising future to link with Solar Thermal Heating due to the very high temperature required during the process. However, the results of thermodynamic calculations and process simulations in DMR project illustrate a good opportunity to utilise flue gas in industry through the so-called Tri- Methane Reforming (TMR). In the DHP by CO_2 process, the catalysts developed were less promising than the ones in DMR due to the severe side-reactions occurred which significantly decreased the selectivity for the desired product. However - and importantly - through our thermodynamic calculations and process simulations, the DHP by CO_2 process has a bright future if the Solar Thermal Heating can be applied with the relative lower temperature requirement, making the CO_2 utilisation process much easier to be fulfilled than DMR.

The work described in this thesis was performed in the Inorganic Chemistry Laboratory, University of Oxford from October 2011 until March 2016, under the complete supervision of Professor Peter P. Edwards. All of the work is my own unless otherwise stated, and has not been submitted previously for any other degree at this or any other university.

Xian Du

March 2016

To my parents, for their kind giving without asking in raising me up;

To every teacher, for the help on making me who I am...

...and to my dearest wife, for her mental company and support during my D.Phil. years.

Acknowledgements

I was nervous when firstly came to Oxford in 2011. It was not only because of the reputation of this world-class university I had heard about from my childhood, but also my research background, Environmental Science, was not 100% fitted with the coming projects which would "afflict" me for 4 years. This feeling got worse because of the delayed first individual meeting with my supervisor - Prof. Peter P. Edwards, and the panic was growing until I heard a kind and gentle voice with warm smile a second later. Throughout the years in PPE group, I have been offered lots of freedom to study the area that I prefer - I will never get self-reliant on my own research without the complete support and full encouragement that Pete has given me. Furthermore, I have enjoyed the time very much when linking my present work to my undergraduate background under his suggestions, and the letter we published together on *The Times* is the happiest experience I have ever had in my life. I feel so grateful because he is always a kind and patient person, sometimes makes me forget about how big his name is in the area of chemistry. In a word, I've learned much more than how to do proper science only in Oxford.

I am highly appreciated to all the friends and colleagues in PPE group, especially Dr. Tiancun Xiao who is looking after the details of my research projects. It is him to push me back to the right track so that I can adapt the pace of research much quicker. I would like to thank my colleagues Zhaoxi Zhang (Ryan) and Xiangyu Jie (Michael) as well - the stimulating and active atmosphere they have created keeps me in the group office to chat in both work and life happily. And I'm grateful to our best supporter, Mrs. Linda Webb, who has given me the world-class assistance on all kinds of documentary issues.

Beyond the quad of Inorganic Chemistry Laboratory where I've been working for more than 4 years, I would like to give my appreciation to everyone at St Anne's College. Many

thanks to our treasury office which offered me their best support on my international conference travelling even though I didn't deserve to this with an off-term application. Many thanks to Prof. Andrew Goodwin, my college tutor, who has organised the Chemistry Christmas Dinner every year for us to have a taste of the NO.1 quality cuisines around Oxford.

And I am highly appreciated to the funding body on my 4-year research in Oxford - the Chinese Scholarship Council. Without the full funding on both my studies and living, it should have been much harder for me to enjoy both research and activities in this university I was dreaming of.

At last, I have to pass my never-enough thanks to my parents who have given me so much during the past 26-year life of mine, and I was feeling sorry every time when not being able to spend my time with them during Chinese New Year. Also, I am most grateful to my wife, and I cannot imagine how to suffer my worst days when lying in hospital during my 2nd year without her care and company.

I am so proud to have the continuous support, encouragement, patience and friendship from every one of you. Thank you!

–Xian Du

–In March of 2016

Contents

List of Figures

List of Tables

Glossary

CCU: CO_2 Capture and Utilisation.

CCS: CO_2 Capture and Sequestration/Storage.

DMR: Dry Methane Reforming.

RWGS: Reverse Water Gas Shift.

SMR: Steam Methane Reforming.

TMR: Tri- Methane Reforming.

DHP: DeHydrogenation of Propane.

ODHP: Oxidative DeHydrogenation of Propane.

DHP by CO_2: DeHydrogenation of Propane by CO_2.

TPD: Temperature Programmed Desorption

Eq.x.y: The numbering y of an equation in Chapter x.

R.x.y: The numbering y of a reaction formula in Chapter x.

$\Delta_r G_m^\theta$**:** Standard change of reaction in Gibbs free energy.

K^θ**:** equilibrium constant of reaction.

$\Delta_r H_m^\theta$**:** Standard molar enthalpy of reaction.

$\Delta_f H_m^\theta$**:** Standard molar enthalpy of formation.

$\Delta_r S_m^\theta$**:** Standard molar entropy of reaction.

S_m^θ**:** Standard molar entropy.

$C_{(p,m)}$**:** Molar heat capacity at constant pressure.

C_i**:** Conversion of substance i (i refers to any reactant in process).

S_j**:** Selectivity of substance j (i refers to any product in process).

Y_j**:** Yield of substance j (j refers to any product in process).

X_i**:** Proportion in volume of i in gas mixture (i refers to any gaseous substance).

B_C**:** Carbon Balance: Percentage of C atoms left in gaseous product mixture after reaction.

B_O**:** Oxygen Balance: Percentage of O atoms left in gaseous product mixture after reaction.

B_H**:** Hydrogen Balance: Percentage of H atoms left in gaseous product mixture after reaction.

Process: Series of reactions in a certain type of reactor.

Sub-reaction: Reaction producing target products and necessary intermediates.

Side-reaction: Reactions generating byproducts.

GHSV: Gas Hourly Space Velocity.

Chapter 1

Introduction

1.1 CO_2 Capture & Utilisation (CCU)

1.1.1 The Big Issue of CO_2

CO_2 is arguably one of the most well-known chemical among people all over the world as the No.1 influential greenhouse gas (GHG).

Apart from the very slow process of photosynthesis in plants, CO_2 is almost invariably at the very end of the energy consumption chain, both in human life and industry. From a thermodynamic perspective, CO_2 absolutely acts as a "bottom line" among the combustion of all kinds of gaseous chemicals [1], which means the conversion of CO_2 to another gaseous compound often requires high temperature to become thermodynamically favoured. The high stability of CO_2 can also be explained by its oxidation state (taken at neutral pH). Figure 1.1 shows the standard Gibbs free energy of formation ($\Delta_f G_m^\theta$) for the carbonaceous substances at different oxidation states of carbon. The gaseous substances (under standard state) are highlighted in red. It is recognised that the gaseous compounds are getting more and more stable as the carbon oxidation state moves from the "middle line" (0 oxidation state) towards either sides of this figure. Moreover, similar trend has been observed among

the liquid and solid carbonaceous substances (in black), which means the carbon oxidation state affects the stability of carbonaceous substances a lot.

There is another trend in Figure 1.1: the gaseous compounds usually have higher $\Delta_f G_m^\theta$ figures than both the liquid and solid substances at the same oxidation states of carbon. Hence, CO_2 is the "bottom line" only in gas phase, and there are liquids (such as oxalic acid) and solids (such as $CaCO_3$) are more stable than CO_2. Based on this, there are indeed some exceptional processes in which the CO_2 conversion is thermodynamically favoured at low temperature (such as $CO_2 + CaO + H_2O \rightarrow CaCO_3 + H_2O$). However, the the production of such CO_2 absorber, taking $CaCO_3$ as an example,usually needs the reverse route by heating limestone ($CaCO_3 \xrightarrow{heat} CaO + CO_2$), which not only requires large quantity of energy but also releases CO_2.

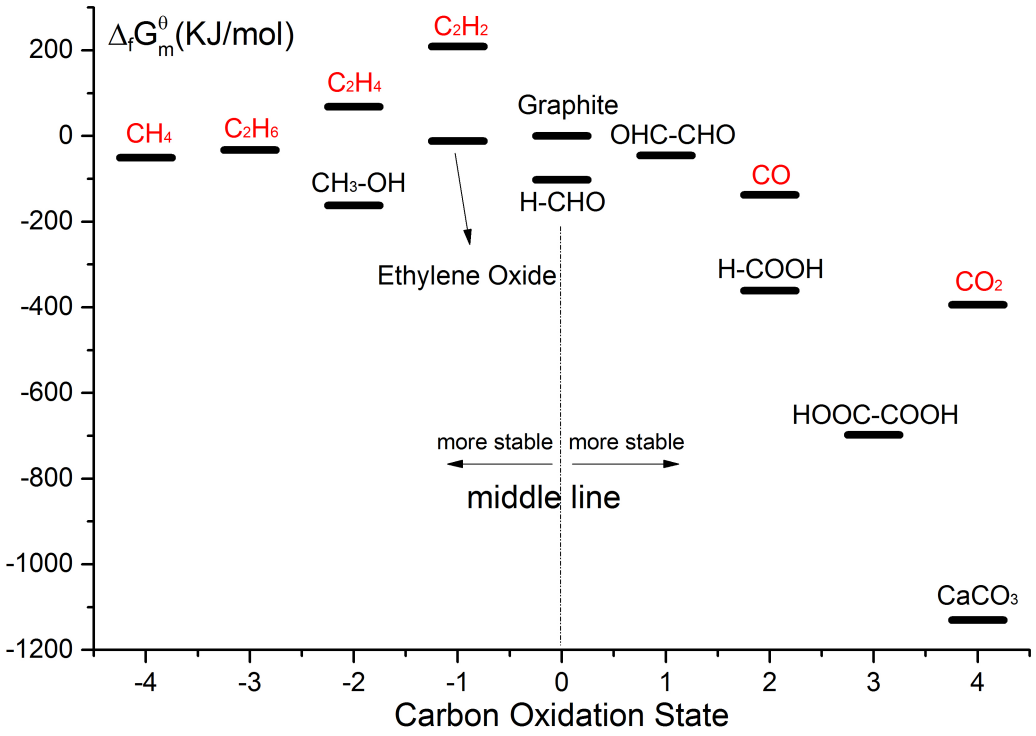

Figure 1.1: Standard Gibbs free energy of formation ($\Delta_f G_m^\theta$) for the carbonaceous substances at different oxidation states of carbon.

Figure 1.2, the $\Delta_r G_m^\theta$ of the reactions between CO_2 and H_2/light alkanes (at 400℃ and normal pressure). One notes, of course, that a ready solution for CO_2 utilisation is its conversion to the more reactive CO via the reverse water gas shift (RWGS, $H_2 + CO_2 \rightarrow H_2O+CO$), and subsequent use of syn-gas chemistry to yield the desired products. However, this attractive route clearly needs a ready source of cheap H_2 - ideally a source of sustainable H_2-derived from non-fossil-fuel routes. In the absence of hydrogen from low (zero) carbon sources, this process will yield a net CO_2 emission for the total wheel-to-wheel analysis. In real world, only about 3.9% of the global demand for H_2 is currently generated from water electrolysis[2], which means the non-fossil-fuel H_2 production will not meet the global H_2 demand for a long time in the future.

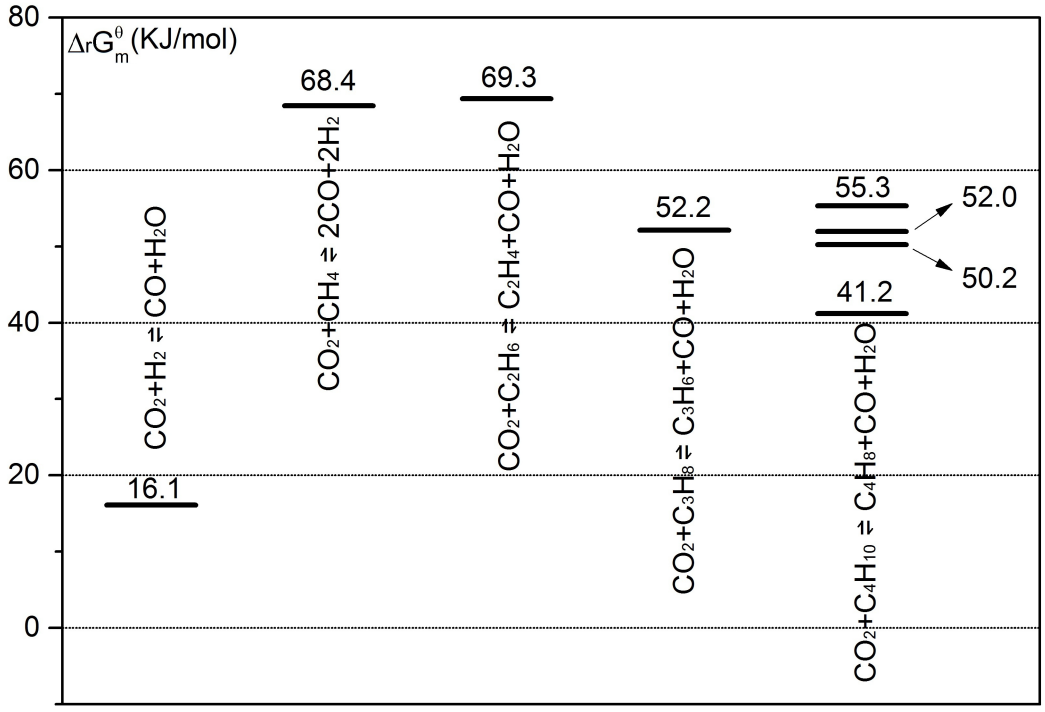

Figure 1.2: $\Delta_r G_m^\theta$ of the reactions between CO_2 and H_2/light alkanes at 400℃ and normal pressure.

Hence, to conclude the discussions above, it is easily assumed that CO_2 will be the ultimate emission if we are still using carbon as the medium to carry the growing demand of energy densely and efficiently.

Figure 1.3 shows the CO_2 concentration in atmosphere which has increased ~2.5% in recent 5 years, and the increase with such rate has been maintained for decades [3]. Besides the apparent exacerbation of the well-known greenhouse effect globally, the concentration of CO_2 in atmosphere can also lead to ocean acidification. The average pH value of oceans has dropped from ~8.179 in the pre-industrial era to ~8.104 in the 1990s [4], and the global average value is even lower at present [5], which means a 28.8% burst of H^+ ion concentration in oceans has arisen through the intensive usage of fossil-fuels. Of course, it does not mean the total diminution of CO_2 from air is always good, and we need certain level of CO_2 kept in the atmosphere or ocean to stabilize the ecosystem - at least, we should slow down the change of environment so that every species can gradually adapt to it.

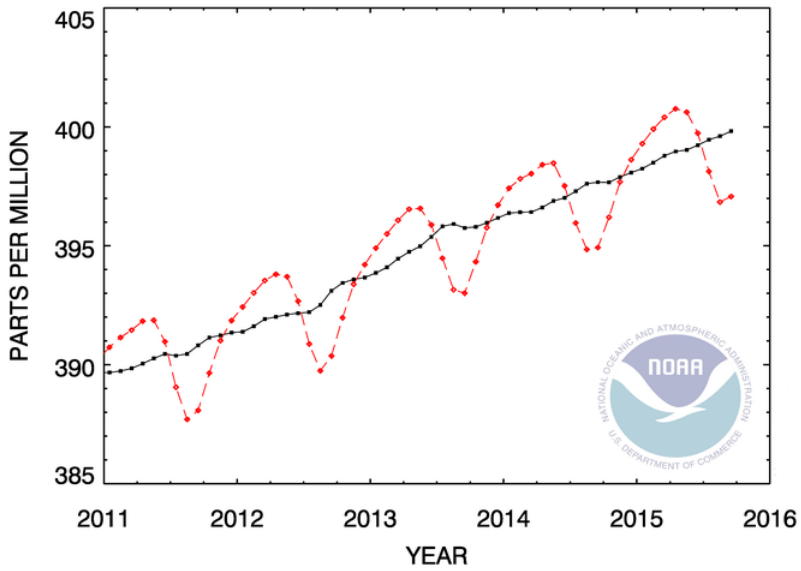

Figure 1.3: Recent global monthly mean of CO_2 concentration in atmosphere. [3]

In addition to the environmental consequences of increasing CO_2 levels, the economic and political ramifications of ever-increasing CO_2 were generally accepted after the famous Kyoto Protocol. From the 1st of April in 2005, CO_2 emission started acting as a price to be traded in market among EU Member States, which can indirectly encourage the countries to slow down the increase of CO_2 emission by developing more carbon-free energy sources. A further goal was raised by the climate negotiators in Cancun, Mexico 5 years ago which was aimed to hold the increase in global average temperatures below 2℃ above pre-industrial levels, and this goal has become the core issue in COP21 held in Paris (21st Annual Conference of Parties of the UN Framework on Climate Change).

We have to say the "2℃-goal" is not a lethal boundary which will kill the planet when the line is slightly crossed, but a simple concept for people to easily understand and hopefully become achievable in reality. According to this, the International Energy Agency (IEA) has calculated that the CO_2 emission must be reduced by 17Gt in 2030 while 39Gt in 2050 to have a 50% chance of achieving this global warming restriction [6].

1.1.2 CCU Versus other Routes of CO_2 Emissions Reduction

With the ultimate goal to cut the concentration of CO_2 in the atmosphere, researchers have claimed several routes, and three of these have attracted the most attention at present are shown in Figure 1.4.

1.1.2.1 Route A, Carbon Capture and Sequestration/Storage (CCS)

Intuitively, the capture and sequestration of CO_2 from, for example, flue gas in plants is the most straightforward route to reduce the net CO_2 emission. It is a route to pump the concentrated CO_2 into a geological site which is usually an exhausted natural gas/oil well or a saline aquifer. Generally, the concentrated CO_2 is compressed and transported via a huge pipeline. SaskPower's "Boundary Dam Power Station" in Canada became operational

in October 2014, which was the first pilot CCS power plant around the world [7]. In this plant, a set of CCS apparatus, occupies ~40% of construction area, was expected to result in a 90% (1Mt/year) reduction of CO_2 emission while the power output of its Unit 3 would be reduced by ~26% (from 139MW to 110MW). However, according to the first financial report released in 2015 [8], the CCS apparatus was estimated to perform only half of the expectation (this is an optimistic estimation and the true value would be much lower). On the other hand, the regular breakdowns and maintenance problems led the unit to only be operational 40% of the time, which means the power loss was much higher than expectation.

1.1.2.2 Route B, Enhanced Hydrocarbon/Oil Recovery (EHR/EOR)

The concept of EHR/EOR is in fact an extension of CCS technology, which is using the concentrated and compressed CO_2 to help mine existing fossil fuels. The mechanism is to supplant gaseous or liquid hydrocarbons with super-critical CO_2. For a long time, it is believed that EHR/EOR is a perfect route to couple the CO_2 mitigation request and economical mining of natural energy reserve. That is why it beats the simple CCS and becomes the major CO_2 emission reduction route in global scale [9].

1.1.2.3 Route C, CO_2 Capture & Utilisation (CCU)

Generally speaking, the utilisation of CO_2 can be regarded as any form of using CO_2 - and the main uses of CO_2 are in urea production, planting (for photosynthesis enhancement), making carbonated beverage and so on. However, in the narrow sense of CCU, researchers have concluded this concept as the applications which can turn CO_2 into long-term-non-degenerating products (such as polymer which lasts in earth for more than 100 years) and short-term-staying products (such as hydrocarbon fuels or other organic chemicals which are ultimately used to release CO_2). So far, apart from the polymer production to sequestrate CO_2 permanently, which may lead to other environmental issues, the CCU is mainly applied

in form of CO_2 reduction by H_2 to hydrocarbons, and the introduction of H_2 gives us a possibility to produce energy storage from CO_2 and renewable energy, which can also meet the request for long-term renewable energy storage[10].

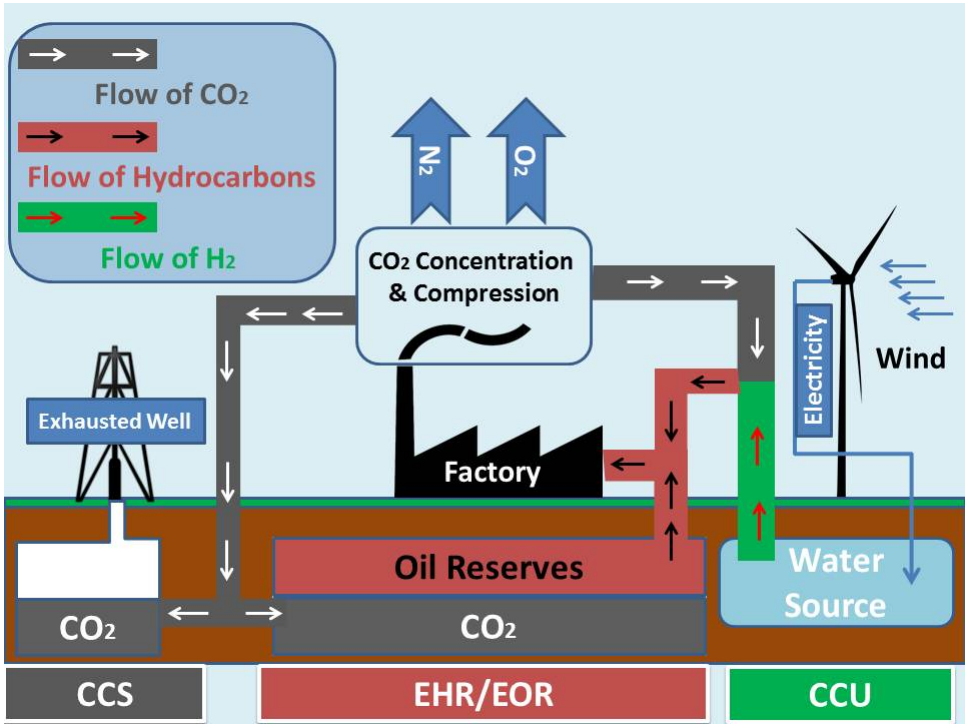

Figure 1.4: Three routes of CO_2 emission reduction. (The production of CCU route is hydrocarbon fuels.)

To compare the net CO_2 emission among the three routes in theory (with the CO_2 emission caused by down-stream production counted), Armstrong and Styring [11] set up a simple model to perform the calculations. In this model, the source of CO_2 was fixed to be collected from the CO_2 concentration and compression, and the amount of sequestrated CO_2 was kept as a constant as $1m^3$ in super-critical state in order to transform the units easier. The results are displayed in Table 1.1, and we can easily find that only CCS can perform a real negative net emission of CO_2, while CCU does not emit extra CO_2 but also more importantly, has no contribution to the mitigation of CO_2 in atmosphere.

Surprisingly, the amount of CO_2 emission caused by recovered products is much larger than the sequestrated CO_2 in EHR/EOR, and this route will not be considered any longer if CO_2 emission reduction displaces the economical profit to be the first principle in high-level decision-makings. (Please note that this calculation does not consider any other CO_2 emissions caused by fossil fuel combustion which is to supply the operational energy.)

Table 1.1: CO_2 net emissions via CCS, EHR/EOR, and CCU routes after using 469kg CO_2 (equal to $1m^3$ super-critical CO_2). (Adapted from Armstrong and Styring. [11])

Routes	Product	CO_2 from product combustion (kg)	Net CO_2 emission (kg)
CCS	No product	0	-469
EHR/EOR	Crude Oil	3051	2582
CCU	$C_{19}H_{40}$	469	0

It is of course understood that the real world would be much more complex than Armstrong and Styring model because the extra consumption of energy and other operational expenses (OPEX) or capital expenses (CAPEX) will further cut down the feasibility of these routes. Taking CCS as an example, despite its effectiveness on net reduction of the CO_2 concentration in the atmosphere, the essential energy cost is nearly 30% of the generated power due to the running of pump and compressor. Furthermore, because of the spatial occupation and huge length of pipeline construction (in SaskPower's "Boundary Dam Power Station", the extra construction occupies nearly 40% of the plant in volume to capture only 1% of the total CO_2 emission.[7]), CCS is not very appealing because there is no real product to motivate payment of any extra bill continuously. On the contrary, CCU may offer economical as well as socio-political reasons for us to develop it. Although we are eager to reduce the CO_2 concentration in the atmosphere, we recognise that the element carbon - in association with hydrogen - is the most effective energy carrier. By producing fuels from CO_2 and H_2 with renewable energy, it is in essence to build up storage of renewable energy with carbon element as a medium, and this kind of storage lasts longer than

any other forms of "energy pool" we have built for holding renewable energy generation.

1.1.3 Two Types of CCU Applications via Renewable Energy

According to previous studies, the concept of CCU can be divided into two major types.

1.1.3.1 Concentrated CO_2 Reacted with Electrochemically Generated H_2 to Fuels

We have to say this is the most accepted route to utilise large quantity of CO_2 via renewable energy source. As displayed in Figure 1.4 above, H_2 is derived from water-splitting using electricity generated by any kinds of renewable energy (such as hydro-, solar-, wind-, geothermal-power and so on. Sometimes nuclear energy is also counted due to its carbon-free nature). The generated H_2 is used to reduce concentrated CO_2, and hydrocarbons or alcohols are produced as the new form of energy storage. The core of this route is to unify all kinds of carbon-free energy sources into electricity, and introduce CO_2 as a carbon source to produce liquid hydrocarbons or alcohols. Compared with on-line electricity or H_2, this energy deposition has higher density and lasts a longer period of time.

The biggest advantages of this route are the simple chemical reactions and large scales, but the drawback is the obvious "energy efficiency" (the ratio between the useful output and input of an energy conversion process). Specht et al. [12] calculated the overall energy efficiency from electricity to methanol formation via chemical and electro-chemical synthesis. The results illustrated that in theory chemical and electro-chemical process can achieve 49.5% and 49% of energy efficiency from electrical power, respectively, and we should cut these numbers massively when considering the low energy efficiency of power generation from renewable energy. For instance, the maximum number of electrical power generation from photo-voltaic (PV) routes is ~20% [13, 14] in converting efficiency while from solar thermal the number is usually between 20%-25% [15]. We must notice that the maximum

number is theoretically computed under perfect conditions and the numbers of average performances are usually much lower. Despite this, the approximate overall energy efficiency, from sunlight to methanol formation, is still much higher than the natural photosynthesis (~1% energy efficiency from sunlight to sugar storage). Hence, it is easy to understand that in nature a complex system with multiple steps often loses more energy than a simpler system, and that is why the idea of coupling simple reaction systems with renewable energy is the core of this research.

One of the main concerns about solar energy utilisation is probably the land usage. Different from the traditional power stations whose capacity is usually decided by how much fossil fuel is burnt, the capacity of a solar power plant (by PV or solar thermal heating) mainly depends on the land area covered by PV cells or sunlight reflectors. The largest solar thermal plant, nowadays in the world, is the Ivanpah Solar Electric Generating System built in the U.S. This plant occupies roughly 5 square miless of land and has a net gross capacity of ~400MW [16]. The PV power stations may occupy even more land than the solar thermal ones. The issue of land usage has given a limitation to the utilisation of solar energy, and the solar power plants can only be settled around (or in) the dessert land where there is abundant sunshine and abundant cheap land.

1.1.3.2 Direct Utilisation of CO_2 with Light Hydrocarbons under Solar Thermal Heating

Coupling CO_2 utilisation with a solar thermal heating system is relatively less reported compared to the electricity-derived CO_2 reduction by H_2.

Solar energy is probably the only renewable energy source that easily achieve medium or high temperatures for chemical process. It has been reported that the operating temperature can reach to as high as 2000℃ by concentrating sunlight, and an annual average collection efficiency up to 45% has also been reported [17]. Furthermore, with solar power

generation in form of electricity as comparison, the capital expenses (CAPEX) of solar thermal heating is lower and the technologies are simple with less maintenance than photovoltaic routes. The drawback of solar thermal heating is as obvious as its advantages: we cannot control the solar radiation or weather to be always bright, in other words, sunlight is intermittent, and this makes it impossible for a solar heating system to perform constantly at high level.

So the key to the solar thermal heating systems would be to maintain the energy output constantly and continuously, and it has been reported to be applicable with Latent Heat Storage (LHS) technology [18]. LHS uses a phase-change material (PCM) to gather the energy from sunlight during the melting of solid, and the advantages of LHS are as follows:

(1), large energy density storage, which means a relatively continuous energy output;

(2), constant-temperature heat source;

(3), easily regenerated.

Hence, LHS makes it possible for a chemical process to be operated under a constant temperature from a solar thermal heating system. Of course we can take after-process heat into consideration if the temperature is still high enough to run a generator but that will not be discussed in detail is my thesis.

1.2 A Brief Introduction to Catalysis

A catalyst accelerates a chemical reaction. It does so by forming bonds with the reacting molecules, and by allowing these to react to a product, which detaches from the catalyst, and, in theory if not always in practice, leaves it unaltered such that it is available for the next reaction. [19] In fact, the catalyst can be described as a participant of a cyclic reaction to improve the rate, and it is recovered in its original form at the end of the cycle.

1.2.1 How Catalysis Accelerates the Reaction

The reaction coordinate diagram in Figure 1.5 illustrates how the catalyst accelerates the reaction. For reaction $A + B \rightarrow P$, P is at a lower total energy than A+B. So this is an exothermic reaction and should be favourable from an energy standpoint. The energy difference between A+B and P is the overall change in free energy (ΔE) in the diagram. However, before reaching to P, some energy is required for A+B to firstly convert to a transition state which is the point of highest energy between the reactants and products, and this energy is called the activation energy (ΔEa).

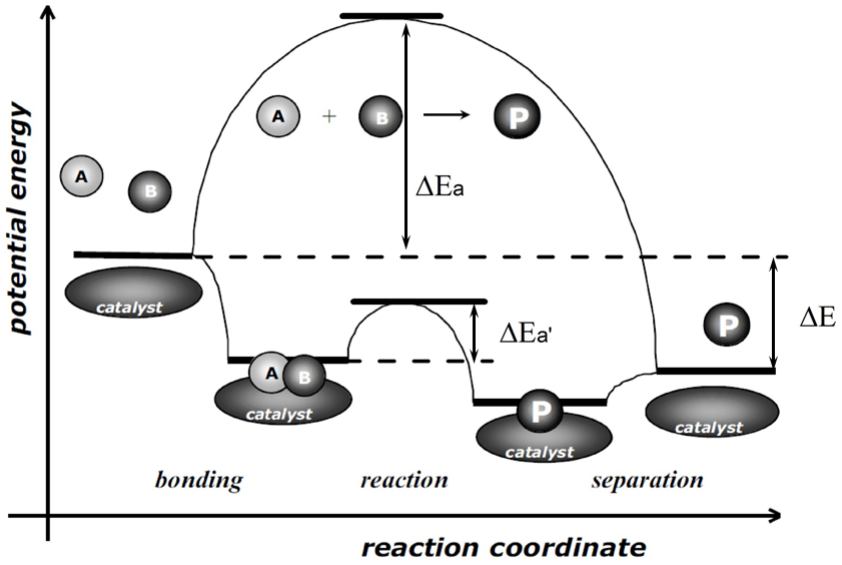

Figure 1.5: Reaction Coordinate Diagram of $A + B \rightarrow P$. [19]

The catalysed reaction $A + B \rightarrow P$ starts by bonding of the reactants A and B to the catalyst, which is spontaneous/exothermic. There then follows the reaction between A and B while they are bound to the catalyst. This step is associated with an activation energy

(ΔEa') which is significantly lower than that for the uncatalysed reaction. Finally, the product P separates from the catalyst in an endothermic step. The rate of the reaction depends on the height of the activation energy, and hence the catalysed route must have a higher rate than the uncatalysed one due to the much lower activation barrier. The catalyst offers an alternative path for the reaction, which is obviously more complex, but energetically much more favourable. On the other hand, the ΔE for the catalytic reaction equals that of the uncatalysed reaction. Hence, the catalyst does not affect the equilibrium for the overall reaction. Thus, if a reaction is thermodynamically unfavorable, a catalyst cannot change this situation – catalysts change the kinetics but not the thermodynamics.

In general, the catalysis can be divided into two major categories: the homogeneous catalysis and the heterogeneous catalysis, and in this thesis we are only discussing the heterogeneous one.

Usually in heterogeneous catalysis, a solid state material acts as the catalyst to accelerate the reactions of molecules in gas or solution. As the catalytic reactions often occur at the surface of solids, we can change the text in Figure 1.5 from "bonding and separation" to "adsorption and desorption". To be noticed, it is not necessary for all the reactants to be attached on catalyst surface before being activated to the transition state, and sometimes there is only one or part of the reactants adsorbed while the others are still left in the gas phase or solution.

1.2.2 Thermodynamics and Kinetics of Reactions

Thermodynamic and kinetic studies are in essence two different perspectives for learning the relationships between "the motion of matter" and "the transfer of energy". [20]

For a chemical reaction under certain conditions (such as temperature, pressure and so on), thermodynamics can tell people the theoretical potential (an unachievable limit) of this reaction - regardless of how long it would take the reaction from initial state to

achieve the equilibrium state; while the kinetic studies are mainly focused on the rate of this reaction with/without a typical catalyst. It is obvious that the activation energy (ΔEa/ΔEa' as shown in Figure 1.5) is dependent on the use of catalyst, and hence the kinetic study results changed as the catalyst changed, which is different from the generic results of thermodynamic studies for a reaction.

The equilibrium constant (K^θ) and rate constant (k) are the keys to the studies of thermodynamics and the kinetics respectively. Both K^θ and k are linked to the concentrations of reactants and products, and they are correlated under the equilibrium state. For a reversible reaction $A \rightleftharpoons B$ at equilibrium state, there is:

$$K^\theta = \frac{k_{A\to B}}{k_{B\to A}} = \frac{[B]_{eqm}}{[A]_{eqm}} \quad \text{.....Eq.1.1}$$

in which the $k_{A\to B}$ and $k_{B\to A}$are the rate constants of reaction $A \to B$ and $B \to A$ respectively. $[A]_{eqm}$ and $[B]_{eqm}$ are concentrations of reactant A and B at equilibrium state.

1.2.3 Rate Laws in Reaction Kinetics

According to the law of mass action, the rate of a chemical reaction at a constant temperature depends only on the concentrations of the substances that influence the rate. The substances that influence the rate of reaction are usually one or more of the reactants, but can occasionally include products. Catalysts, which do not appear in the balanced overall chemical equation, can also influence reaction rate. The rate law is experimentally determined and can be used to predict the relationship between the rate of a reaction and the reactant concentrations.

1.2.3.1 Rate Laws for Elementary Reactions

The basic knowledge of rate laws are adapted from the book: *Reaction Kinetics* [21].

For an elementary reaction (a chemical reaction in which chemical species react directly to form products in a single reaction step and with a single transition state) $aA+bB+\ldots \rightarrow products$, the rate law is given as follows:

$$r = k\,[A]^{\alpha}\,[B]^{\beta}\,\ldots\ldots\ldots\ldots\ldots\ldots\textbf{Eq.1.2}$$

in which the "r" is the reaction rate, and the "k" is called the rate constant. [A] and [B] are the concentrations of reactant A and B respectively. The exponents "α" and "β" , called the orders of the reaction with respect to that reactant, are usually (but not always) integers and have no relation to the coefficients "a" and "b" in the reaction formula. If "p" is the sum of the exponents ($p = \alpha + \beta + ...$), then "p" is called the overall order of this reaction.

Table 1.2 displays four of the simplest rate laws in both their differential and integrated form. The above $[A]_0$ and $[B]_0$ in this table represent the initial concentrations of reactant A and B. The differential form indicates the relationship between reaction rate and reactant concentrations, whilst the integrated form reveals the the relationship between reactant concentrations and reaction time.

Table 1.2: Rate laws for simplest elementary reactions both in differential and integrated form.

Reaction	Overall Order	Differential Form	Integrated Form
$A \rightarrow P$	Zeroth	$r = \frac{d[A]}{dt} = -k$	$[A] = [A]_0 - kt$
$A \rightarrow P$	First	$r = \frac{d[A]}{dt} = -k[A]$	$ln[A] = ln[A]_0 - kt$
$A + A \rightarrow P$	Second	$r = \frac{d[A]}{2dt} = -k[A]^2$	$\frac{1}{[A]} = \frac{1}{[A]_0} + 2kt$
$A + B \rightarrow P$	Second	$r = \frac{d[A]}{dt} = \frac{d[B]}{dt} = -k[A][B]$	$kt = \frac{1}{[B]_0 - [A]_0} \cdot ln\frac{[B]_0[A]}{[A]_0[B]}$

1.2.3.2 Rate Laws for Complex Reactions

In kinetics, a complex reaction simply means a reaction whose mechanism comprises more than one elementary step (or say multiple transition states). Hence the rate law of a complex reaction is in essence the combination of rate laws for multiple elementary reactions.

The types of complex mechanisms include consecutive reactions; reversible reactions, pre-equilibria; uni-molecular reactions, and so on. Here in the thesis, only the simplest scheme, a consecutive reaction, is discussed in details to reveal how the rate laws for a complex reaction are derived from the rate laws for the elementary reactions.

The simplest scheme of the complex reaction consists of two consecutive, irreversible elementary steps: $A \xrightarrow{k_1} B \xrightarrow{k_2} C$. Both steps are first order reactions.

In this situation, the relation among the concentrations of A, B and C is always:

$$[A] + [B] + [C] = [A]_0 \quad \textbf{Eq.1.3}$$

and the rate equations for [A], [B] and [C] are:

$$\frac{d[A]}{dt} = -k_1[A] \quad \textbf{Eq.1.4}$$

$$\frac{d[B]}{dt} = k_1[A] - k_2[B] \quad \textbf{Eq.1.5}$$

$$\frac{d[C]}{dt} = -k_2[B] \quad \textbf{Eq.1.6}$$

Integrating **Eq.1.4** gives:

$$[A] = [A]_0 \cdot e^{-k_1 t} \quad \textbf{Eq.1.7}$$

Substituting **Eq.1.7** into **Eq.1.5** gives $\frac{d[B]}{dt} + k_2[B] = k_1[A]_0 \cdot e^{-k_1 t}$, and the solution of this differential equation is:

$$[B] = \frac{k_1}{k_2 - k_1} \cdot (e^{-k_1 t} - e^{-k_2 t}) \cdot [A]_0 \quad \textbf{Eq.1.8}$$

Finally, from **Eq.1.3** we can find $[C] = [A]_0 - [A] - [B]$, and:

$$[C] = (1 + \frac{k_1 e^{-k_2 t} - k_2 e^{-k_1 t}}{k_2 - k_1}) \cdot [A]_0 \quad \textbf{Eq.1.9}$$

Kinetic study is complex and dependent on other reaction conditions (such as the influences from catalysts), and the overall orders of the complex reactions are usually carried out by practical experimental data. In the following chapters, the reaction orders are the kinetic study results from other researchers. The main parts of the carried-out results in this thesis are still showing the thermodynamic calculations for CO_2-utilising reaction complexes and the results from the experimental catalysis which are demonstrated by thermodynamic results.

1.3 Catalytic Activation and Utilisation of CO_2 by Reactions with Light Hydrocarbons

In this section, two different processes for CO_2 utilisation are introduced – dry methane reforming (DMR) and dehydrogenation of propane by CO_2 (DHP by CO_2). Both processes have attracted much popularity in recent years with potential to effectively reduce CO_2 and produce valuable products.

1.3.1 Dry Methane Reforming (DMR)

As a part of Tri- Methane Reforming (TMR), DMR (**R.1.1**) is highly promising and frequently discussed in recent years. Utilising CO_2 and CH_4 as chemical feedstocks would seem to be a perfect solution for all the problems above [22]. Mostly, what we call methane reforming is Dry Methane Reforming wherein CO_2 and CH_4 react to synthesis gas or syn-gas (CO and H_2) [23].This reaction is strongly endothermic and runs according to the following equation.

$$CO_2 + CH_4 \rightleftharpoons 2CO + 2H_2 ....\mathbf{R.1.1}$$

$$(\Delta H^{\theta}_{298K} = +247KJ/mol)$$

This reaction is equally favored by low pressure but requires high temperature. A Reverse Water Gas Shift (RWGS, **R.1.2**) reaction occurs as a side reaction:

$$CO_2 + H_2 \rightleftharpoons CO + H_2O \quad \text{....}\mathbf{R.1.2}$$

$$(\Delta H^{\theta}_{298K} = +41KJ/mol)$$

The dry reforming process provides several advantages compared to Steam Methane Reforming (SMR, **R.1.3**), and the most important one is the production of synthesis gas with a low H_2/CO ratio, which is suitable for use in Fischer–Tropsch synthesis for higher hydrocarbons. (In a stoichiometric reaction, the H_2/CO ratio of DMR production is 1:1 while the one of SMR production is 3:1.)

$$H_2O + CH_4 \rightleftharpoons CO + 3H_2 \quad \text{....}\mathbf{R.1.3}$$

$$(\Delta H^{\theta}_{298K} = +206KJ/mol)$$

1.3.1.1 Reaction Mechanisms

The mechanism of heterogeneously catalysed gas-phase reactions can be described by the sequence of elementary reaction steps, including adsorption and desorption of the species, surface diffusion and chemical reaction of the adsorbed species. There are two different models to describe the bi-molecular surface reaction mechanism: the Langmuir-Hinshelwood mechanism and the Eley-Rideal mechanism[24] (displayed in Figure 1.6). In the Langmuir-Hinshelwood model, the rate of the heterogeneous reaction is controlled by the reaction of adsorbed molecules, and that all adsorption and desorption pressures are in equilibrium. The rate expression can be derived to be a function of surface coverage of adsorbed species on the surface; while the Eley-Rideal one assumes that only one of the molecules adsorbs and the other react with it directly from the gas phase, without adsorbing.

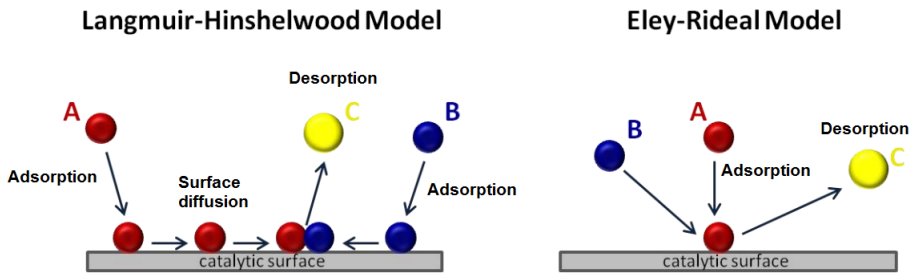

Figure 1.6: Schematic Diagram of the Langmuir-Hinshelwood and the Eley-Rideal Models. [24]

Both of the two models have been proposed when discussing the mechanism of DMR reaction. The general opinion is that methane is adsorbed, activated and dissociated on the surface of reduced metal catalyst first. The disagreement centres on whether CO_2 also dissociates on the surface of catalyst.[25–28]

Takayasu et al. [25] suggested that gaseous CO_2 directly reacts with hydrogen formed from methane to water. Steam reforming then followed to obtain synthesis gas. That is to say, the substance of dry reforming is the same as steam reforming.

Erdöhelyi et al. [26] proposed the mechanism of CO_2 reforming with methane over supported noble metal catalysts on the basis of kinetic studies. Methane may undergo two reactions as following routes: (1) step-wise dehydrogenation followed by the surface reaction with surface oxygen or $-OH$ to CO and H_2, (2) or direct reaction with surface oxygen species to CH_x then following the former route. CO_2 may react with adsorbed hydrogen, surface carbon and surface CH_x fragments.

The mechanism of CO_2 reforming with methane may change when different types of catalysts are used. Tsipouriari and co-workers [29] proposed a mechanism that when doing a partial oxidation of methane over a Ni/La_2O_3 catalyst, only carbonate species are formed over La_2O_3 at elevated temperatures. His co-worker Zhang [27] did the DMR reaction over

the same catalyst and found CO_2 is preferred to being absorbed on the surface of La_2O_3 rather than nickel.

Yan and co-workers [28] reported that the decomposition of methane on a nickel catalyst could result in the formation of at least three kinds of surface carbon species on supported nickel catalyst. These carbonaceous species can be described as: completely dehydrogenated carbidic C_α type, partially dehydrogenated $CH_x(1\leq x\leq 3)$ species, namely C_β type, and carbidic clusters C_γ type formed by the agglomeration and conversion of C_α and C_β species under certain conditions. C_α type was mainly hydrogenated to methane even below 500K, which is responsible for CO formation. A significant amount of surface carbon species which is assigned to partially dehydrogenated C_β were hydrogenated to methane below 600K. The majority of the surface carbon was hydrogenated above 800K and was attributed to carbidic clusters C_γ. The possible reaction processes of CO_2 reforming with methane was inferred as follows: methane is firstly decomposed into hydrogen and different surface carbon species, then the adsorbed CO_2 reacts with surface carbons to form CO.

Hence, the proposed mechanism of methane dry reforming is as following [28]:

1), Dissociative adsorption of methane (the rate-determining step)

$$CH_{4(g)} \rightarrow CH_{4(ad)} \rightarrow CH_{x(ad)} + (4-x)H_{(ad)} \rightarrow C_{(ad)} + 4H_{(ad)} \ldots . \mathbf{R.1.4}$$

2), Dissociative adsorption of CO_2

$$CO_{2(g)} \rightarrow CO_{2(ad)} \rightarrow CO_{(ad)} + O_{(ad)} \rightarrow C_{(ad)} + 2O_{(ad)} \ldots . \mathbf{R.1.5}$$

3), Formation of water

$$2H_{(ad)} + O_{(ad)} \rightarrow H_2O_{(ad)} \rightarrow H_2O_{(g)} \ldots . \mathbf{R.1.6}$$

4), Formation of hydrogen

$$2H_{(ad)} \rightarrow H_{2(ad)} \rightarrow H_{2(g)} \ldots . \mathbf{R.1.7}$$

5), Formation of carbon monoxide and decarbonation

$$CO_{2(ad)} \rightarrow CO_{(g)} \rightarrow C_{(ad)} + O_{(ad)} \rightarrow CO_{2(ad)} \rightarrow CO_{(g)} \ldots . \textbf{R.1.8}$$

1.3.1.2 Selection of Metals in Catalyst Preparation

In relation to catalysts in DMR, an ideal catalyst should lower the temperature and pressure in this reaction and also should have high resistance to side effects.

Catalysts may deactivate due to a sintering effect [30], coking effect and sulfur poisoning [30, 31]. Coking is the common side effect during the DMR reaction. It makes a carbon deposit both via the Boudouard reaction (**R.1.9**) and methane cracking (**R.1.10**) [32, 33].

$$2CO \rightleftharpoons CO_2 + C \ldots . \textbf{R.1.9}$$

$$CH_4 \rightleftharpoons 2H_2 + C \ldots . \textbf{R.1.10}$$

Both of the two reactions above can be catalytically activated by some metallic compounds which are also catalysts for DMR reaction. Hence the resistance to coking is very important in judging the stability of a certain catalyst.

DMR was intensively investigated in the last two decades and the results were frequently improved in order to obtain a high conversion and long-term stability against coking. The main results are for carbide, oxide and nitride based catalysts whose metal elements are mainly from Group-VIII such as Ni [34, 35], and other transition metal groups such as Co, Mo and so on [36, 37].

Nickel-containing catalysts are perfect to pursue a high conversion but also need high ignition temperatures (>850℃) and are subject to sintering and coking effects [38]. To avoid coking, some noble metals such as Au, Pd, [39, 40] are introduced to make metallic or bimetallic catalysts. Guczi and co-worker [39] made a gold modified $Au - Ni/MgAl_2O_4$ and got no observable graphite or CMWNT(carbon deposit and carbon nanotubes) on it

after the DMR reaction. Steinhauer and co-workers [40] did a series of DMR reactions over catalysts under different Ni/Pd ratios and reached to a best conversion when using a $7.5wt\%$ supported catalyst. However, with a good result in coking resistance, the cost of noble metals is very high.

Co, Mo, W containing bimetallic catalysts were discovered to have a good result both in conversion and coking resistance with a relatively low price and this kind of catalyst has become very popular during the last 2 decades [41, 42].

1.3.1.3 Supported Metal Carbide Catalysts

Besides the selection of metals, there are two popular topics also attracting researcher's attention in the field.. With a special structure that carbon atoms are dispersed among metal atoms, the total structure of metal is changed without any cutting down of electrical conductivity. Metal carbide is a relatively later-studied catalyst for DMR, and it can strengthen the structural stability with no apparent negative effects on conversion. York et al. [43] studied the DMR reactions over molybdenum and tungsten carbide with a comparison with some noble metal catalysts. The results showed that β–Mo_2C has an activity for dry reforming comparable to that of $5wt$ and $5wt\%Rh/Al_2O_3$ and the price is much lower than the noble metal. York's co-worker Claridge [44] also concluded the reason why the activity of WC is considerably lower than β–Mo_2C, is probably due to the lower surface area of the tungsten carbide ($\alpha - WC = 39m^2/g$; $\beta - Mo_2C = 91m^2/g$), and also may be partly due to the difficulty in obtaining high chemisorption for α-WC samples, as reported by Ribeiro and co-workers previously [45].

The role of the support in the catalytic process is another popular topic.

Erdöhelyi and his co-workers have done DMR reactions over a series of supported Pd catalysts (TiO_2, Al_2O_3, SiO_2, and MgO) [46]. The conclusion summarised that the CH_4 decomposition occurs at 773K to give H_2 and CO_2 dissociation occurs at elevated temper-

ature and showed a significant support effect on Pd/TiO_2 and Pd/Al_2O_3. Supported Pd carbides were active in the high temperature in DMR with very little carbon deposition. In addition, the order of activity of the catalysts on different supports, based on the turnover frequency(TOF), is $Pd/TiO_2 > Pd/Al_2O_3 > Pd/SiO_2 > Pd/MgO$.

Basini and Sanfilippo [47] also carried out similar research on the DMR reactions over different metals on various supports. The results showed that based on the TOF, the activity per metal atom was Rh≈Ru>Ir, and for the supports, $Al_2O_3 > La_2O_3 > CeO_2 > MgO > TiO_2$.

Steinhauer [40] also carried out a comparison of DMR reactions over different supports when changing the ratio of Ni/Pd. The result showed that the catalytic activity of the studied $Ni - Pd$ catalysts depends strongly on the support used and decreases in the following ranking: $ZrO_2 - La_2O_3 > La_2O_3 > ZrO_2 > SiO_2 > Al_2O_3 > TiO_2$,which showed a huge difference compared with the two results above.

The author thinks the reason of the huge difference is partially due to the nature of the supports and metals and, what is more, the structural properties such as surface area decide the chemisorption abilities, and the chemisorption may have a great influence to the TOF of catalysts.

In recent years, supported carbides are becoming more prominent because the support can improve both the efficiency and stability of carbide in the DMR reaction by changing its structure and surface area [48, 49]. Darujati et al. tested the stability of supported and promoted Mo_2C catalysts in dry methane reforming. The results showed that low surface area MgO and α-Al_2O_3 were ineffective supports for Mo_2C catalysts in dry reforming applications, while higher surface area ZrO_2 and γ-Al_2O_3 were more effective. In addition, γ-Al_2O_3 showed a higher thermal stability than ZrO_2 even though deactivation via oxidation also occurred. It was also found that the higher loading of Mo_2C can lead to a higher activity and this is because of strong interactions between Mo_2C and Al_2O_3 at higher Mo

loading, forming a Mo_2C mono-layer, which results in a higher Mo_2C dispersion.

Raskó [50] carried out FT-IR studies on the adsorption of CO and CH_3 on silica-supported MoO_3 and Mo_2C catalysts. The spectrum of Mo_2C/SiO_2 shows that polymeric carbon was formed on the catalyst's surface during preparation step; the spectrum of CO adsorbed on Mo_2C/SiO_2 is very similar to that obtained on supported Group-VIII metals, which may indicate that silica-supported Mo_2C has a noble metal-like character in CO adsorption; ethylene was clearly observed in the gas phase product, which indicated that Mo_2C is the active surface component on Mo-containing catalysts in converting of methane into ethylene; the thermal stability of $CH_{3(ad)}$ shows marked differences to MoO_3/SiO_2 and Mo_2C/SiO_2, respectively. The IR band due to $CH_{3(ad)}$ started to disappear at 373K on Mo_2C/SiO_2, while on MoO_3/SiO_2 appreciable disappearance of this band could be observed only from 473 K. The temperatures of complete elimination of the band due to $CH_{3(ad)}$ were 573K on Mo_2C/SiO_2 and 673K on MoO_3/SiO_2. Isothermal experiments performed at 423K revealed that the extent of $CH_{3(ad)}$ disappearance is 1.5–2 times higher on Mo_2C/SiO_2, than on MoO_3/SiO_2. From the above findings we can state that $CH_{3(ad)}$ species are less stable (more reactive) on Mo_2C/SiO_2.

Naito et al. studied the mechanistic differences in the CO_2 reforming of methane over unsupported and zirconia supported molybdenum carbide catalysts [51]. Besides the fluid reaction in a $CH_4 : H_2$=1:1 gas flow, the isotopic exchange reaction of CH_4 and CD_4 was carried out over Mo_2C/ZrO_2 catalysts after the carburisation of MoO_3/ZrO_2 in a closed gas circulation system with the same procedure as the flow system, and the products were analysed by quadrupole mass spectrometer. The results showed (in Figure 1.7) that in the initial reaction, unsupported Mo_2C showed a high conversion at the very beginning but it dropped in the short term which means a low stability. In contrast, 1wt% loading supported catalyst had a very good stability but with a low conversion throughout the whole process; only 1wt% loading supported Mo_2C can combine the stability and activity

in a good level. This implied that a support can strengthen the stability of carbide but over supported carbide may reduce conversion.

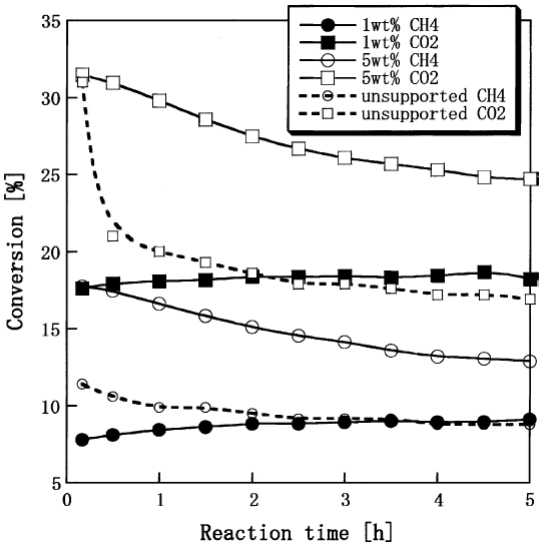

Figure 1.7: Time courses of CH_4–CO_2 reaction over unsupported Mo_2C and 1 and 5wt at 1123K ($CH_4 : CO_2 = 1 : 1$). [51]

To investigate the reason for this, the XPS analysis showed a difference in the binding energy $Mo3d5/2$ and $Mo3d3/2$ transitions which shifted during the reaction process on supported and unsupported Mo_2C (shift occurred on the unsupported Mo_2C which indicated the oxidation of Mo_2C). This result indicated a strong electronic interaction between Mo_2C and ZrO_2 on the fresh Mo_2C/ZrO_2 catalyst, which is disturbed little by the CH_4–CO_2 reaction. A CH_4–CD_4 isotopic exchange reaction was carried out over unsupported and supported catalysts. The initial rates of CH_3D formation are listed in Table 1.3 at various reaction temperatures. It is necessary to notice that, the data adapted from the original research paper are carried out with both different loading levels and different reaction temperatures, and the results under multiple variables are usually incomparable. However, the reaction results can still imply that by dispersing on ZrO_2, the CH_4 dissociation ability of molybdenum carbide is diminished significantly because of the strong

electronic interaction with ZrO_2 (the supported samples have much lower initial rates of CH_3D formation than the unsupported Mo_2C although the reaction temperatures are much higher). All the results above explained the phenomena that over supported carbides lose their activity significantly.

Table 1.3: Initial rates of CH_3D formation in CH_4–CD_4 isotopic exchange reaction over unsupported and ZrO_2 supported Mo_2C catalysts at various temperatures [51]

Catalysts	Reaction Temperature (K)	Initial rates of CH_3D formation (mol/min)
Unsupported Mo_2C	373	3.4×10^{-7}
$5wt\%Mo_2C/ZrO_2$	473	1.6×10^{-7}
$1wt\%Mo_2C/ZrO_2$	793	1.9×10^{-7}

The stability of catalyst was measured in another way which changed the ratio of CH_4/CO_2 to 1:3 and 3:1 to do a comparison. The results showed that 1wt% loading catalyst can be more stable in a $CH_4 : CO_2 = 1 : 3$ gas flow than in the one whose $CH_4 : CO_2$ ratio is 3:1. According to this result, Naito and co-workers proposed that the mechanism of deactivation may be the inactive carbon accumulation because CH_4 decomposition is the rate determining reaction in the whole process which may produce a high carbon deposition with a high $CH_4 : CO_2$ ratio. This mechanistic conclusion was quite different from Green and co-worker's conclusion which is the oxidation on unsupported Mo_2C that deactivates the catalyst [44]. Naito also explained that it is because the CO_2 can be adsorbed on the vicinity of carbide and support which leads to the difference in properties and performance.

1.3.2 Historical Research of Propane Dehydrogenation to Propylene

Propylene is probably the second most important organic chemical feedstock, which is behind ethylene only, in the petrochemical industry for production of poly-propylene, acrolein, acrylic acid, glycerin and so on. At present, propylene is mainly produced via fluid catalytic cracking (FCC) of petroleum or naphtha steam-cracking [52]. However, the propylene production is not only limited by the ethylene/propylene ratio in the product of petroleum

FCC process but also competitively inhibited by the usage of light alkane to gasoline with higher octane-number, and the supply and demand of propylene have been unbalanced. Hence, to open a new and reliable route for propylene production is becoming more and more desirable.

Propane is probably an attractive future alternative to propylene production, but so far it has not been fully used like methane as an abundant natural resource. As mentioned by Zhang et al. [53], more than 6% of volume is in associated petroleum gas (APG) when directly extracted from and oilfield, and this ratio could reach to 15% if we turn to the wet gas (or wet natural gas). Moreover, this ratio will be increased to more than 60% in volume if any Liquid Petroleum Gas (LPG) is produced from petrochemical industry. However, unfortunately, the current usage of propane seems to generate heat via immediate combustion both in life and industry, which is a terrible waste.

The Dehydrogenation of Propane to produce propylene (DHP, $C_3H_8 \rightarrow C_3H_6 + H_2$) was firstly discussed in 1955 by Kearby et al. [54] Chen et al. did a kinetic study over $Pt-Sn/Al_2O_3$ catalysts and claimed that the mechanism of this reaction could be separated in 3 steps (footnote "ad" means adsorbed):

(1) Propane is adsorbed on catalyst surface;

$$C_3H_8 \rightarrow C_3H_{8(ad)} \ldots . \textbf{R.1.11}$$

(2) C-H bond of adsorbed propane is cracked to form C_3H_7 and C_3H_6 with the help of catalyst;

$$C_3H_{8(ad)} \rightarrow C_3H_{7(ad)} + H_{(ad)} \rightarrow C_3H_{6(ad)} + H_{2(ad)} \ldots \textbf{R.1.12}$$

(3) Generated propylene and H_2 are desorbed from catalyst surface.

$$C_3H_{6(ad)} \rightarrow C_3H_6 \ldots . \textbf{R.1.13}$$

$$H_{2(ad)} \rightarrow H_2 \ldots . \mathbf{R.1.14}$$

Through the decades till now, the catalysts for this process have been systematically developed. When selecting the elements for catalyst design, Cr-based and Pt-based catalysts doped on various supports appear to be the most popular catalyst series. However, both of Cr-based and Pt-based catalysts can hardly be kept at high level of catalytic performance long term due to the rapid coke formation which might be caused by large amount of acid sites formed naturally on the catalyst surface. Although we can find papers reporting that Pt-based catalysts can be promoted by Sn and Cu additives to enhance the coke resistance [55, 56], the price of Pt has decided that this series could never be applied to the industry unless the lifetime or the regeneration of catalysts can be improved during the reactions.

In recent years, Liu et al. [57–59] introduced ordered mesoporous carbon (OMC) catalysts without any metallic doping into this process and achieved significant improvement, and this material has been proved to solve the problem of coking which is fatal over Cr-based and Pt-based catalysts. Through the XPS oxygen 1s spectra of samples, the mechanism had been attributed to the existence of ketonic C=O species on the OMC's surface. During the DHP:

(1) Ketonic C=O acted as the electron donor to activate the C-H bond of propane;

(2) Propylene formed and hydroxyl species (C-OH) remain as intermediates;

(3) Thermal decomposition of C-OH happened and ketonic C=O was regenerated.

The population of ketonic C=O species can also be enhanced via HNO_3 activation of OMC, which will strengthen the propane conversion. However, propylene selectivity was consequently decreased a little due to the increased population of acid sites on the catalyst surface, and this will enhance a further cracking of propylene to lower hydrocarbons or even coke formation.

Compared to any other kinds of metal-based catalysts, ordered mesoporous carbon has huge advantages in any aspects of catalytic performance (propane conversion, propylene se-

lectivity, coke resistance, thermal stability). However, like many new materials, the greatest barrier for OMC to be industrialised would be how to scale-up the catalyst synthesis, and the difficulty of catalyst regeneration if deactivated by coke during the larger time on stream in a manufacturing process.

In short, DHP has the advantages including high product yield and selectivity, but due to the very high operating temperature, the energy consumption is a big issue when taking industrialisation into consideration. And its poor coking resistance in the process limits the development and popularity both in the lab and industry.

With the concern of rapidly generated coke during the DHP, oxidants were introduced into the process in order to inhibit the coke formation. Oxygen was firstly introduced as a "coke sweeper" by Skarchenko et al. in 1968 [60], and this oxygen-containing process is usually named Oxidative Dehydrogenation of Propane (ODHP, $C_3H_8 + \frac{1}{2}O_2 \rightarrow C_3H_6 + H_2O$). Besides the gasification of coke, two different mechanisms over the catalysts were also claimed to enhance the catalytic performance with the presence of oxygen.

The communal mechanism over all kinds of catalysts was called "radical reactive mechanism", which is explained as following equations:

(1) One of the C-H bond on the methylene ($-CH_2-$) of propane was firstly cracked to form adsorbed $CH_3CH \cdot CH_3$ radicals (claimed by Michalakos et al. [61]);

$$C_3H_8 + O_2 \rightarrow CH_3CH \cdot CH_3 + HO_2 \cdot \text{.....} \mathbf{R.1.15}$$

(2) One of the C-H bond on methyl ($-CH_3$) of propane was cracked to form propylene;

$$CH_3CH \cdot CH_3 + O_2 \rightarrow C_3H_6 \cdot + HO_2 \cdot \text{.....} \mathbf{R.1.16}$$

(3) The generated $HO_2 \cdot$ radicals will react with propane to form $CH_3CH \cdot CH_3$ radicals and H_2O_2;

$$C_3H_8 + HO_2 \cdot \rightarrow CH_3CH \cdot CH_3 + H_2O_2 \text{....} \mathbf{R.1.17}$$

(4) H_2O_2turns to $OH\cdot$ radicals which react with propane to form $CH_3CH\cdot CH_3$ radicals and H_2O.

$$C_3H_8 + H_2O_2 \rightarrow C_3H_8 + 2OH\cdot \rightarrow CH_3CH\cdot CH_3 + H_2O ....\mathbf{R.1.18}$$

The specific mechanism called "Mars-Van Krevelen mechanism" can occur especially on transition metal oxide catalysts. As shown in Figure 1.8, propane was firstly oxidised by the "oxidative active sites" on catalyst surface while the active sites were reduced; then the oxygen vacancies in the lattices of reduced active sites were oxidised by free-state O_2 or adsorbed oxygen radicals to regenerate the "oxidative active sites".

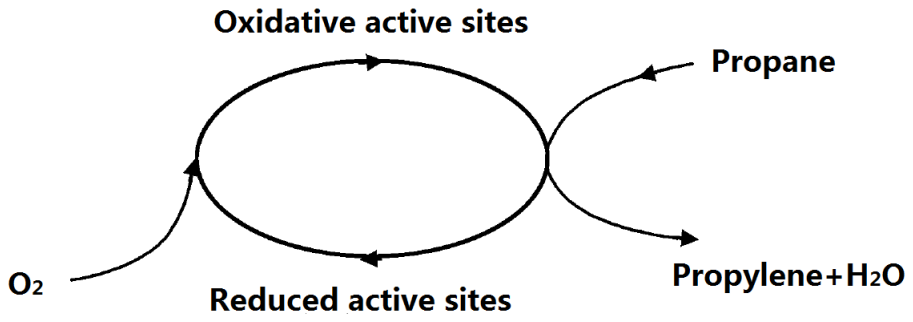

Figure 1.8: Schematic diagram of Mars-Van Krevelen mechanism.

No matter which mechanism can be suitable for the ODHP, the addition of O_2 does improve the propane conversions. Furthermore, the operating temperature has been decreased from 600℃ in DHP to 450-500℃ in ODHP, which is a huge energy-saving improvement.

The design of catalyst for ODHP was always based on V, Mo and some rare-earth elements. Due to the high coke resistance of this process, the partial pressure of propane, which can reach to 20vol.% or higher, can be much higher than DHP (usually 5vol.% or lower) when designing the catalytic reactions. However, the biggest problem for this process

would be the massive drop of propylene selectivity when O_2 is introduced into the reaction system (from 80% or above in absence of O_2 to 50% or below in presence of O_2). This problem can be partially relieved but can hardly be completely solved because the "combustion" (or directly oxidation) of hydrocarbons is always much more thermodynamically and kinetically favoured than the simple cracking of C-H bond on "oxidative active sites". Hence, a mild oxidant is desired as the alternative to O_2.

1.3.3 CO_2 as a Mild Oxidant in Dehydrogenation of Propane (DHP by CO_2, $C_3H_8 + CO_2 \rightarrow C_3H_6 + H_2O + CO$)

With "intuitive" thinking on propane dehydrogenation to propylene, O_2 is without question an over-strong oxidant to solve the problem in DHP, of the rapid coke generation and high operating temperature, by sacrificing the propylene selectivity a lot. Hence, Fox et al. started considering CO_2 as the alternative to O_2 in 1972 [62], which led to the research of DHP to the Dehydrogenation of Propane by CO_2 (DHP by CO_2, $C_3H_8 + CO_2 \rightarrow C_3H_6 + H_2O + CO$). In this process, CO_2 acts like a "balance point" between O_2 and reductive atmosphere (propane and carrier mixture). The "moderate" oxidising performance can be immediately observed by control of the operating temperature. Michorczyk et al. [63] operated the DHP by CO_2 over a Ga_2O_3 catalyst under various temperatures, and the results indicated that the extent of the coking effect soared above 600℃, which means the ideal temperature for this reaction would be 500-550℃. As mentioned above, the operating temperature of DHP is usually 600℃ or above while the one of ODHP is usually 450-500℃.

1.3.3.1 Mechanisms

When discussing the working mechanism of DHP by CO_2, there are also two theories which have been claimed so far, and the communal one which is applicable over all kinds of catalysts is to separate reaction system into two steps:

(1) Similar to the DHP, propane is first adsorbed on catalyst surface, and propylene is formed with H_2;

$$C_3H_8 \rightarrow C_3H_6 + H_2 \text{....} \mathbf{R.1.19}$$

(2) H_2 was reacted with free-state or adsorbed CO_2, which is RWGS (**R.1.2**).

Hence, from thermodynamic perspective, the equilibrium of the first step will be shifted to "more favourable" due to the consumption of H_2 in second step. Moreover, CO_2 has the potential to inhibit the coke generation by Reverse Boudouard reaction;

$$C + CO_2 \rightarrow 2CO \text{ ....} \mathbf{R.1.20}$$

Just like the "Mars-Van Krevelen Mechanism" in ODHP, the redox cycle between $Cr(VI)$ and $Cr(III)$ species had been claimed by Shishido et al. [64]. As shown in Figure 1.9, $Cr(VI)$ acts as an electron acceptor to oxidise propane and propylene is formed together with H_2O, and the reduced $Cr(III)$ species were re-oxidised by CO_2 to $Cr(VI)$ while CO was produced. Compared to the dehydrogenation of propane over $Cr(III)$ species, the ODHP over $Cr(VI)$ species is much more kinetically favoured. As a result, the amount of $Cr(VI)$ species cannot be reduced rapidly but be kept at higher valence state for a much longer period of time in the presence of CO_2, and hence, the catalytic performance can be kept at higher level for longer time.

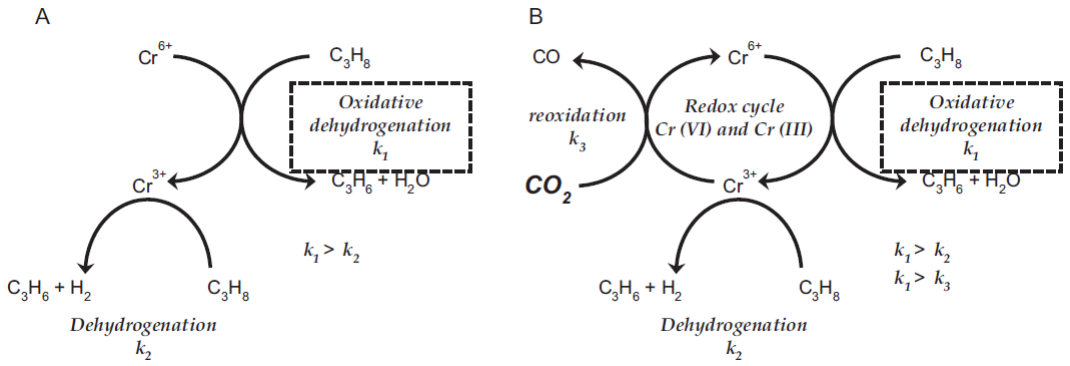

Figure 1.9: Proposed reaction mechanism of dehydrogenation of C_3H_8 (A) in the absence of CO_2 and (B): in the presence of CO_2. [64]

However, CO_2 is also playing a negative effect due to the competitive adsorption between propane and CO_2 (or generated H_2O), and the decrease of propane conversion is getting serious with the increasing CO_2 partial pressure, which has been proved by lots of researchers [52, 64–66].

1.3.3.2 The Support Effect on DHP by CO_2

The support effect is important once again in the heterogeneous catalysis process. Different kinds of supports can not only improve the dispersion of active sites but also offer an interaction with the dopant so that the electronic property of the catalyst surface is changed. For instance, Michorczyk et al. prepared a series of Cr-based oxide catalysts on a SBA-1 zeolite support [67] and found that higher-valent states of Cr ($Cr(VI)$ and $Cr(V)$) can be formed even though the $Cr(III)$ precursor was used for sample preparation, and this is attributed to the partial oxidation of $Cr(III)$ during the calcination of samples in air. The stabilised states of Cr are $Cr(VI)$, $Cr(V)$ and $Cr(III)$, and the distribution of different kinds of Cr species was varied by changing the total Cr content on catalyst surface:

Below 5wt% of Cr loading level: On the surface of SAB-1, Cr is more likely to achieve mono-layer dispersion and dispersed $Cr(V)$ is observed together with $Cr(VI)$ in the form

of chromates and dichromates;

Above 7wt% of Cr loading level: The dominant Cr species is agglomerated $Cr(III)$ in the form of crystalline Cr_2O_3 and $Cr(VI)$ in the form of dichromates while $Cr(V)$ species disappear.

The cause of competitive adsorption between CO_2 and propane, which is a negative influence on propane conversion during the reaction as mentioned in last section, can be explained by the modified acidity and basicity on catalyst surface with different supports. Takahara and his co-workers [65] prepared some Cr-based catalysts supported on different oxides (such as Al_2O_3, SiO_2 and so on.) and tested them for both DHP and DHP by CO_2. The results showed that the reactivity was decreased over Cr_2O_3/Al_2O_3 but increased over Cr_2O_3/SiO_2 in the presence of CO_2 when comparing to the reactivity in the absence of CO_2. Similar results was observed by Shishido et al. as well [64], and this is due to the different acid-base properties of Al_2O_3 and SiO_2: it is proved by NH_3-TPD and CO_2-TPD (shown in Table 1.4) that Al_2O_3 is a kind of amphoteric support (both acid and base sites available on surface) while SiO_2 is a typical acidic support (almost no base sites available on surface). Since the definition of surface basicity is usually defined by CO_2-TPD, we can easily assume that the surface basicity can immediately decide the ability of a material to adsorb CO_2 on its surface. Hence during the reactions, CO_2 was adsorbed by basic sites on the surface of Cr_2O_3/Al_2O_3, and the competitive adsorption and the adsorption of propane was inhibited. However, there was no CO_2 attached to the base sites of Cr_2O_3/SiO_2, which means no negative influence from the competitive adsorption occurred. Furthermore, the DHP step ($C_3H_8 \rightarrow C_3H_6 + H_2$) would be improved due to the H_2 consumption by CO_2 (RWGS, $H_2 + CO_2 \rightarrow H_2O + CO$), and that is why an increased reactivity of propane can be observed on Cr_2O_3/SiO_2 in the presence of CO_2.

Table 1.4: NH_3-TPD and CO_2-TPD results over supported $Ga_2O_3$and various pure supports. [66]

Sample	NH_3-TPD $(mmol/g)$	CO_2-TPD $(mmol/g)$
Ga_2O_3/Al_2O_3	0.57	0.09
Ga_2O_3/SiO_2	0.26	0.02
Al_2O_3	0.41	0.07
SiO_2	0.13	0.01

1.3.3.3 Selection of Elements in Catalyst preparation

Besides the support effect, the selection of elements in catalyst preparation was also an important issue in catalyst design, and Cr-based oxides doped on different kinds of support were the most discussed group of catalysts in DHP by CO_2 through the decades from 1972. As mentioned in the DHP section, Supported Cr-based oxide had already been agreed to be a robust catalyst group to activate propane with high conversion and propylene selectivity. However, with the additional presence of CO_2, the active sites on catalyst surface have been changed due to the redox cycle between $Cr(VI)$ and $Cr(III)$ species (as shown in Figure 1.9). Claimed by the previous study [68], the general belief was that $Cr(VI)$ species was consumed by hydrocarbons at the beginning of the process, which lead to the deeper cracking of propane (or propylene), and the $Cr(III)$ species became the active sites for the later DHP step. On the contrary, with the presence of CO_2, Takehira et al. claimed that the active sites were $Cr(VI)O_4$ tetrahedra [69], and the slow regeneration of $Cr(VI)O_4$ tetrahedra from reduced $Cr(III)O_6$ octahedra could be proved by multiple evidence from various characterisation methods including UV-vis, UV-Raman, TPR and so on. However, although the redox cycle between $Cr(VI)$ and $Cr(III)$ species looks fascinating, only a very limited population of $Cr(III)$ species can be oxidised by CO_2 in reality, and hence the enhancement of $Cr(III)$ oxidation is becoming a major direction to study.

Ga-based oxide was first reported by Nakagawa et al. in 1998 [70], and then it became the second most popular element in catalyst design for the dehydrogenation of propane.

Zheng et al. [71] tested the reaction over different types of crystalline Ga_2O_3 ($\alpha-$, $\beta-$,$\gamma-$ and δ-Ga_2O_3). From the results they found that the highest activity of γ-Ga_2O_3 was attributed to its higher surface area, and in fact the β-Ga_2O_3 may have the best performance due to the highest turnover frequency. Hence, Zheng and his co-workers claimed that the Ga species on the surface of β-Ga_2O_3 was be the key to the activity of Ga-based catalysts. Following Zheng's research, Xu and his co-workers [66] studied the DHP by CO_2 over β-Ga_2O_3 catalysts doped on various supports. The results showed that the surface acidity of the catalyst was modified a lot by different supports, and the supports with higher acidity (ZrO_2, Al_2O_3 and TiO_2) performed better than the ones with lower acidity (SiO_2 and MgO). Furthermore, on Ga_2O_3/TiO_2, propane dehydrogenation was even improved in the presence of CO_2 than without CO_2, (which was totally different from the results of Shishido et al. on Cr_2O_3/TiO_2 [64]) and this was attributed to the special interaction between β-Ga_2O_3 and a TiO_2 support which enhanced the adsorption of produced H_2 and hence the RWGS ($H_2 + CO_2 \rightarrow H_2O + CO$) was consequently improved. Besides supported Ga_2O_3, the $Ga - Al$ solid solution ($Ga_xAl_{10-x}O_{15}$) catalyst introduced by Chen et al. was also approved to be well-performed [72]. From their research, tetrahedral surface Ga^{3+} sites, which enhanced the Lewis-acidity on surface and hence propane conversions, was more favoured to be formed on a $Ga_xAl_{10-x}O_{15}$ rather than Ga_2O_3/Al_2O_3, and propylene was more easily desorbed from $Ga_xAl_{10-x}O_{15}$ surface, which limited the coke formation on catalyst surface.

As an element comes from the same group as gallium, indium-based catalysts were also studied in recent years [73, 74]. From the previous study of Chen et al. [74], dispersion of In_2O_3 on different supports immediately decides the population of In^0 species, which are the real active sites of the catalyst, formed on the surface. However, the biggest problem of In-based catalysts so far is to find a proper route to regenerate the spent catalysts without any oxidation of In^0 species, which needs further investigation.

1.3.4 The Road-ahead to CO_2 Emission Reduction for these Two Processes

It is important to foresee how to link the existing processes (or to-be-existing like DMR) with CO_2 emission reduction schemes.

Compared to DMR, the DHP by CO_2 reaction is much easier to operate under a solar thermal heating system because of the lower reaction temperatures. Propylene, the established product, is mainly converted to polypropylene in the downstream industry which of course is a permanent storage of carbon by producing building materials (polypropylene can last in earth for more than 100years, and hence the carbon captured in this form is permanently sequestrated from the atmosphere unless being burnt). The whole process including polymer production is therefore an ideal removal of carbon from cycling it between CO_2 emission and hydrocarbons if solar thermal heating technology can offer enough energy with high-enough temperature. Furthermore, the ultimate goal of this application is to draw CO_2 from the atmosphere as carbon source. It is apparent to understand the increasing difficulty in concentrating CO_2 when the CO_2 source is getting more diluted. The minimum thermodynamic energy cost of CO_2 separation (from CO_2/N_2 mixture in different ratios) is calculated [75]. In theory, about 521.7 MJ of energy consumption is needed for separating 1 tonne of CO_2 from atmosphere, while the figure drops to 163.6 MJ when the CO_2 concentration rises to 20vol.% in CO_2/N_2 mixture. Despite this, calculated capture energy costs using industrial benchmark capture agents such as monoethanolamine (MEA) and other amines frequently exceed 3000–4000 MJ per tonne CO_2 even when starting from relatively concentrated CO_2 sources (such as flue gas), which means the CO_2 capture from atmosphere has a great potential but long way to go.

The DMR process is hard to be linked with solar thermal heating energy due to the requirement of high temperature (800℃ or above) required, and this is currently the biggest

problem for this process to be applied although many high performing catalysts have been developed with long lifetimes on stream. Simakov et al. has reviewed the research on combination of solar thermal heating and the methane reforming process [76], and they claimed an approximate limit of <600℃ for parabolic concentration of solar energy although the methane reforming process is not thermodynamically favourable at this temperature. From other aspects, DMR is a promising route to be the major part of the Tri- Methane Reforming (TMR) process which is mixing reaction system containing SMR, DMR and exothermic methane oxidation (EMO, $CH_4 + \frac{1}{2}O_2 \rightarrow CO + 2H_2$). Song et al. [77] have claimed the future for TMR is to collect the oxidant source from flue gas in industry, (which contains CO_2, H_2O and O_2 30vol% in total), and also use the flue gas heat (usually ~1200℃ as energy output from furnace but cooled down to 150℃ around the stack after gradual heat exchange) immediately. Also from the research of Halmann and Steinfeld [78], the flue gas, both from the coal-fired and the gas-fired power stations, were modelled to be reacted with natural gas in the Tri- Methane Reforming (TMR) process, and the calculated results (CO_2 emission avoidance, fuel saving and economic viability) were all attractive.

There are disadvantages of using the N_2-diluted CO_2 source: one is the heat-up cost for the substantial N_2 in flue gas mixture[79]; the other is the increased plant size -to maintain a high level of productivity - which leads to more expensive CAPEX and OPEX costs [80]. Despite these, the advantages are also distinct. In DHP process, the dilution is often needed to increase the conversion of feedstock or give long coking tolerance. Moreover, Halmann and Steinfeld also claimed that syn-gas containing nitrogen, the product from TMR process, is perceived to be particularly useful for ammonia synthesis in the downstream [78]. Last but not least, the immediate use of flue gas will save at least the energy and the apparatus required to concentrate CO_2 from flue gas.

1.4 From "Reduced" to "Negative" CO_2 Emission via CCU

Apart from possible long-term storage in forms of polymers, it is widely accepted to be pointless if the energy source for CCU is from fossil-fuel-derived combustion. Quite simply, renewable energy must always be used to drive CO_2-fuel production. According to the calculation in Table 1.1, it has been argued that in spite of fully using renewable energy for the running, CCU will never lead to a reduction of CO_2 emission if only short-term chemicals or fuels (such as oil or alcohol) are produced through this process, and this is true if we are holding the precondition to ultimately burn the produced oil over a long period of time.

However, from a short-term perspective, we can assume that the total essential energy request has a "cap" during any limited length of time. Figure 1.10 shows the potential of flue-gas, where CO_2 can be utilised as a carbon source to produce methanol, polyethylene, diesel and petrol. From IEA's statistics [81, 82], the CO_2 potential from power plants is estimated (CO_2 is supposed to be 100% converted to methanol:$CO_2+3H_2 \rightarrow CH_3OH+H_2O$). In Berkel's report[83], the global markets of chemicals (traditional markets) and fuels (new growth markets) are also claimed. The comparison between potential and markets indicates that a 40% conversion of CO_2 in power plants will absolutely cover the global energy and chemical demands.

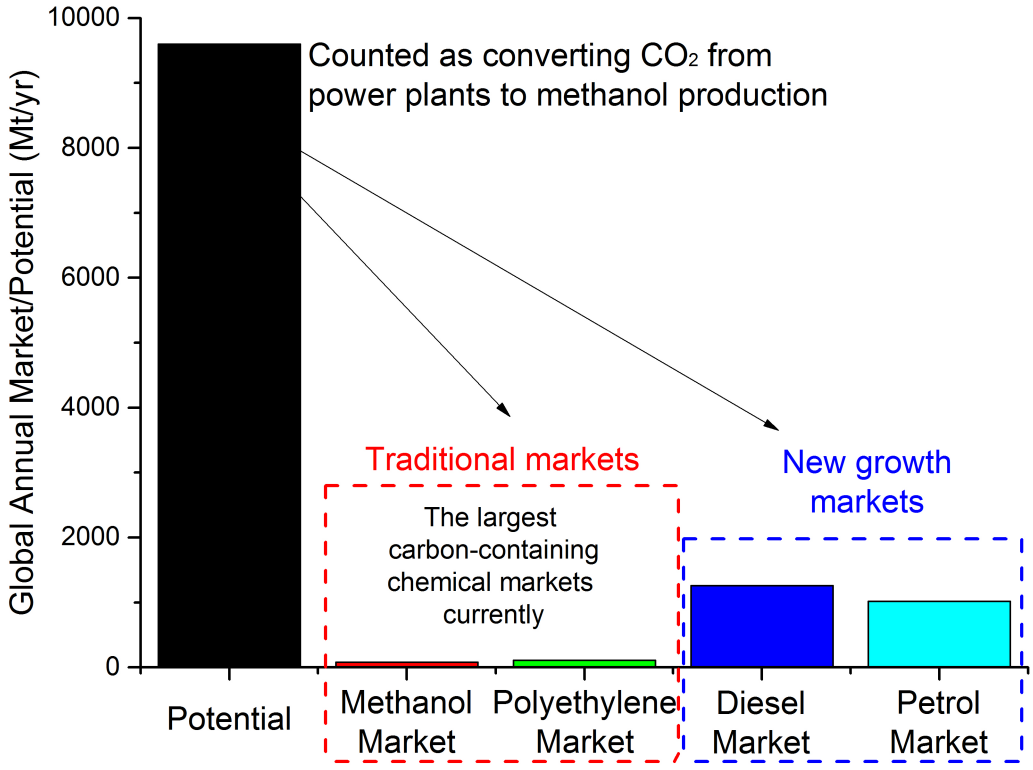

Figure 1.10: Current global annual markets vs. CCU potential (The "Market" data are adapted from Berkel's work [83], whilst the "Potential" data from power plants are calculated based on the statistical research of IEA[81, 82]. The CO_2 potential from power plants is estimated with the setting that 1mol CO_2 will be 100% converted to produce 1mol methanol.)

Since we have insisted that CCU is meaningful only when it is driven by renewable energy, this route is in essence to reduce the demand on fossil fuels by replacing part of it with renewable energy. In other words, by encouraging CCU applications with renewable energy source, is a real slow-down of CO_2 emission because the real exploitation of fossil-fuel is decreased. The following Figure 1.11 can also illustrate this change when total energy request is fixed.

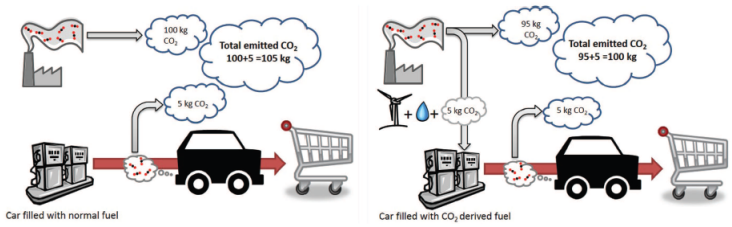

Figure 1.11: The change of CO_2 emission by CCU under a fixed energy demand. (adapted from the article of Armstrong and Styring.[11])

But if considering further, we need to make efforts, such as negative CO_2 emission, to achieve climate change mitigation. Or in other words: to ultimately reduce the CO_2 concentration in the atmosphere.

It is apparent to understand that we can only capture the point emission of CO_2 around stacks in factories but can hardly accumulate the small/individual CO_2-emitters (e.g. vehicles) which are also burning fossil-fuels, and this will lead to a slow but positive CO_2 emission in to the air even the whole emission of CO_2 from industry has been captured. Figure 1.12 shows that nearly 40% of world CO_2 emission (from fuel combustion) in 2014 was from the small/individual emitters, which means we would still have around 12600 Mt of CO_2 emission from fossil fuels even if we had already captured 100% of CO_2 from power plants and factories all over the world. Hence, it is impossible to reduce the CO_2 concentration only by CCU/CCS at the end of flues, and the real negative CO_2 emission route can only become true when CO_2 can be drawn and concentrated from the air, and of course, driven by renewable/carbon-free energy.

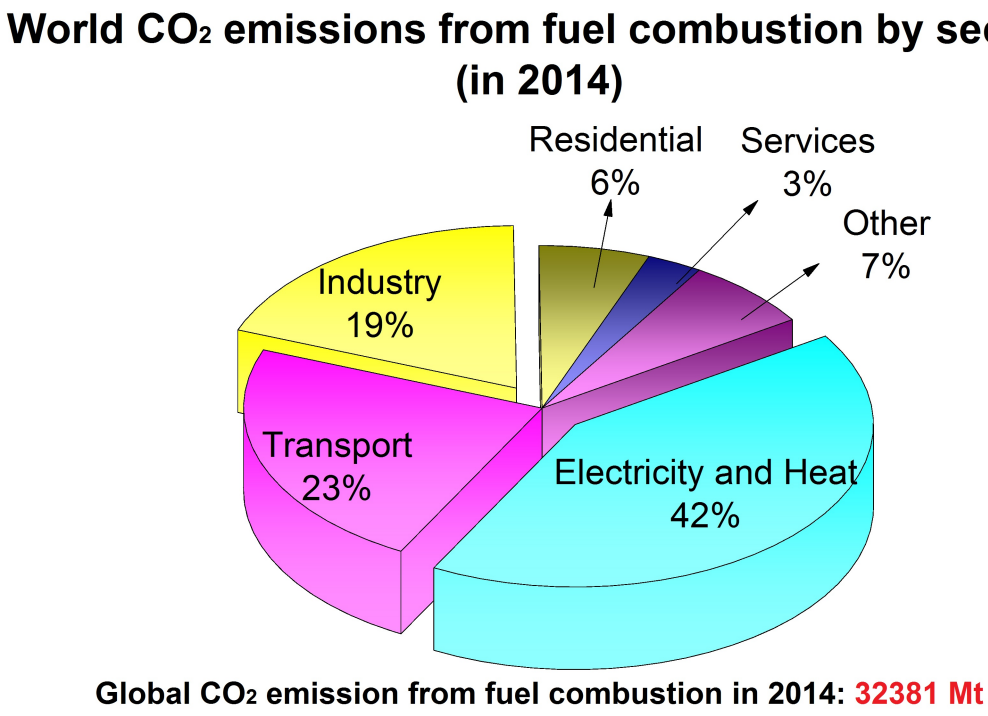

Figure 1.12: World CO_2 emissions from fuel combustion by sector in 2014. (data from IEA [82])

The ultimate technology to support and CO_2-neutral or CO_2-negative emission will be the capture of CO_2 from the atmosphere.

As shown at the very beginning of this chapter, the CO_2 concentration in Earth's atmosphere has exceeded 400ppm on average, which increased 2.5% in the last 5 years. However, this CO_2 level in the atmosphere is only about 1/300 less concentrated than in flue gas, and the CO_2 concentration from highly diluted level mean technology development is required. The basic mechanism for CO_2 concentration from air is to absorb CO_2 with solution or solid at lower temperature while release it at higher temperature. Pioneers have started to conquer this mountain [84] but the problem at the centre is not only how to reduce the costs and to attract investigators for scaling-up to a real application level, but

also the slow rate of CO_2 accumulation if we are approaching to the pure CO_2 product.

As discussed in the last section, it seems to be unnecessary to achieve very high concentration of CO_2 if the captured product is going to the CCU processes, especially in the DHP by CO_2 process which requires only 5-10vol.% of CO2 in the feedstock. Due to the requirement of the N_2-diluted CO_2 source, the CO_2 enrichment can run less than halfway of being 100%, which can surely lead to the less operational costs, faster production, and last but not least, a low threshold for the technology to be realised.

Bibliography

[1] Z. Jiang, T. Xiao, V. L. Kuznetsov, and P. P. Edwards. Turning Carbon Dioxide into Fuel. *Philosophical Transactions of the Royal Society of London A*, 368(1923):3343–3364, 2010.

[2] C. M. Kalamaras and A. M. Efstathiou. Hydrogen Production Technologies: Current State and Future Developments. *Conference Papers in Energy*, pages 1–9, 2013.

[3] E. Dlugokencky and P. Tans. NOAA/ESRL, Available at http://www.esrl.noaa.gov/gmd/ccgg/trends/ (last accessed on Feb.16th 2017).

[4] R. M. Key, A. Kozyr, C. L. Sabine, K. Lee, R. Wanninkhof, J. L. Bullister, R. A. Feely, F. J. Millero, C. Mordy, and T.-H. Peng. A Global Ocean Carbon Climatology: Results from Global Data Analysis Project (GLODAP). *Global Biogeochemical Cycles*, 18(4):1–23, 2004.

[5] J. M. Hall-Spencer, R. Rodolfo-Metalpa, S. Martin, E. Ransome, M. Fine, S. M. Turner, S. J. Rowley, D. Tedesco, and M.-C. Buia. Volcanic Carbon Dioxide Vents Show Ecosystem Effects of Ocean Acidification. *Nature*, 454(7200):96–99, 2008.

[6] IEA. IEA Energy Technology Perspectives 2014, Harnessing Electricity's Potential. Technical report, Paris: IEA Publicaions, 2014.

[7] SaskPower. Boundary Dam Carbon Capture Project. Available at http://www.saskpower.com/about-us/category/blog/ccs-blog/ (last accessed on

Feb.16th 2017).

[8] J. Glennie. Analysis of the Cash and Carbon flows of Boundary Dam Coal-Fired Power Station. Technical report, 2015.

[9] Global CCS Institute. The Global Status of CCS. pages 1–12, 2013.

[10] Centre for Low Carbon Futures. Carbon Capture and Utilisation in the Green Economy. pages 1–60, 2011.

[11] K. Armstrong and P. Styring. Assessing the Potential of Utilization and Storage Strategies for Post-Combustion CO2 Emissions Reduction. *Frontiers in Energy Research*, 3:1–9, 2015.

[12] M. Specht, A. Bandi, C. U. Maier, and J. Schwarz. Energetics of Solar Methanol Synthesis from Atmospheric Carbon Dioxide Compared to Solar Liquid Hydrogen Generation. *Energy Conversion and Management*, 33(5-8):537–543, 1992.

[13] W. Shockley and H. J. Queisser. Detailed Balance Limit of Efficiency of p-n Junction Solar Cells. *Journal of Applied Physics*, 32(3):510, 1961.

[14] A. Freundlich, A. Mehrotra, M. Gunasekera, G. Lancel, and G. K. Vijaya. Ultra-Thin Defect Tolerant High Efficiency III-V Tandems for Development of Low-Cost Photovoltaics. *IEEE 40th Photovoltaic Specialist Conference (PVSC)*, pages 2117–2121, 2014.

[15] V. Siva Reddy, S. C. Kaushik, K. R. Ranjan, and S. K. Tyagi. State-of-the-Art of Solar Thermal Power Plants: A Review. *Renewable and Sustainable Energy Reviews*, 27:258–273, 2013.

[16] B. Skoloff and M. R. Blood. Huge Thermal Plant Opens as Solar Industry Grows. Available at: http://bigstory.ap.org/article/huge-thermal-plant-opens-solar-industry-grows (last accessed on Feb.21st 2017).

[17] C. Perkins and A. W. Weimer. Solar-Thermal Production of Renewable Hydrogen. *AIChE Journal*, 55:286–293, 2009.

[18] T. Nomura, N. Okinaka, and T. Akiyama. Technology of Latent Heat Storage for High Temperature Application: A Review. *Isij International*, 50(9):1229–1239, 2010.

[19] I. Chorkendorff and J. W. Niemantsverdriet. *What is Catalysis*. John Wiley & Sons, Inc., 2003.

[20] G. W. Castellan. *Physical Chemistry (3rd Edition)*. Addison Wesley Publishing Company, Inc., 1983.

[21] M. J. Pilling and P. W. Seakins. *Reaction Kinetics*. Oxford University Press, 2nd edition, 1995.

[22] M. Aresta and A. Dibenedetto. Utilisation of CO2 as a Chemical Feedstock: Opportunities and Challenges. *Dalton Transactions*, 28(28):2975–2992, 2007.

[23] A. T. Ashcroft, A. K. Cheetham, and M. L. H Green. Partial Oxidation of Methane to Synthesis Gas Using Carbon Dioxide. *Nature*, 352:225–226, 1991.

[24] M. E. Davis. *Fundamentals of Chemical Reaction Engineering (Chapter 5)*. McGraw-Hill Higher Education, 2003.

[25] O. Takayasu, N. Hongo, and I. Matsuura. *New Aspects of Spillover Effect in Catalysis-For Development of Highly Active Catalysts, Proceedings of the Third International Conference on Spillover(Studies in Surface Science and Catalysis, Volume 77)*. Elsevier, 1993.

[26] A. Erdohelyi. Activation of CH4 and Its Reaction with CO2 over Supported Rh Catalysts. *Journal of Catalysis*, 141(1):287–299, 1993.

[27] Z. L. Zhang, V. A. Tsipouriari, A. M. Efstathiou, and X. E. Verykios. Reforming of Methane with Carbon Dioxide to Synthesis Gas over Supported Rhodium Catalysts: I. Effects of Support and Metal Crystallite Size on Reaction Activity and Deactivation Characteristics. *Journal of Catalysis*, 158(1):51–63, 1996.

[28] Z.-F. Yan, R.-G. Ding, L.-H. Song, and L. Qian. Mechanistic Study of Carbon Dioxide Reforming with Methane over Supported Nickel Catalysts. *Energy & Fuels*,

12(10):1114–1120, 1998.

[29] V. A. Tsipouriari, Z. Zhang, and X. E. Verykios. Catalytic Partial Oxidation of Methane to Synthesis Gas over Ni-Based Catalysts. *Journal of Catalysis*, 179(1):283–291, 1998.

[30] N. Mota, C. Alvarez-Galvan, R. M. Navarro, and J. L. G. Fierro. Biogas as a Source of Renewable Syngas Production: Advances and Challenges. *Biofuels*, 2(3):325–343, 2011.

[31] M. L. Pritchard, R. L. McCauley, B. N. Gallaher, and W. J. Thomson. The Effects of Sulfur and Oxygen on the Catalytic Activity of Molybdenum Carbide during Dry Methane Reforming. *Applied Catalysis A: General*, 275(1-2):213–220, 2004.

[32] F. Barrai, T. Jackson, N. Whitmore, and M. J. Castaldi. The Role of Carbon Deposition on Precious Metal Catalyst Activity During Dry Reforming of Biogas. *Catalysis Today*, 129(3-4):391–396, 2007.

[33] N. A. Pechimuthu, K. K. Pant, and S. C. Dhingra. Deactivation Studies over Ni-K/CeO2-Al2O3 Catalyst for Dry Reforming of Methane. *Industrial & Engineering Chemistry Research*, 46(6):1731–1736, 2007.

[34] J. H. Edwards and A. M. Maitra. The Chemistry of Methane Reforming with Carbon Dioxide and Its Current and Potential Applications. *Fuel Processing Technology*, 42(2-3):269–289, 1995.

[35] G. Valderrama, M. R. Goldwasser, C. U. de Navarro, J. M. Tatibouët, J. Barrault, C. Batiot-Dupeyrat, and F. Martínez. Dry Reforming of Methane over Ni Perovskite Type Oxides. *Catalysis Today*, 107-108:785–791, 2005.

[36] N. Wang, W. Chu, T. Zhang, and X.-S. Zhao. Manganese Promoting Effects on the Co-Ce-Zr-Ox Nano Catalysts for Methane Dry Reforming with Carbon Dioxide to Hydrogen and Carbon Monoxide. *Chemical Engineering Journal*, 170(2-3):457–463, 2011.

[37] R. R. Grigoryan, L. A. Vartikyan, R. A. Mnatsakanyan, and A. R. Zurnachyan. Dry Reforming of Methane on Molybdenum Carbide. *Hayastani Kimiakan Handes*, 63(4):535–537, 2010.

[38] K. Asai, K. Takane, Y. Nagayasu, S. Iwamoto, E. Yagasaki, and M. Inoue. Decomposition of Methane in the Presence of Carbon Dioxide over Ni Catalysts. *Chemical Engineering Science*, 63(20):5083–5088, 2008.

[39] L. Guczi, G. Stefler, O. Geszti, I. Sajó, Z. Pászti, A. Tompos, and Z. Schay. Methane Dry Reforming with CO2: A Study on Surface Carbon Species. *Applied Catalysis A: General*, 375(2):236–246, 2010.

[40] B. Steinhauer, M. R. Kasireddy, J. Radnik, and A. Martin. Development of Ni-Pd Bimetallic Catalysts for the Utilization of Carbon Dioxide and Methane by Dry Reforming. *Applied Catalysis A: General*, 366(2):333–341, 2009.

[41] A. J. Brungs, A. P. E. York, and M. L. H. Green. Comparison of the Group V and VI Transition Metal Carbides for Methane Dry Reforming and Thermodynamic Prediction of Their Relative Stabilities. *Catalysis Letters*, 57:65–69, 1999.

[42] H. Shao, E. L. Kugler, W. Ma, and D. B. Dadyburjor. Effect of Temperature on Structure and Performance of In-House Cobalt-Tungsten Carbide Catalyst for Dry Reforming of Methane. *Industrial & Engineering Chemistry Research*, 44(14):4914–4921, 2005.

[43] A. P. E. York, J. B. Claridge, A. J. Brungs, S. Tsang, and M. L. H. Green. Molybdenum and Tungsten Carbides as Catalysts for the Conversion of Methane to Synthesis Gas Using Stoichiometric Feedstocks. *Chemical Communications*, (1):39–40, 1997.

[44] J. B. Claridge, A. P. E. York, A. J. Brungs, C. Marquez-Alvarez, J. Sloan, S. C. Tsang, and M. L. H. Green. New Catalysts for the Conversion of Methane to Synthesis Gas: Molybdenum and Tungsten Carbide. *Journal of Catalysis*, 180(1):85–100, 1998.

[45] F. H. Ribeiro, R. A. Dalla Betta, G. J. Guskey, and M. Boudart. Preparation and

Surface Composition of Tungsten Carbide Powders with High Specific Surface Area. *Chemistry of Materials*, 3(5):805–812, 1991.

[46] A. Erdöhelyi, J. Cserényi, E. Papp, and F. Solymosi. Catalytic Reaction of Methane with Carbon Dioxide over Supported Palladium. *Applied Catalysis A: General*, 108(2):205–219, 1994.

[47] L. Basini and D. Sanfilippo. Molecular Aspects in Syn-Gas Production: The CO2-Reforming Reaction Case. *Journal of Catalysis*, 157(1):162–178, 1995.

[48] A. J. Brungs, A. P. E. York, J. B. Claridge, C. Marquez-Alvarez, and M. L. H. Green. Dry Reforming of Methane to Synthesis Gas over Supported Molybdenum Carbide Catalysts. *Catalysis Letters*, 70:117–122, 2000.

[49] A. R. S. Darujati and W. J. Thomson. Stability of Supported and Promoted-Molybdenum Carbide Catalysts in Dry-Methane Reforming. *Applied Catalysis A: General*, 296(2):139–147, 2005.

[50] J. Raskó and J. Kiss. Infrared Study of the Adsorption of CO and CH3 on Silica-Supported MoO3 and Mo2C Catalysts. *Applied Catalysis A: General*, 253(2):427–436, 2003.

[51] S. Naito, M. Tsuji, and T. Miyao. Mechanistic Difference of the CO2 Reforming of CH4 over Unsupported and Zirconia Supported Molybdenum Carbide Catalysts. *Catalysis Today*, 77(3):161–165, 2002.

[52] R. Wu, P. Xie, Y. Cheng, Y. Yue, S. Gu, W. Yang, C. Miao, W. Hua, and Z. Gao. Hydrothermally Prepared Cr2O3-ZrO2 as a Novel Efficient Catalyst for Dehydrogenation of Propane with CO2. *Catalysis Communications*, 39:20–23, 2013.

[53] L. Zhang, Y. Liu, Y. Liu, Z. Hu, Z. Hu, Y. Yang, Y. Yang, H. Yu, H. Yu, Z. Yuan, and Z. Yuan. Advance in Catalysts for Propane Dehydrogenation to Propylene. *Acta Petrolei Sinica*, 31(2):400–417, 2015.

[54] K. K. Kearby. Catalytic Dehydrogenation. *Catalysis*, 3:453–491, 1955.

[55] M. Santhosh Kumar, D. Chen, A. Holmen, and J. C. Walmsley. Dehydrogenation of Propane over Pt-SBA-15 and Pt-Sn-SBA-15: Effect of Sn on the Dispersion of Pt and Catalytic Behavior. *Catalysis Today*, 142(1-2):17–23, 2009.

[56] Z. Han, S. Li, F. Jiang, T. Wang, X. Ma, and J. Gong. Propane Dehydrogenation over Pt-Cu Bimetallic Catalysts: the Nature of Coke Deposition and the Role of Copper. *Nanoscale*, 6(17):10000–10008, 2014.

[57] L. Liu, Q.-F. Deng, B. Agula, X. Zhao, T.-Z. Ren, and Z.-Y. Yuan. Ordered Mesoporous Carbon Catalyst for Dehydrogenation of Propane to Propylene. *Chemical Communications*, 47:8334–8336, 2011.

[58] L. Liu, Q.-F. Deng, Y.-P. Liu, T.-Z. Ren, and Z.-Y. Yuan. HNO3-Activated Mesoporous Carbon Catalyst for Direct Dehydrogenation of Propane to Propylene. *Catalysis Communications*, 16(1):81–85, 2011.

[59] L. Liu, Q.-F. Deng, B. Agula, T.-Z. Ren, Y.-P. Liu, B. Zhaorigetu, and Z.-Y. Yuan. Synthesis of Ordered Mesoporous Carbon Materials and Their Catalytic Performance in Dehydrogenation of Propane to Propylene. *Catalysis Today*, 186(1):35–41, 2012.

[60] V. K. Skarchenko. Oxidative Dehydrogenation of Hydrocarbons. *Uspekhi Khimii*, 37(1):3–35, 1968.

[61] P. M. Michalakos, M. C. Kung, I. Jahan, and H. H. Kung. Selectivity Patterns in Alkane Oxidation over Mg3(VO4)2-MgO, Mg2V2O7, and (VO)2P2O7. *Journal of Catalysis*, 140(1):226–242, 1993.

[62] D. B. Fox, E. H. Lee, and M.-H Rei. Carbon Dioxide as Hydrogen Acceptor in Dehydrogenation of Alkanes. *Industrial and Engineering Chemistry, Product Research and Development*, 11:444–446, 1972.

[63] P. Michorczyk and J. Ogonowski. Dehydrogenation of Propane in the Presence of Carbon Dioxide over Oxide-Sased Catalysts. *Reaction Kinetics and Catalysis Letters*, 78(1):41–47, 2003.

[64] T. Shishido, K. Shimamura, K. Teramura, and T. Tanaka. Role of CO2 in Dehydrogenation of Propane over Cr-based Catalysts. *Catalysis Today*, 185(1):151–156, 2012.

[65] I. Takahara, W. C. Chang, N. Mimura, and M. Saito. *Advances in Chemical Conversions for Mitigating Carbon Dioxide, Proceedings of the Fourth International Conference on Carbon Dioxide Utilization(Studies in Surface Science and Catalysis, Volume 114)*. Elsevier, 1998.

[66] B. Xu, B. Zheng, W. Hua, Y. Yue, and Z. Gao. Support effect in Dehydrogenation of Propane in the Presence of CO2 over Supported Gallium Oxide Catalysts. *Journal of Catalysis*, 239:470–477, 2006.

[67] P. Michorczyk, P. Pietrzyk, and J. Ogonowski. Preparation and Characterization of SBA-1-Supported Chromium Oxide Catalysts for CO2 Assisted Dehydrogenation of Propane. *Microporous and Mesoporous Materials*, 161:56–66, 2012.

[68] S. Sokolov, M. Stoyanova, U. Rodemerck, D. Linke, and E. V. Kondratenko. Comparative Study of Propane Dehydrogenation over V-, Cr-, and Pt-based Catalysts: Time on-Stream Behavior and Origins of Deactivation. *Journal of Catalysis*, 293:67–75, 2012.

[69] K. Takehira, Y. Ohishi, T. Shishido, T. Kawabata, K. Takaki, Q. Zhang, and Y. Wang. Behavior of Active Sites on Cr-MCM-41 Catalysts during the Dehydrogenation of Propane with CO2. *Journal of Catalysis*, 224(2):404–416, 2004.

[70] K. Nakagawa, M. Okamura, N. Ikenaga, T. Suzuki, and T. Kobayashi. Dehydrogenation of Ethane over Gallium Oxide in the Presence of Carbon Dioxide. *Chemical Communications*, 3(9):1025–1026, 1998.

[71] B. Zheng, W. Hua, Y. Yue, and Z. Gao. Dehydrogenation of Propane to Propene over Different Polymorphs of Gallium Oxide. *Journal of Catalysis*, 232(1):143–151, 2005.

[72] M. Chen, J. Xu, F.-Z. Su, Y.-M. Liu, Y. Cao, H.-Y. He, and K.-N. Fan. Dehydrogena-

tion of Propane over Spinel-Type Gallia-Alumina Solid Solution Catalysts. *Journal of Catalysis*, 256(2):293–300, 2008.

[73] M. Chen, J. Xu, Y. Cao, H.-Y. He, K.-N. Fan, and J.-H. Zhuang. Dehydrogenation of Propane over In2O3-Al2O3 Mixed Oxide in the Presence of Carbon Dioxide. *Journal of Catalysis*, 272(1):101–108, 2010.

[74] M. Chen, J.-L. Wu, Y.-M. Liu, Y. Cao, L. Guo, H.-Y. He, and K.-N. Fan. Study in Support Effect of In2O3/MOx (M=Al,Si,Zr) Catalysts for Dehydrogenation of Propane in the Presence of CO2. *Applied Catalysis A: General*, 407(1-2):20–28, 2011.

[75] G. R. M. Dowson, I. Dimitriou, R. E. Owen, D. G. Reed, R. W. K. Allen, and P. Styring. Kinetic and Economic Analysis of Reactive Capture of Dilute Carbon Dioxide with Grignard Reagents. *Faraday Discussions*, 183:47–65, 2015.

[76] D. S. A. Simakov, M. M. Wright, S. Ahmed, E. M. A. Mokheimer, and Y. Roman-Leshkov. Solar Thermal Catalytic Reforming of Natural Gas: A Review on Chemistry, Catalysis and System Design. *Catalysis Science and Technology*, 5(4):1991–2016, 2015.

[77] C. Song. Global Challenges and Strategies for Control, Conversion and Utilization of CO2 for Sustainable Development Involving Energy, Catalysis, Adsorption and Chemical Processing. *Catalysis Today*, 115(1-4):2–32, 2006.

[78] M. Halmann and A. Steinfeld. Thermoneutral Tri-reforming of Flue Gases from Coal- and Gas-fired Power Stations. *Catalysis Today*, 115(1):170–178, 2006.

[79] C. Song and W. Pan. Tri-reforming of Methane: A Novel Concept for Catalytic Production of Industrially Useful Synthesis Gas with Desired H2/CO Ratios. *Catalysis Today*, 98(4):463–484, 2004.

[80] P. Styring, E. A. Quadrelli, and K. Armstrong. *Carbon Dioxide Utilisation: Closing the Carbon Cycle*. Elsevier Science, 2014.

[81] International Energy Agency (IEA). CO2 Emissions from Fuel Combustion - Highlights. *IEA Statistics*, 2015.

[82] International Energy Agency (IEA). Excerpt from:CO2 Emissions from Fuel Combustion. *IEA Statistics*, 2016.

[83] F. V. Berkel. Carbon Dioxide Utilisation: Thermodynamic Limitations and How to Overcome Them. *International Conference on Carbon Dioxide Utilisation*, Sep.12th, 2016.

[84] E. Kintisch. Can Sucking CO2 Out of the Atmosphere Really Work? Available at http://www.technologyreview.com/featuredstory/531346/can-sucking-co2-out-of-the-atmosphere-really-work/, 2014.

Chapter 2

Plan of the Thesis

In Chapter 1, a CO_2-utilising process without CO_2-purification and/or electricity generation from renewable energy has been outlined. Based on these preconditions, two issues are claimed to be the major thresholds before the real applications of CO_2 Capture and Utilisation (CCU): **a**, the easy access to concentrated CO_2 source; **b**, stable temperature output from renewable energy resource.

In the following chapters, both of the two CO_2-utilising processes introduced in Chapter 1, dry methane reforming (DMR) and dehydrogenation of propane by CO_2 (DHP by CO_2), are studied both via computational thermodynamic analysis and catalyst-testing experiments.

2.1 Methods in Chapter 3

To describe the methods on doing thermodynamic analysis, the formulas of calculations are derived in details at the beginning of Chapter 3.1. Based on the same principles, Aspen Plus software is introduced to help computing complex reaction systems, and the instruction on how to use this software is outlined in Chapter 3.1 as well.

The experimental methods covering the whole research process are described together with the fundamental mechanisms. They include the methods of catalyst preparations (Chapter 3.2), catalytic performance testing (Chapter 3.3) and the characterisation methods on catalysts (Chapter 3.4).

2.2 Thermodynamic Analysis in Chapter 4

By calculating the equilibrium of reaction formulas under certain conditions, it is straightforward to see the limit of reactant conversions and product yields. In other words, thermodynamics decide the potential of a process/reaction system under fixed conditions. Besides, it is also the thermodynamics that indicate whether a reaction is favoured or not.

Hence, in Chapter 4, thermodynamic studies were carried out, manually and with help from software, to make the judgment on temperature limit for DMR and DHP by CO_2 towards target products. By changing the compositions of reactants during the calculations, some low-concentration CO_2 sources (such as flue-gas in power plant and oil refinery) are predicted to be utilised immediately.

2.3 Catalyst-testing Experiment Results in Chapter 5 and 6

The experimental results and discussions of DMR and DHP by CO_2 catalysis are exhibited in Chapter 5 and 6, respectively.

The catalyst-testing experiments not only indicate the catalyst performances in a process but also discover mechanisms by characterising catalysts pre- and post- reactions. As a feedback, the derived mechanism can also instruct catalyst development in pursuing better performances.

2.4 The Link between Thermodynamics and Catalysis

It is generally accepted that the kinetics, rather than thermodynamics, help optimising the reaction conditions for a process . Hence, the link between thermodynamic studies and practical experiments is often critically judged because thermodynamic equilibrium can only indicate the theoretical limit but never reflect the real states in a reaction. In most heterogeneous catalytic reactions, the residence time of molecules on catalyst surface is typically too short for a reaction system to reach equilibrium state.

However, it is still arguable that thermodynamic study is instructive. Comparing to the mechanisms concluded via kinetic studies, the principles derived from thermodynamics are more generally adapted to all catalysts regardless the special mechanisms. On the other hand, the calculations for equilibrium state display the theoretical limit of reactant conversions and product yields, which is also an important instruction in catalyst performance enhancement and condition optimisation.

2.5 Summary and Outlook in Chapter 7

In Chapter 7, all of the research related to CCU is concluded by different processes (DMR and DHP by CO_2), and the future development and applications of these two CO_2-utilising projects are foreseen as outlooks. Potential future improvements and challenges concluded from results and discussions have been outlined as the "to-be-improved" studies in Chapter 7.3, which is not only reflection but also the direction of improvements in the future.

Chapter 3

Methods

3.1 Thermodynamic Calculations

3.1.1 Gibbs Free Energy ($\Delta_r G_m^\theta$)

Thermodynamic calculations have been widely used for more than a century to study the nature and extent of chemical process, which illustrates the energy demand and possibility of a modelled reaction at certain conditions.[1]

The standard change of reaction in Gibbs Free Energy ($\Delta_r G_m^\theta$) is important for a judgment as to whether a modelled reaction is to be favoured at certain temperature. And the relationships are shown as following,

$\Delta_r G_m^\theta(T) < 0$ ----The reaction is thermodynamically favourable at T;

$\Delta_r G_m^\theta(T) = 0$ ----The reaction is thermodynamically at equilibrium at T;

$\Delta_r G_m^\theta(T) > 0$ ----The reverse reaction is thermodynamically favourable at T.

Also $\Delta_r G_m^\theta$ can be calculated from the equilibrium constant (K^θ) with the equation $\Delta_r G_m^\theta = -RTlnK^\theta$.

To calculate the $\Delta_r G_m^\theta$, it is applicable to any reactions that:

$$\Delta_r G_m^\theta = \Delta_r H_m^\theta - T\Delta_r S_m^\theta \text{....}\mathbf{Eq.3.1}$$

In this formula, $\Delta_r H_m^\theta$ and $\Delta_r S_m^\theta$ are standard molar enthalpy of reaction and standard molar entropy of reaction respectively. Within any reaction, $\Delta_r H_m^\theta$ can be calculated by the standard molar enthalpy of formation ($\Delta_f H_m^\theta$) of reactants and products with a relationship as following,

$$\Delta_r H_m^\theta = \sum_B \nu_B \Delta_f H_m^\theta(B) \text{ ....}\mathbf{Eq.3.2.}$$

And $\Delta_f H_m^\theta$ is regarded as a function of temperature,

$$\Delta_f H_m^\theta(T) = \Delta_f H_m^\theta(298.15) + \int_{298.15}^{T} C_{(p,m)} dT \text{ ....}\mathbf{Eq.3.3}$$

$C_{(p,m)}$ is the molar heat capacity at constant pressure. When combined with equation $C_{(p,m)} = A + BT + CT^2 + DT^3 + ET^4$, **Eq.3.3** can be integrated as,

$$\Delta_f H_m^\theta(T) = \Delta_f H_m^\theta(298.15) + A \cdot (T - 298.15) + \tfrac{1}{2} B \cdot (T^2 - 298.15^2) + \tfrac{1}{3} C \cdot (T^3 - 298.15^3) + \tfrac{1}{4} D \cdot (T^4 - 298.15^4) + \tfrac{1}{5} E \cdot (T^5 - 298.15^5) \text{ ....}\mathbf{Eq.3.4}$$

Similar to $\Delta_r H_m^\theta$, $\Delta_r S_m^\theta$ can be calculated by the standard molar entropy (S_m^θ) of reactants and products with a relationship as following,

$$\Delta_r S_m^\theta = \sum_B \nu_B S_m^\theta(B) \text{ ....}\mathbf{Eq.3.5}$$

And S_m^θ can also be regarded as a function of temperature,

$$S_m^\theta(T) = S_m^\theta(298.15) + \int_{298.15}^{T} \frac{C_{(p,m)}}{T} dT \text{ ....}\mathbf{Eq.3.6}$$

Hence, after the similar combination and integration as $\Delta_f H_m^\theta(T)$ formula,

$$S_m^\theta(T) = S_m^\theta(298.15) + A \cdot (lnT - ln298.15) + B \cdot (T - 298.15) + \tfrac{1}{2} C \cdot (T^2 - 298.15^2) + \tfrac{1}{3} D \cdot (T^3 - 298.15^3) + \tfrac{1}{4} E \cdot (T^4 - 298.15^4) \text{ ....}\mathbf{Eq.3.7}$$

3.1.2 Introduction of the Aspen Plus Software

For the multiple-reaction combinations (where competitive or consecutive reactions occur), the involved single reactions are interactional to each other. For instance, one compound could be reactants of several reactions and products of several reactions at the same time. Hence, to compute the equilibrium state for a complex system - manually - is not practical due to large calculation amount. Process simulation software can help under this situation, and we used Aspen Plus (V7.3.2) to compute what with input parameters the temperature and the partial pressure of reactants.

In Aspen Plus (V7.3.2), there are two reactor models for calculating equilibrium: REquil and RGibbs. From the practical experience in using this software, an important difference between these two models is that RGibbs can deal with a system containing solid substances, whilst there is an error occurred when inputting solid substances into REquil models. In the thesis, carbon formation is considered as an unavoidable part when modelling the processes of dry methane reforming (DMR) and propane dehydrogenation by CO_2 (DHP by CO_2). Hence, the RGibbs model was kept for determining the thermodynamic equilibrium compositions for the reactions.

RGibbs solves its model by minimizing Gibbs free energy. In the cases where information on the stoichiometry is unknown and, especially, if phases changes accompany the reaction, an approach based on minimizing the Gibbs free energy of the whole mixture can be used. In this approach, the total Gibbs energy of all components (i = reactants, products, and internal standard) is minimized. For example, the Gibbs energy for an ideal gas mixture (G_{mix}) is given by:

$G_{mix} = \sum_i x_i G_i + RT \sum_i x_i ln x_i$ (i = reactants, products, or internal standard)

The minimum of G_{mix} is found when the derivative of this equation becomes zero. A similar approach can be applied for more complex systems with multiple phases as well.

The main goal of using this model is to help calculating the multi-reaction combinations. Hence, the calculations with the RGibbs model are in essence thermodynamic calculations for the equilibrium constants of a multi-reaction combination, which is difficult to be carried out manually. By defining the flow composition together with total pressure and temperature, the outlet gas compositions can be computed with equilibrium constants which have been automatically calculated by Aspen Plus at backstage. The outlet gas compositions in such calculations are only affected by reaction temperatures and inlet gas compositions, and there are no influences from catalysis-relating conditions (such as "reactor scale", "gas space velocity", "residence time of reactants on the catalyst surface" and "types of the catalyst bed") taken into consideration.

3.1.3 Software Manual of Aspen Plus (V7.3.2)

After opening Aspen Plus, the initial interface is shown in Figure 3.1. A new simulation project is started by clicking "new..." and then a double clicking on "Blank Simulation" option in the pop-up window.

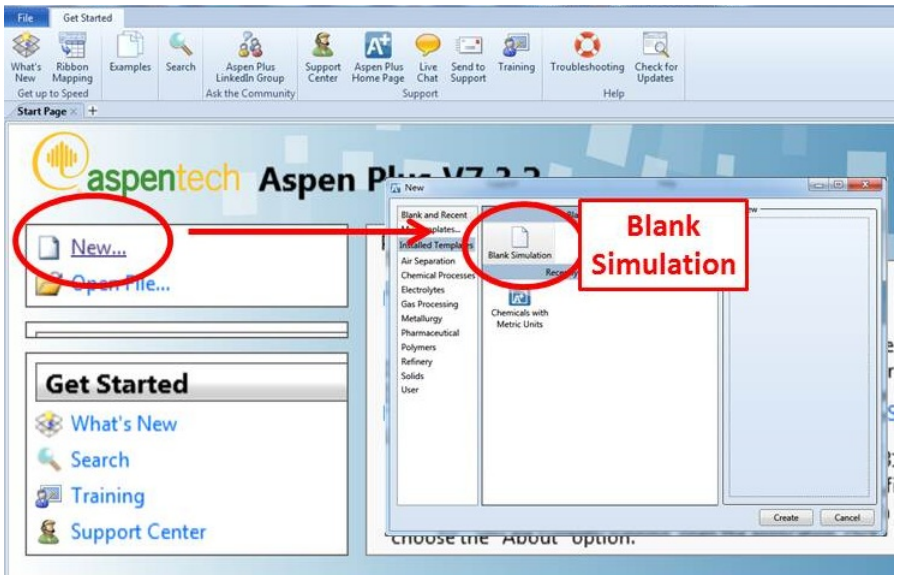

Figure 3.1: Step 1: Start a blank simulation.

The main interface comes out after starting a new simulation project (shown in Figure 3.2).There are two major sections named as "Properties" and "Simulations".

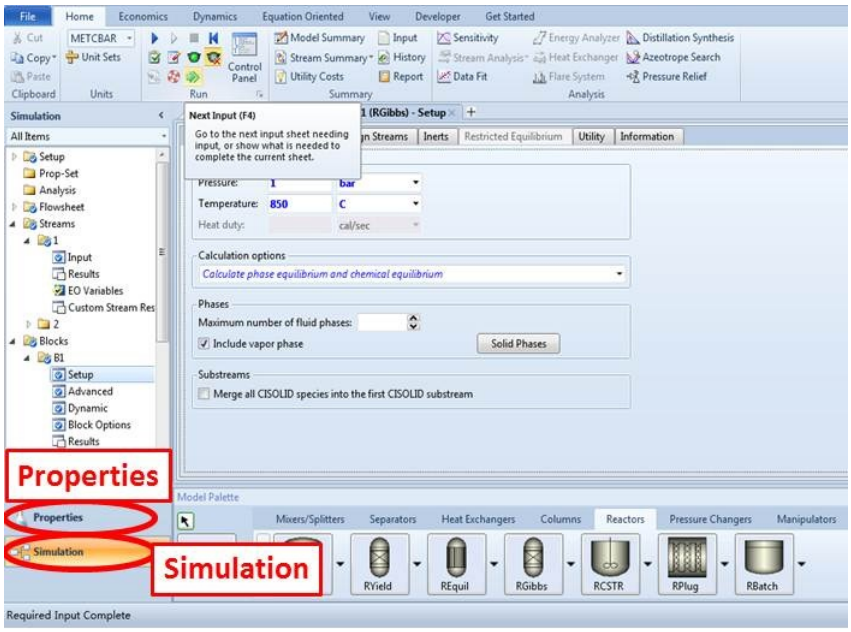

Figure 3.2: The main operational interface of Aspen Plus.

The "Properties" section is where all "participating components" (reactants, products and internal standards) are looked up from the Aspen database. The selected components are put onto a list from which the process won't contain any substances out of the range. In other words, this selection list must be comprehensive to include all possible components appeared during the process, or the calculation results will become false. As shown in Figure 3.3, the participating components are looked up in the "Properties" section by clicking "Components"→"Specifications"→"Find". In the pop-up window, enter the alias of components in the blank before clicking "Find Now", and then select the right component in searching result and click "Add selected compounds".

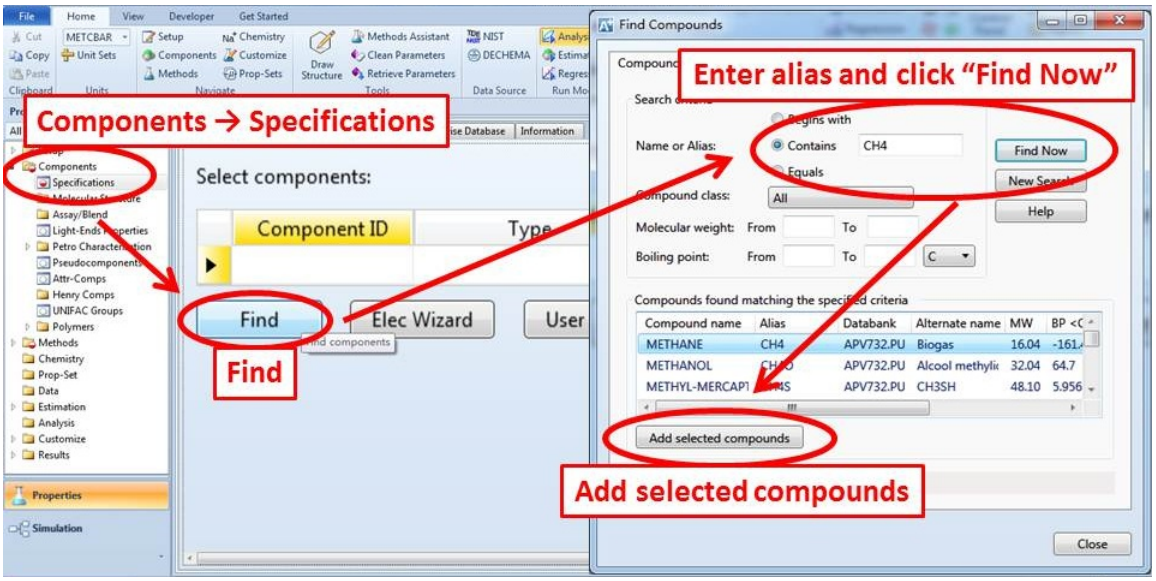

Figure 3.3: Step 2: selecting the participating components for a process.

The base method is also selected in the "Properties" section (Figure 3.4). The base method interface comes out by clicking "Methods"→"Specifications". In this thesis, the base method is kept as "NRTL" by selecting from the drop-down menu. "NRTL" is the base method which defines that all reactions are simulated under Ideal Gas Principle and Henry's Law.

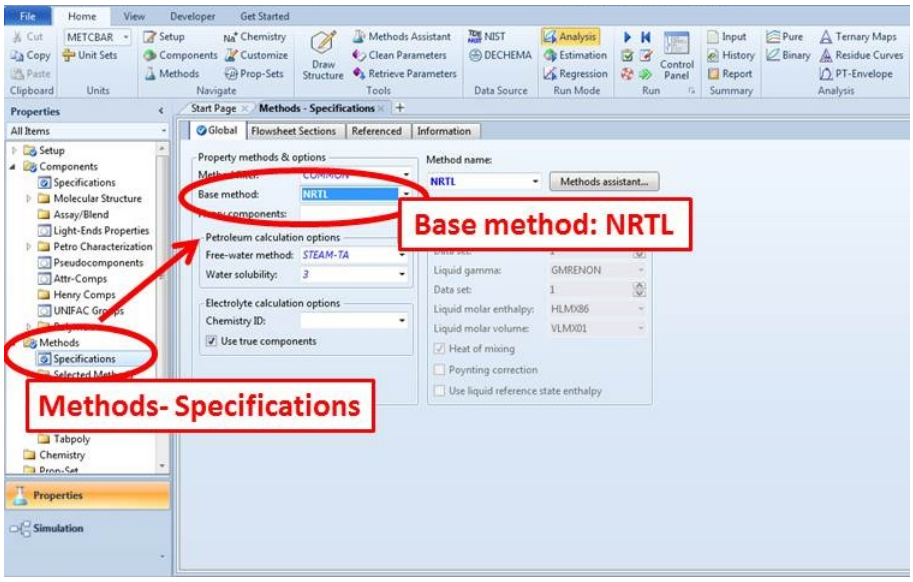

Figure 3.4: Step 3: selecting the base method as NRTL.

In the "Simulation" section, a RGibbs model (named "Block 1" or "B1") is applied with an inlet flow (named "1") and an outlet flow (named "2"). The set up procedures are displayed in Figure 3.5. The RGibbs model is drawn in the "Main Flowsheet" by clicking the tag "Reactors" underneath and the "RGibbs" button (shown as "Phase 1"). The inlet/outlet flows are drawn by clicking "Material". These flows are allocated by clicking the small red arrows which show the flow directions (shown as "Phase 2").

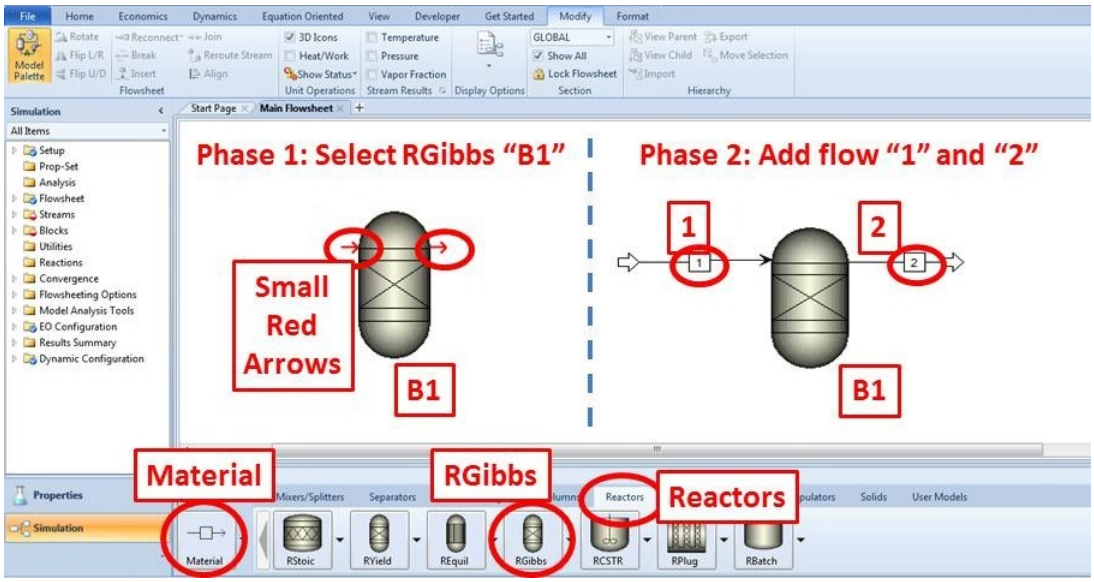

Figure 3.5: Step 4: RGibbs model and the inlet/outlet flows.

The variable interface of the inlet flow ("1") is reached to by clicking "Streams"→"1"→"Input" (shown in Figure 3.6). In this interface, temperature (in °C), pressure (in bar) and total flow rate (in kmol/h) of the inlet flow "1" are set in the left panel, whilst the composition of inlet flow is defined in the right panel by giving fractional flows (in kmol/h) to the gases in the participating component list.

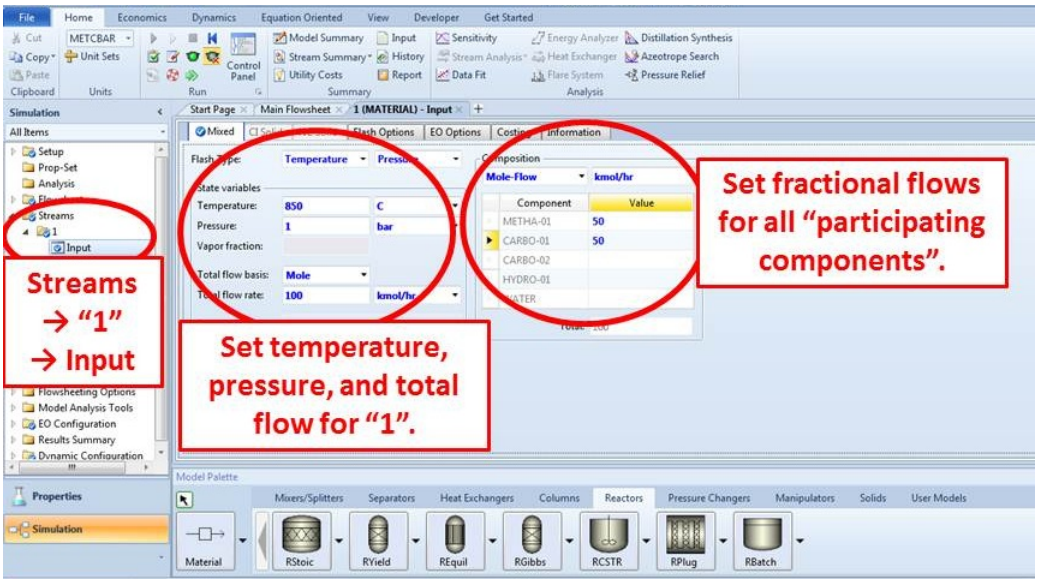

Figure 3.6: Step 5: setting variables for the inlet flow "1".

The variable interface of the RGibbs reactor ("B1") is reached to by clicking "Blocks"→"B1"→"Setup" (Shown in Figure). In this interface, operating conditions in the reactor, total pressure (in bar) and temperature (in ℃), are set consistent to the values in the inlet flow settings in Figure 3.6.

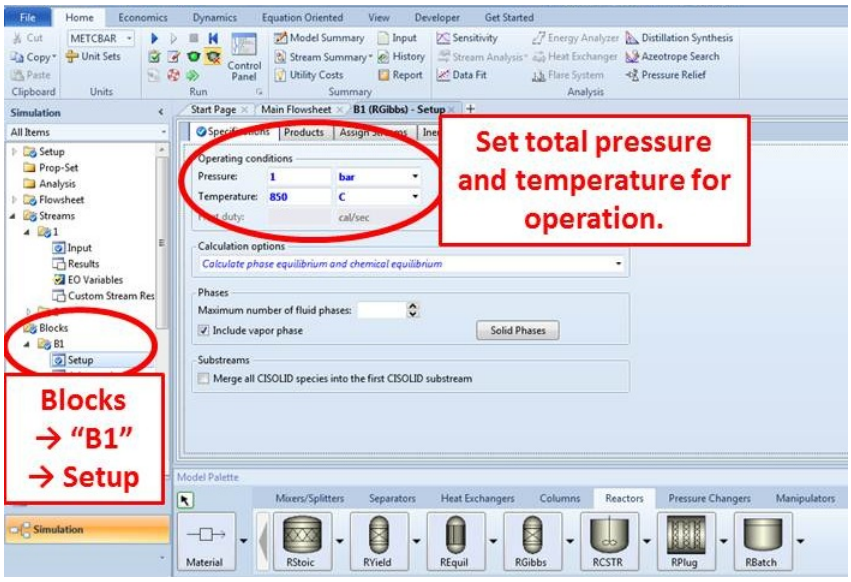

Figure 3.7: Step 6: setting variables for the RGibbs reactor.

The simulation running is applicable only when all required input is complete. Click the green arrow ("next input") on the top (shown in Figure 3.7) to check the input completion and click "OK" in the pop-up window for the data output.

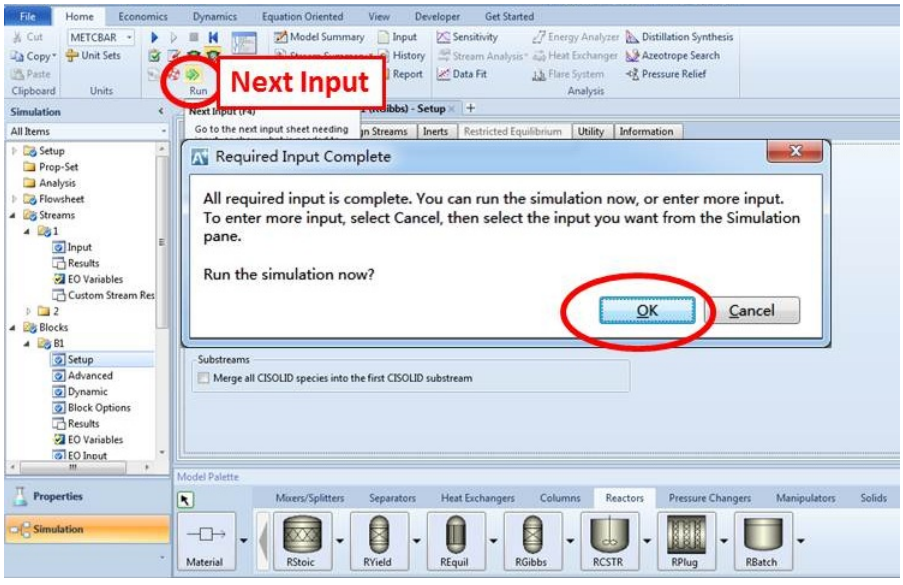

Figure 3.8: Step 7: complete required input and continue to the simulation running.

In Figure 3.9, the simulation results are displayed in the form of fractional flows in the outlet flow "2". These data can be achieved by clicking "Stream"→"2" and the tag "2 (MATERIAL) - Results". The data are output in the form of the fractional flow rates for each participating components (in kmol/h). These data can be translated directly to gas composition by dividing every fractional flow against the total outlet flow, and also the more interpreted results, such as reactant conversion and product yield, can also be calculated out.

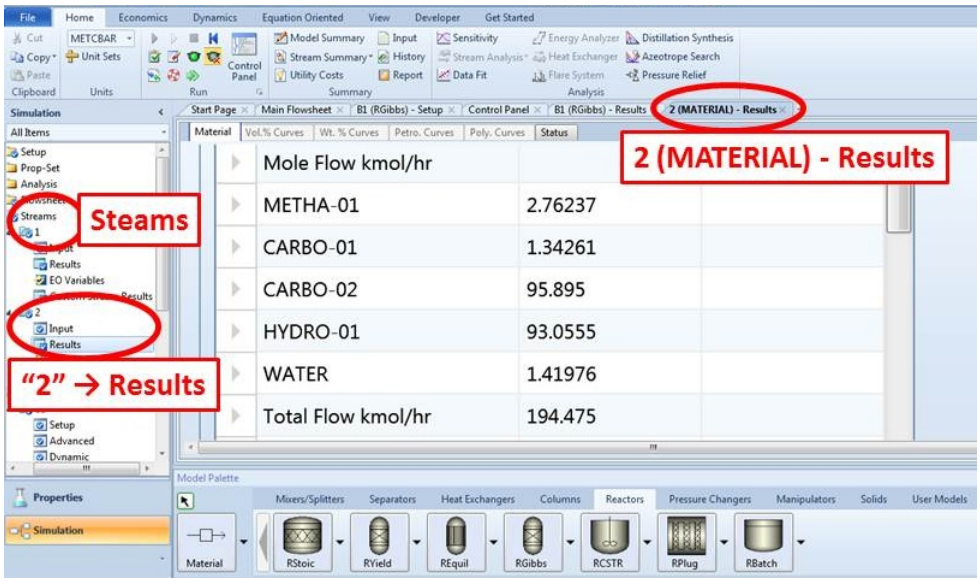

Figure 3.9: The formation of the Aspen simulation results.

3.2 Preparation of Catalysts

3.2.1 The Commercial Chemicals Used in this Thesis

Table 3.1: The List of Commercial Chemicals Used in this Thesis

Chemical Formula	Supplier	Purity%	Product Code	Use
ZrO_2	Alfa Aesar		43815	Catalyst Support
$(NH_4)_6Mo_7O_{24} \cdot 4H_2O$	Sigma-Aldrich	98	A7302	precursor of Mo oxides
$Co(NO_3)_2 \cdot 6H_2O$	Sigma-Aldrich	≥98	239267	precursor of Co oxides
$Cr(NO_3)_3 \cdot 9H_2O$	Sigma-Aldrich	99	239259	Precursor of Cr oxides
$La(NO_3)_3 \cdot 6H_2O$	Sigma-Aldrich	≥99.0	61520	precursor of La oxides
$Ce(NO_3)_3 \cdot 6H_2O$	Sigma-Aldrich	≥99.0	22350	precursor of Ce oxides
$Pr(NO_3)_3 \cdot 6H_2O$	Sigma-Aldrich	99.9	205133	precursor of Pr oxides
$NaNO_3$	Sigma-Aldrich	≥99.0	S5506	precursor of Na oxides
KNO_3	Sigma-Aldrich	≥99.0	P8394	precursor of K oxides

3.2.2 Zirconium Oxide (ZrO_2) as Catalyst Support

The "Support Effect" is very important in heterogeneous catalysis [2–4]. Different types of support not only influence the dispersion of the metallic catalysts but also determines the adsorption of reactants with its own acidic and basic sites. Acid sites on catalyst surfaces are well known to be important adsorption centre, first capturing and then activating hydrocarbons [5, 6], and the extent of adsorption directly affects the performance of catalysts. While the surface basicity is defined to enhance the CO_2 chemisorption because it is usually quantified via Temperature Programmed Desorption of CO_2 (CO_2-TPD), which may give merits to the utilisation of CO_2 in the catalysis process. The acidity and basicity of ZrO_2, SiO_2, Al_2O_3 and TiO_2 are listed in the following Table 3.2. It is clear that ZrO_2 and $\gamma - Al_2O_3$ have both high acidity and basicity sites on their surface, which shows ZrO_2 as one of the the most typical amphoteric support. Hence in all projects, ZrO_2 was applied as the major support when designing catalysts and others metal oxides will be used occasionally as comparisons.

Table 3.2: The acidity (indicated via NH_3-TPD) and basicity (indicated via CO_2-TPD) of ZrO_2, SiO_2, γ-Al_2O_3 and TiO_2. [6]

Catalyst support	NH_3-TPD ($mmol/g$)	CO_2-TPD ($mmol/g$)
ZrO_2	0.40	0.08
SiO_2	0.13	0.01
Al_2O_3	0.41	0.07
TiO_2	0.30	0.06

Due to sintering, the grain size of a catalyst support will be significantly changed during the high temperature calcination. On the other hand, the pre-heating of catalyst support is necessary to remove the moisture. Hence, the pre-heating of a catalyst support will be the first step of the sample preparation before grinding it into a certain particle size.

3.2.3 Wetness Impregnation Method to Dope Metal Oxides on Catalyst Supports

A metal oxide is the most common doping substance over the surface of a support. The oxide itself can perform as a semiconductor to transfer electrons as its working mechanism. In addition, it is also the precursor of dispersed metal, metallic carbides or sulfides on the catalyst surface. To achieve dispersed metal oxides doped on the support, the general method is as follows:

(1), Mix pre-treated support powders with a solution of precursor salts which contains the required elements (salts, such as nitrates or carbonates, are usually soluble in 20ml water);

(2), Stir for 24 hours to achieve a uniform suspension;

(3), Dehydrate the mixture to a paste at 120℃;

(4), Calcine the paste in air, the temperature is usually not lower than the operating temperature of the following catalytic test reactions, but the ammonium molybdate precursor (in Table 3.1) can only be calcined below 500℃ due to a possible sublimation of

MoO_3 when the temperature is too high;

(5), Grind the calcined solid into particles ($<125\mu m$, measured by sieves) and store it in specimen tubes.

3.2.4 Carburisation of Supported Oxide-Based Materials

In this project, Dry Methane Reforming (DMR) in Chapter 5, the metal and bi-metal carbides were applied as catalysts. Supported oxides were utilised as the precursor of the carbide catalysts and prepared following the method given in section 3.2.2.

To carry out the carburisation, a specific system based on a tubular furnace was built up as shown in Figure 3.10.

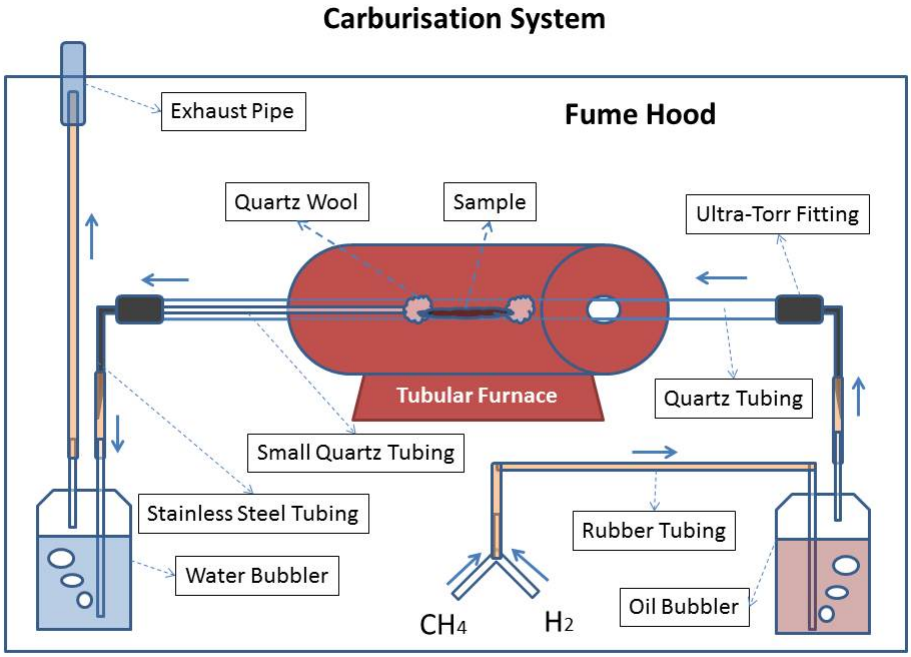

Figure 3.10: Schematic Diagram of the Designed Carburisation System.

Typically to obtain carbide materials, temperature programmed reduction (TPR) was

used. The prepared oxide precursors were carburised in a quartz tube under a gas flow of CH_4/H_2 ($8ml/min$ to $32ml/min$) for 3 hours at 750℃ to which the ramping rate was 3℃/min. The two bubblers displayed in Figure 2.1 are filled with non-volatile oil and water respectively. The oil bubbler is set to fully mix the CH_4/H_2 gas with a turbulence above the liquid before enter the quartz tubing; while the water bubbler is set to confirm that no problem (leaking/pressurizing) in this closed system. To fill the upstream bubbler with non-volatile oil is also to avoid any moisture introduction which may cause steam reforming of methane reaction. The carburised samples should be passivated in a low oxidising atmosphere for 48 hours to avoid a spontaneous combustion when the carbides are immediately exposed in air.

3.3 Catalytic Performance Testing

3.3.1 System

All catalytic activity tests were carried out in a micro-reactor (M-R-10A, KUNLUN YONG-TAI Company, China). The schematic diagram is shown in Figure 3.11. In this reactor, the gases from multiple cylinders are mixed for expected feedstock compositions before entering the reactor tube. On each inlet line, the gas flow rate is kept by a mass flow controller. A tubular furnace is set to heat up the reactor tube in its centre, before and after which are two pressure gauges measuring the "pressure drop" of the reactor tube. The outlet gases from the reactor tube is cooled down in a tank before entering the GC for gas composition measurements. This cooling tank is set to collect the possible liquid products at room temperature. However, this tank also lengthens the time period for stabilising the gas compositions before entering the GC, and hence the first GC measurements in every time-on-stream catalytic tests are 40 minutes after the reaction starts.

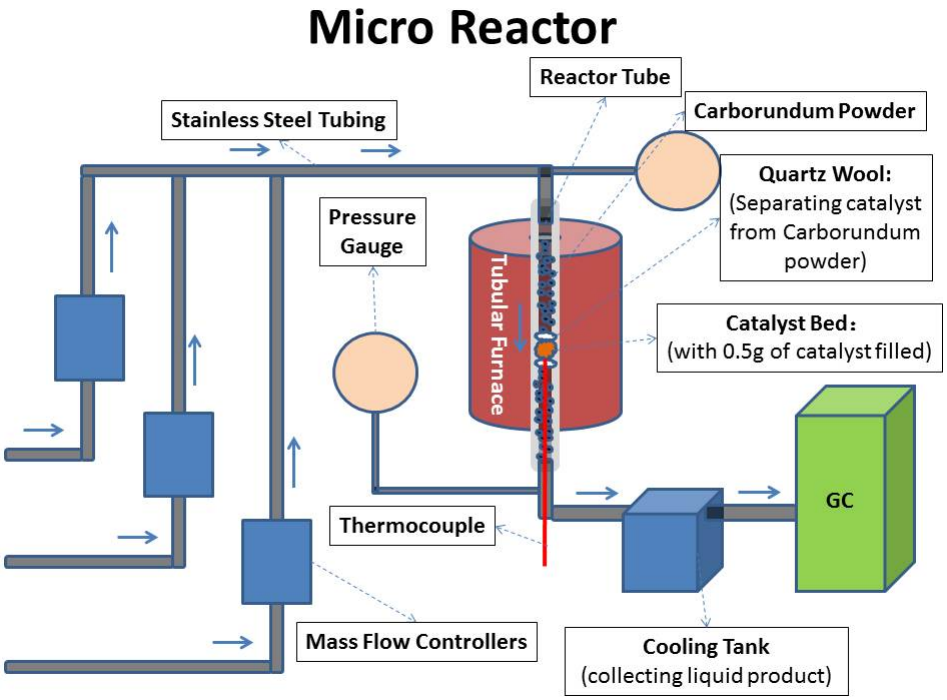

Figure 3.11: Schematic Diagram of the Micro Reactor and Online Gas Chromatograpghy.

Design and size parameters (in mm) of the reactor tube are shown in Figure 3.12. In the reactor tube, catalyst powder was placed at the middle position (catalyst bed). A thin inner cap is set for a thermocouple to measure the temperature of catalyst bed (at the middle) without influencing the reaction inside. Besides the catalyst powder, the 1mm-sized carborundum powder was used to fill the space below and above the catalyst bed (separated from the catalyst bed by quartz wool). The carborundum powder is not only for supporting the catalyst powder at the position without dropping but also can help making turbulence with the gap among these large particles. The turbulence is necessary in the reactor tube to fully mix the inlet gas mixture so that the gas flow has the compositions and heat distribution evenly.

There is an argument that the reactor in this scale is too large to be a micro-reactor (the micro one are in μm scale). Usually the tubes in this size are call mesoscale reactor

tubes. However, for avoidance of inconsistency throughout this thesis, micro-reactor is kept because it is the name given by the manufacturer designing this product.

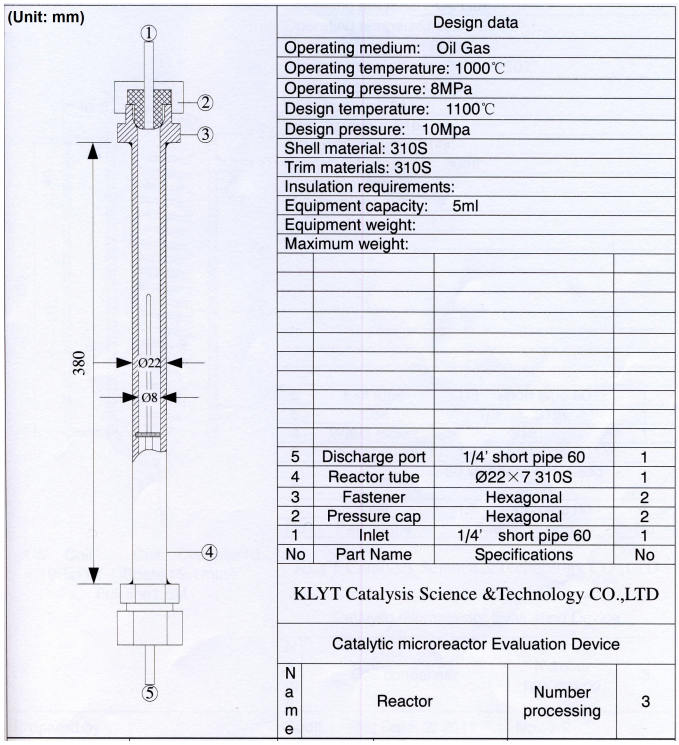

Design data			
Operating medium: Oil Gas			
Operating temperature: 1000℃			
Operating pressure: 8MPa			
Design temperature: 1100℃			
Design pressure: 10Mpa			
Shell material: 310S			
Trim materials: 310S			
Insulation requirements:			
Equipment capacity: 5ml			
Equipment weight:			
Maximum weight:			
5	Discharge port	1/4' short pipe 60	1
4	Reactor tube	Ø22×7 310S	1
3	Fastener	Hexagonal	2
2	Pressure cap	Hexagonal	2
1	Inlet	1/4' short pipe 60	1
No	Part Name	Specifications	No
KLYT Catalysis Science &Technology CO.,LTD			
Catalytic microreactor Evaluation Device			
Name	Reactor	Number processing	3

Figure 3.12: Design and size parameters of the customised reactor tube. (Adapted from product instruction of manufacturer.)

The calibrated amount of reactants were mixed with N_2 gas before purging through the reactor tube which had been heated up to target temperature. N_2 was not only acting as an internal standard which can help interpreting the raw reacting data to results (such as the reactant conversion or product selectivity), but also help easily diluting the reactants which would enhance the reactant conversion by changing its partial pressure (and this will be discussed later in Chapter 6). The outlet gas was cooled to room temperature and analysed by an online Gas Chromatography (GC).

3.3.2 Basics of Gas Chromatography (GC)

Gas Chromatography is an effective route to separate a mixed gas flow by forcing it to travel through a column [7]. The gas flow is forced to travel by an nonreactive carrier gas (the mobile phase), and the column is chosen such that different gaseous components of the mixture have differing levels of adsorption on the column inner surface (the stationary phase). A component which is more adsorbed on the column inner surface will take longer to travel through the column than a component which is less adsorbed on the column inner surface. As a result of these differences in mobility, the gas mixture will become separated from each other when travelling through the column. After the separation of gas mixture, components will be quantified in the form of peak one by one at their own "retention time" (a term of the time between sample injection and component's peak reaching a detector at the end of the column).

According to the different phase of the column inner surface, Gas Chromatography (GC) and Gas-Liquid Chromatography (GLC) are slightly different. In Gas Chromatography, the stationary phase is a microscopic layer of liquid or polymer on an inert solid support deposited on glass- or metal-type column. In Gas-Liquid Chromatography, the stationary phase comprises of a small amount of liquid held on a finely-divided inert solid support deposited on a column.

3.3.2.1 Method of GC

In this thesis, the gas products from reactions were separated and measured by 2 sets of columns and detectors. H_2, CO, CO_2 and N_2 were analysed by thermal conductivity detector (TCD) using a series of packed columns (1.2 m×3.2 mm OD) containing molecular sieves 5A, HayeSep Q and silica gel. TCD is commonly used in GC. This detector senses changes in the thermal conductivity of the column effluent and compares it to a reference

flow of carrier gas. Since most compounds have a thermal conductivity much less than that of the carrier gas (helium is used in this system), when an analyte eluted from the column the effluent thermal conductivity is reduced, and a detectable signal is produced. Hence, TCD has a wide range of gaseous compounds to be identified (except helium itself).

The hydrocarbons (C_1-C_5) were separated using a capillary column (30m×0.53mm COL C RT-Alumina) and analysed by flame ionisation detector (FID). FID is widely used in detecting hydrocarbons. The working of FID is based on the detection of ions formed during the combustion of organic compounds in a hydrogen flame. Hydrocarbons generally have molar response factors that are equal to number of carbon atoms in their molecule, while oxygenates and other species that contain heteroatoms tend to have a lower response factor (CO and CO_2 are not detectable by FID). Since the response intensity of hydrocarbons in FID is much higher than the one in TCD, the quantification of gaseous hydrocarbons are usually carried out with FID signals.

The parameters of the GC method are decried as follows:

1, **Total measuring time:** 18 minutes in total;

2, **Column temperature programme: a,** temperature held at 80℃ for 10min from the beginning; **b,** the column is heated up to 200℃ with a ramping rate of 25℃/min; **c,** temperature is held at 200℃ until the measurement stops;

3, **Carrier gas (helium) split:** 100ml/min split to the capillary column and FID; 30ml/min split to the packed columns and TCD;

4, H_2 **and Air for the FID flame:** 45ml/min of H_2 and 450ml/min of Air;

5, **Temperatures of detectors:** FID is kept at 250℃, whilst TCD is kept at 200℃.

3.3.3 Calibration and Quantification

Before starting all the catalyst testing reactions in the micro-reactor, the Catalysts Assessment System was calibrated by testing the mass flow controllers and re-calculating

quantitative standard curves of each related gaseous compound in GC.

The testing of gas flow is to double-check whether the mass flow controllers are working properly and stably. The real gas flow rate can be accurately measured by using bubble meter and stopwatch (the operation is shown in Figure 3.13). Usually, under the same setting number on a mass flow controller, gas mixture with different compositions will achieve different gas flow rates by volume. Hence, it is important to set the function of gas flow rates by volume with respect to setting number on a certain mass flow controller (called as Gas Flow Rate Calibration).

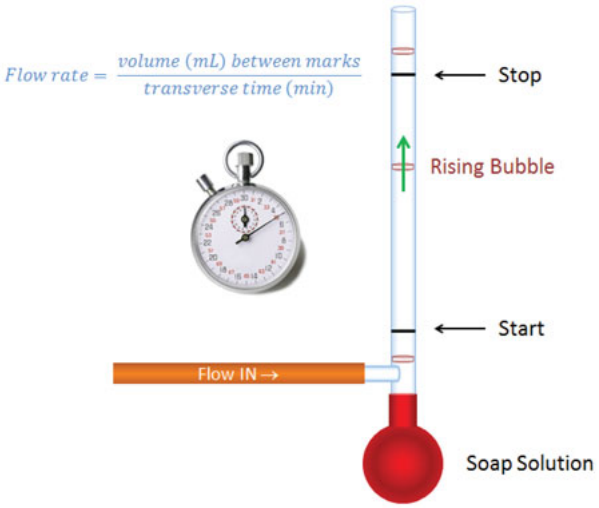

Figure 3.13: Schematic Diagram of Gas Flow Rate Calibration [8].

With the Flow Rate Calibration results, it is easy to mix different gases together with certain proportions. Since there exists a roughly linear relationship between the proportion of gas and their responsive intensities (integrated peak area) on GC detectors, it is straightforward to draw the quantitative standard curves for each gas as the functions of responsive intensities (integrated peak area) with respect to volume percentages of gas in a mixture. Hence, in the following experiments, the raw data (integrated peak area) can be routinely converted to the compositions of gases (in percentage) in a mixture which is

noted as X_i(i = gas identities) in this paper. Further interpretation of the data such as the calculation of reactant's conversion and product selectivity are all based on X_i. in the Appendix, the GC calibration method and sensitivity data are outlined in details.

3.4 Characterisation of Catalyst for Pre- and Post-Reaction Properties

The properties of catalysts both before and after the catalytic performance tests were measured by different characterisation methods.

3.4.1 X-ray Diffraction (XRD)

X-ray Diffraction is the most common characterisation method in solid state chemistry to measure the crystalline structure of a material.

3.4.1.1 Fundamental Principles

The working mechanism [9] is based on Bragg's Law, as shown in Figure 3.14.

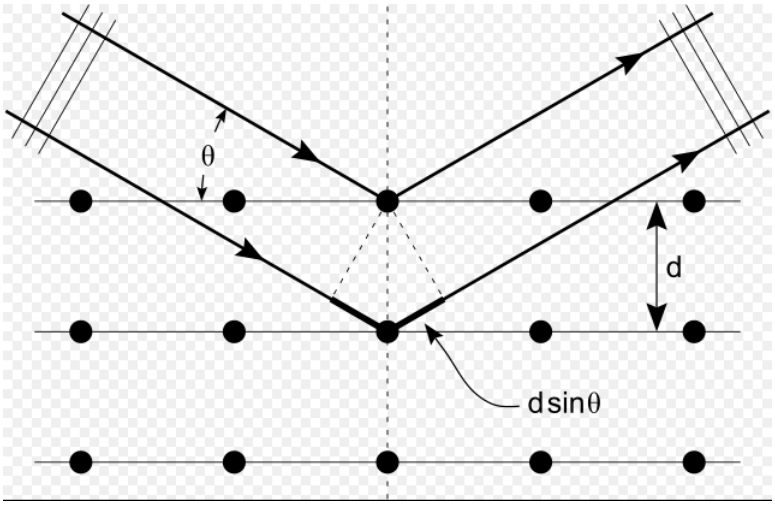

Figure 3.14: Bragg Diffraction on a Crystal [9].

When an X-ray strikes on an atom, it makes the electronic cloud move and this movement of these charges re-radiates waves with the same frequency. This phenomenon is known as Rayleigh scattering (or elastic scattering). In Bragg's Law, X-rays are partially scattered by atoms when they strike the surface of a crystal. The part of the X-ray that is not scattered passes through to the next layer of atoms, where again part of the X-ray is scattered and part passes through to the next layer.

Due to the regular array of atoms in crystals, regular array of scattered X-rays are formed. Although in most directions, these waves cancel one another through destructive interference, however in some specific directions they add constructively which is determined by Bragg's Law (**Eq.3.8**) [9].

$$n\lambda = 2d\sin\theta \quad \text{....Eq.3.8}$$

In this equation, d is the spacing between diffracting planes, θ is the incident angle, n is any integer, and λ is the wavelength of the incident X-ray. These specific directions appear as spots on the diffraction pattern called reflections. Thus, X-ray diffraction results from an electromagnetic wave (the X-ray) impinging on a regular array of scatterers (the repeating arrangement of atoms within the crystal).

It is theoretical and practical that different kinds of crystal will have their own series of spherical waves additions at specific value of θ, which is called patterns and each pattern is matched to a certain phase of crystal. Hence, with the standard database of XRD patterns for each typical crystallised compounds, it is possible to analyse the crystal structure. Moreover, slight changes of crystal structure can be recognised with the change of XRD patterns.

3.4.1.2 Specimen Preparation and Instrumentation

In this thesis, the PANalytical X'Pert PRO (or Empyrean) diffractrometer (shown in Figure 3.15) with CuKα radiation ($0.15418nm$) was used. To prepare the specimen for scanning, the sample powder should be ground to fine particle (which means no large fragments were mixed). The powder should be fully filled in a slot of the custom-built sample holder and the top surface of the powder pile should be kept flat, smooth and not over saturated to the slot.

Figure 3.15: PANalytical Empyrean diffractrometer.

To load the specimen, a specific stage for the spinner sample holders was attached on the diffractrometer and electronically connected in advance. The sample holder was fixed on the stage and the scanning programme was made by setting the scanning range (in 2θ), step size ($^\circ$), time per step (s), which were set in different values in various projects as the following Table 3.3:

Table 3.3: Instrumental settings of X-ray diffractrometers in different projects.

	In Chapter 5	In Chapter 6
Instrument	PANalytical X'Pert PRO	PANalytical Empyrean
Radiation	CuK_α (45kV, 40mA)	CuK_α (45kV, 40mA)
Scanning Range (in 2θ)	10° to 70°	20° to 30°
Step Size	0.0084°	0.0084°
Time per Step	$0.017778°s^{-1}$	$0.017778°s^{-1}$

The as received patterns were analysed by a supplementary software called X'pert Highscore which can match the patterns with its own database so that the components and crystal phases would be identified. By measuring the full width at half maximum (FWHM) of the peaks, the grain size of materials can be roughly estimated through Scherrer Equation (**Eq.3.9**) [9]:

$$\tau = \frac{K\lambda}{\beta \cos\theta} \quad \text{....Eq.3.9}$$

Where:

τ = the mean size of the ordered (crystalline) domains, which may be smaller or equal to the grain size, in nm;

K = a dimensionless shape factor, with a value close to unity. The shape factor has a typical value of about 0.9;

λ = the X-ray wavelength, in nm;

β = the line broadening at half the maximum intensity (FWHM), after subtracting the instrumental line broadening, in rad;

θ = the Bragg angle, in °.

3.4.2 Laser-Raman Spectroscopy

Raman Spectroscopy relies on inelastic scattering of monochromatic light on a material's surface, which is an efficient method to analyse the material surface for the special proper-

ties.

3.4.2.1 Fundamental Principles

When a monochromatic laser strikes on the surface of a matter, the electrons of atoms on the surface can absorb the energy of photons and then re-radiate a mixed frequency of light. This phenomenon is called scattering. Mostly, the frequencies of radiation is the same as the laser (photons contain same energy), which is called Rayleigh Scattering; while the energy of re-radiated photons in a minor fraction of scattering are shifted up or down, and the frequency of the scattered light is changed, which is called Raman Scattering.[10] The energy state changes for different kinds of scattering are displayed in Figure 3.16.

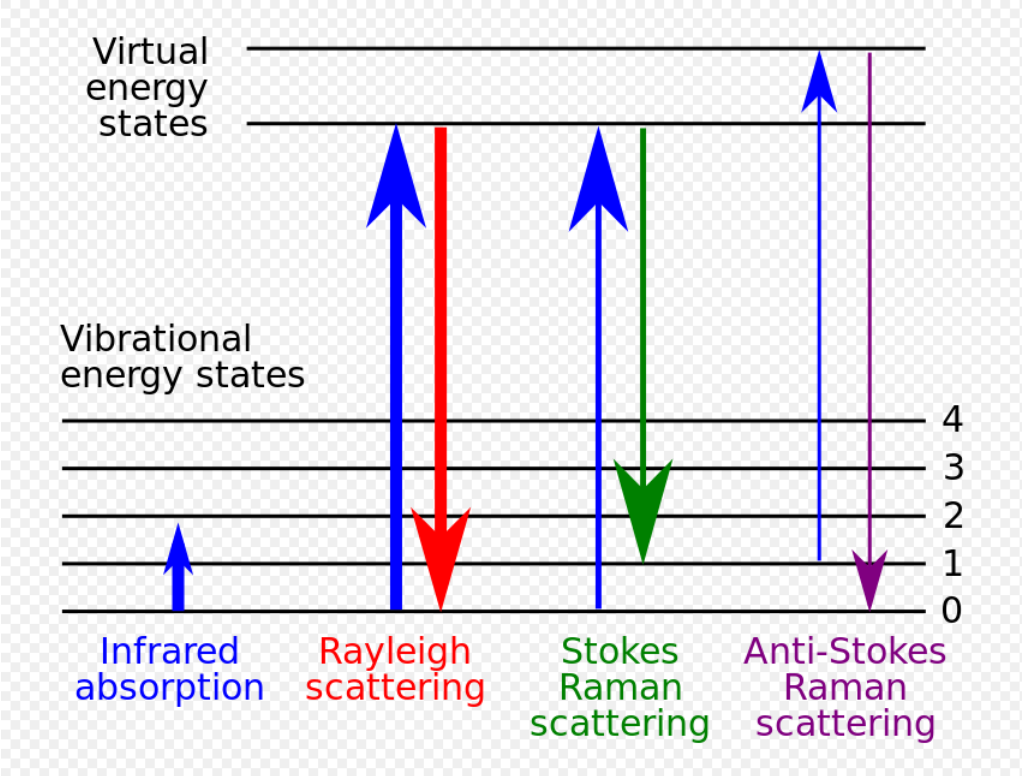

Figure 3.16: The Energy State Change of Different kinds of Scattering [11].

In a typical Raman scattering, a photon excites the molecule in neither the ground energy state nor an excited state. This results in the molecule being in a so-called virtual energy state for a short period of time before an inelastically scattered photon results. The resulting inelastically scattered photon which is "emitted"/"scattered" can be of either lower or higher energy than the incoming photon, resulting the molecule transited to a rovibronic state which is a different rotational or vibrational state than the one in which the molecule was originally. If the final vibrational state of the molecule is more energetic than the initial state, the inelastically scattered photon will be shifted to a lower frequency for the total energy of the system to remain balanced. This shift in frequency is designated as a Stokes shift. While if the final vibrational state is less energetic than the initial state, the inelastically scattered photon will be shifted to a higher frequency, and this is designated as an anti-Stokes shift. Raman scattering is an example of inelastic scattering because of the energy and momentum transfer between the photons and the molecules during the interaction. It is easy to imagine that most molecules are at ground energy state rather than the rotational/vibrational states at room temperature, so there are much more signals from Stokes shift than the anti-Stokes shift, and hence in most cases, we only pay attention to the Stokes shift (positive value of frequency shift) in Raman spectroscopy.

Since the working mechanism is to collect shift signals from the scattering of light, it is acceptable to assume that Raman spectroscopy is a method to characterise the surface properties of materials.

3.4.2.2 Specimen Preparation and Instrumentation

To prepare the specimen for Laser-Raman spectroscopy, the commonly normal microscope slides can be regarded as the sample holders. A tiny amount of sample (about $10mg$) was loaded on a glass slide and gently compressed by another glass slide to achieve a flat top surface.

The characterisation via Laser-Raman spectroscopy were carried out on a PerkinElmer RamanStation^{TM} 400F spectrometer (shown in Figure 3.17), which has an excited laser at 785nm in frequency. The specimens were loaded on a slot (fitted with the microscope slides) of this equipment. Using the camera and sample stage controller, the exciting spot can be precisely focused at very small range. The scanning method includes the laser power (in percentage), scanning range (in wavenumber, cm^{-1}), exposure time per scan (in seconds, s), repeat times. The laser power not only affects the intensity of a certain band (both positive or negative effects are possible) but also massively shifts some typical bands under certain scenarios, which means the consistency of methods should be kept as much as possible when measuring samples within the series.

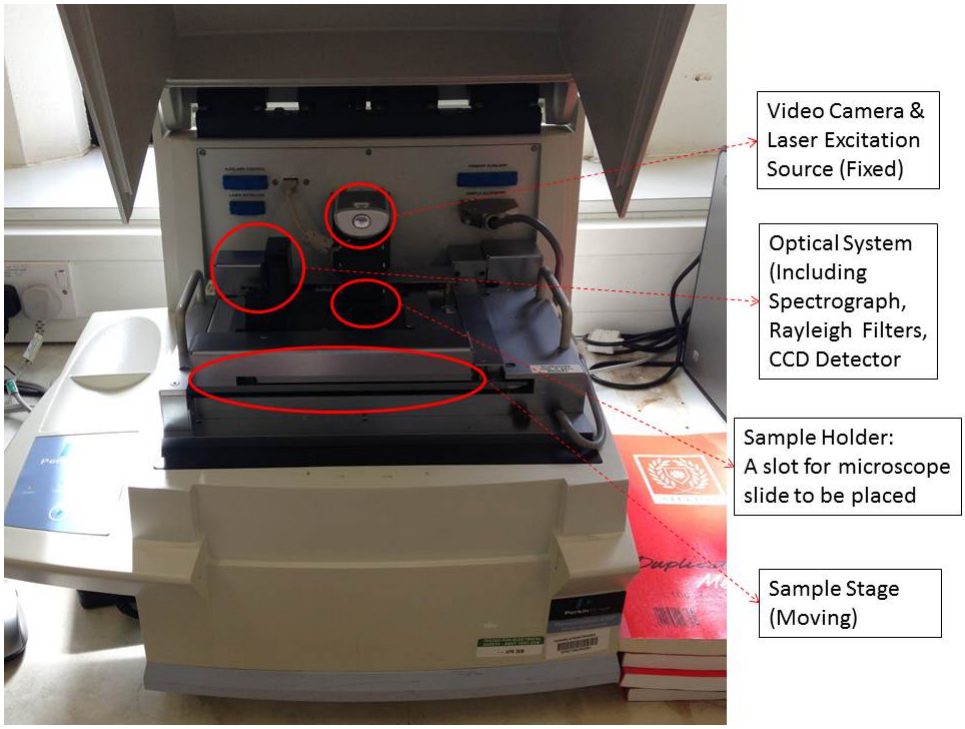

Figure 3.17: PerkinElmer RamanStation^{TM} 400F spectrometer.

3.4.3 Fourier Transform Infrared Spectroscopy (FT-IR)

Infrared Spectroscopy is a characterising method based on similar theory as Raman spectroscopy but yields complementary information.

3.4.3.1 Fundamental Principles

Theoretically [7], infrared Spectroscopy is affiliated to absorption spectroscopy which is to measure how well a sample absorbs light at each wavelength, and based on the nature of infrared radiation, the absorption at different wavelengths are corresponding to the typical force inner or among molecules (such as chemical bonds). Different from the "dispersive spectroscopy" which measures how much of the monochromatic beam of light is absorbed, Fourier transform spectroscopy is a technology which shines a beam containing many frequencies of light at once, and measures how much of that beam is absorbed by the sample. The beam is modified to contain a different combination of frequencies, giving a second data point. This process is repeated many times. Afterwards, a computer takes all these data and works backwards to infer what the absorption is at each wavelength.

3.4.3.2 Specimen Preparation and Instrumentation

The specimens for FT-IR were prepared by making translucent KBr pellets. The to-be-analysed sample was mechanically ground and mixed together with potassium bromide (KBr) as support. The ratio of $sample/support$ is around 3/997, and the mixed powder is compressed with a specific tool set. The pressure to make translucent pellets will be 10 tons exerted for 20s. The amount of mixed powder to be compressed should be appropriate so that the pellet would be both semi transparent and have no cracks at the centre. Due to the strong water-absorbing property of KBr, which leads to strong signals from water, it is necessary to dehydrate KBr in ovens before mixing samples and thereafter keep it away from a wet atmosphere.

The spectra of atmosphere background should be tested before the first measurement on specimens, the method including the scanning range (in wavenumber, cm^{-1}) and the resolution (in wavenumber, cm^{-1}) should be kept the same for all of specimens. The as prepared pellets were fitted in a supplementary sample holder which held the pellet at the position where IR radiation was passing through. The results of FT-IR spectroscopy will be displayed as negative peaks in the unit of transparency ($T\%$), and a straightforward process, automatic baseline corrections, will screen out atmospheric background.

3.4.4 Thermal Gravimetric Analysis (TGA)

3.4.4.1 Fundamental Principles

Thermal Gravimetric Analysis (TGA) is a method of thermal analysis, in which changes in physical and chemical properties of materials are measured as a function of increasing temperature (with constant heating rate), or as a function of time (with constant temperature and/or constant mass loss) [10, 12]. TGA can provide information about physical phenomena, such as secon order phase transition, including vaporization, sublimation, adsorption and desorption. Likewise, TGA can provide information about chemical phenomena including chemisorption, dehydration, decomposition and solid-gas reactions [13, 14].

A differential thermal gravimetric curve, D-TGA, is generated as the first derivative of the weight with respect to temperature or time. The D-TGA curve can be used to provide both qualitative and quantitative information about the sample. Qualitative modes of analysis include fingerprinting a material and distinguishing between two or more overlapping reactions. Quantitative modes include peak height and temperature at maximum weight loss measurements.

3.4.4.2 Specimen Preparation and Instrumentation

The instrument employed was a TA Instrument, SDT Q-600 (shown in Figure 3.18). To prepare the specimen of TGA, a supplementary alumina crucible (resists up to 1500℃) should be calcined in air by high temperature plasma to ensure nothing left, or at least there is nothing potentially to change weight during the measurement process. This calcined crucible will be tared at the initial temperature (30℃) and in the constant flow of air (100ml/min) before putting roughly 20mg sample in it.

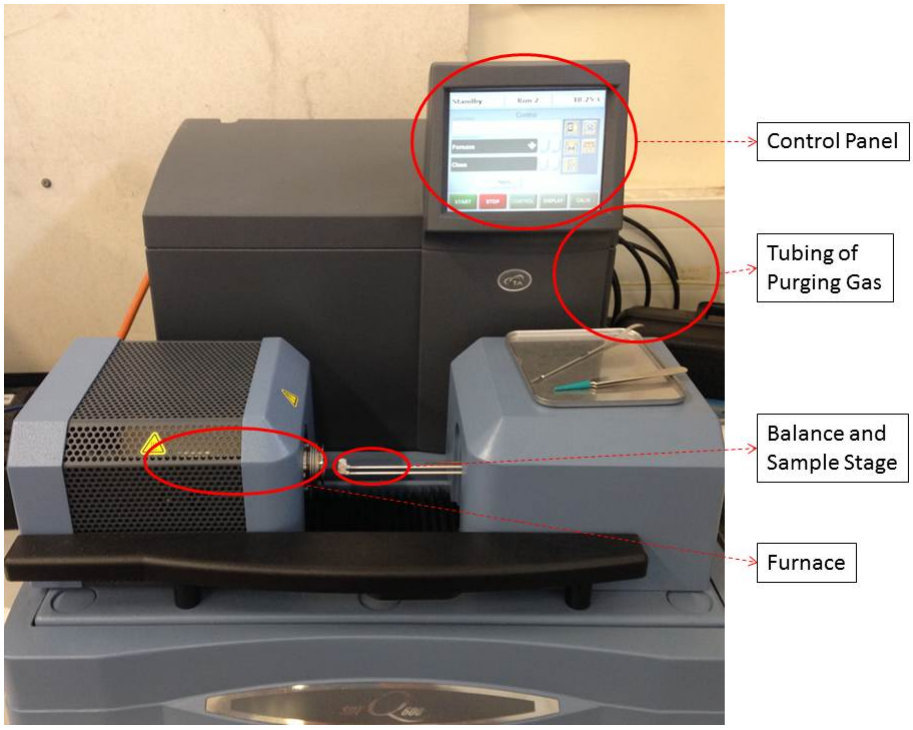

Figure 3.18: TA Instrument, SDT Q-600.

After the balance is stablised at a certain level at the initial temperature (30℃) and in the constant flow of air (100ml/min), the loaded crucible is automatically regarded as 100% of weight. The instrumental temperature is programmed to ramp towards 950℃ with the rate of 10℃/min. The whole heating programme is ended when the temperature reaches

950℃.

With different purposes, the atmosphere during the furnace heating-up of TGA is variable. Carbon containing species are usually able to be burned in air flow at high temperature, and hence the TGA in air is often used with the aim of measuring the coke generated during the processes. In Chapter 6, CO_2 and N_2 were also applied as atmosphere in TGA to discover any possible changes of materials under different atmospheres.

3.4.5 Brunauer, Emmett and Teller (BET) Surface Analysis

Brunauer, Emmett and Teller (BET) surface analysis is a method to measure the surface area of powder samples according to BET theory [15]. In this theory, the specific surface area of powders is determined by physical adsorption of a gas on the surface of the solid and by calculating the amount of adsorbate gas corresponding to a mono-molecular layer on the surface. Physical adsorption results from relatively weak forces (van der Waals forces) between the adsorbate gas molecules and the adsorbent surface area of the test powder. The determination is usually carried out at the temperature of liquid nitrogen. The amount of gas adsorbed can be measured by a volumetric procedure.

3.4.5.1 Theory and Specific Surface Area Determination

The concept of the theory is an extension of the Langmuir theory, which is a theory for mono-layer molecular adsorption, to multi-layer adsorption with the following hypotheses: (a) gas molecules physically adsorb on a solid in layers infinitely; (b) there is no interaction between each adsorption layer; and (c) the Langmuir theory can be applied to each layer. The resulting BET equation (**Eq.3.10**) is: [15].

$$\frac{1}{\left[V_a\left(\frac{P_0}{P}-1\right)\right]} = \frac{C-1}{V_m C} \times \frac{P}{P_0} + \frac{1}{V_m C} \quad \text{....Eq.3.10}$$

P = partial vapour pressure of adsorbate gas in equilibrium with the surface at 77.4 K (b.p. of liquid nitrogen), in Pa;

P_0= saturated pressure of adsorbate gas, in Pa;

V_a= volume of gas adsorbed at standard temperature and pressure (STP), in ml;

V_m= volume of gas adsorbed at STP to produce an apparent mono-layer on the sample surface, in ml;

C = BET constant which is related to the enthalpy of adsorption of the adsorbate gas on the powder sample.

A value of V_a is measured at each of not less than 3 values of $\frac{P_0}{P}$. Then the BET value $\frac{1}{\left[V_a\left(\frac{P_0}{P}-1\right)\right]}$ is plotted against $\frac{P_0}{P}$ according to the equation above. This plot should yield a straight line usually in the approximate relative pressure range 0.05 to 0.35. The data are considered acceptable if the correlation coefficient,r, of the linear regression is not less than 0.9975; that is, r^2 is not less than 0.995. From the resulting linear plot, the slope, which is equal to $\frac{C-1}{V_m C} = A$, and the intercept, which is equal to $\frac{1}{V_m C} = I$, are evaluated by linear regression analysis. From these values, V_m is calculated as $\frac{1}{A+I}$, while C is calculated as $\frac{A}{I} + 1$. From the value of V_m so determined, the specific surface area, S, is calculated by the equation: **Eq.3.11** and **Eq.3.12**[15].

$$S_{total} = \frac{V_m N_A \sigma}{22414} \times 10^{-18} \quad \text{....Eq.3.11}$$

$$S_{BET} = \frac{S_{total}}{m} \quad \text{....Eq.3.12}$$

S_{total} = surface area of sample, in $m^2 \cdot g^{-1}$;

S_{BET} = specific surface area of sample, in $m^2 \cdot g^{-1}$;

N_A= Avogadro constant ($6.022 \times 10^{23} mol^{-1}$);

σ = effective cross-sectional area of one adsorbate molecule, in nm^2 (0.162 nm^2 for nitrogen);

m = mass of the solid sample or adsorbent, in g.

22414= volume occupied by 1 mole of the adsorbate gas at STP allowing for minor departures from the ideal, in ml;

10^{-18}= exponential for the conversion from nm^2 to m^2;

3.4.5.2 Specimen Preparation and Instrumentation

Before operating the volumetric method, it is necessary in the sample preparation procedure to remove gases and vapours which can physically occupy the absorbing space, and this step is called "outgassing". Outgassing of many substances is often achieved by applying a vacuum, by purging the sample in a flowing stream of a non-reactive, dry gas, or by applying a desorption-adsorption cycling method. In either case, elevated temperatures are sometimes applied to increase the rate at which the contaminants leave the surface. In the volumetric method, the recommended adsorbate gas, nitrogen, is admitted into the evacuated space above the previously outgassed powder sample to give a defined equilibrium pressure, p, of the gas. Interfering effects of thermal diffusion are not necessary to be counted in this method since only pure adsorbate gas rather than a gas mixture is employed.

The instrument used to do BET measurements was the ChemiSorb 2720 from Micromeritics, and we would like to thank Guangzhou BOXENERGY Ltd. for the help of doing these characterisations.

Bibliography

[1] P. W. Atkins and J. de Paula. *Atkins' Physical Chemistry.* Oxford University Press, 7th edition, 2002.

[2] L. Basini and D. Sanfilippo. Molecular Aspects in Syn-Gas Production: The CO2-Reforming Reaction Case. *Journal of Catalysis*, 157(1):162–178, 1995.

[3] A. Erdöhelyi, J. Cserényi, E. Papp, and F. Solymosi. Catalytic Reaction of Methane with Carbon Dioxide over Supported Palladium. *Applied Catalysis A: General*, 108(2):205–219, 1994.

[4] B. Steinhauer, M. R. Kasireddy, J. Radnik, and A. Martin. Development of Ni-Pd Bimetallic Catalysts for the Utilization of Carbon Dioxide and Methane by Dry Reforming. *Applied Catalysis A: General*, 366(2):333–341, 2009.

[5] M. M. Bettahar, G. Costentin, L. Savary, and J. C. Lavalley. On the Partial Oxidation of Propane and Propylene on Mixed Metal Oxide Catalysts. *Applied Catalysis A: General*, 145:1–48, 1996.

[6] B. Xu, B. Zheng, W. Hua, Y. Yue, and Z. Gao. Support effect in Dehydrogenation of Propane in the Presence of CO2 over Supported Gallium Oxide Catalysts. *Journal of Catalysis*, 239:470–477, 2006.

[7] F. Rouessac and A. Rouessac. *Chemical Analysis: Modern Instrumentation Methods and Techniques.* John Wiley and Sons, Inc., 2nd edition, 2007.

[8] M. Klee. GC Solutions #34: Split Sample Introduction - Part 2: Measuring Flows, Liner Choice, Available at http://www.sepscience.com/Information/Archive/GC-Solutions/1636-/GC-Solutions-34-Split-Sample-Introduction—Part-2-Measuring-Flows-Liner-Choice (last access.

[9] M. M. Woolfson. *An Introduction to X-ray Crystallography*. Cambridge University Press, 2nd edition, 1997.

[10] E. N. Kaufmann. *Characterization of Materials*. John Wiley and Sons, Inc., 2nd edition, 2012.

[11] I. R. Lewis and H. G. M. Edwards. *Handbook of Raman Spectroscopy*. Taylor & Francis Group, LLC., 2001.

[12] J. P. Redfern and A. P. Coats. Thermogravimetric Analysis. *Analyst*, 88:906–924, 1963.

[13] G. Ma, Y. Shen, R. Gao, and X. Wang. Micromorphology and Adhesive Properties of Sulfonated Polyurethane/polyacrylate Emulsions Prepared by Surfactant-free Polymerization. *Journal of Polymer Research*, 24(3):36, 2017.

[14] S. Luo, F. Wang, K. Yu, J. Shao, L. Peng, and Q. Zeng. Enhancement of Visible-light Photocatalytic Activity of Cu3B2O6 Hybridized with G-C3N4. *Colloids and Surfaces A: Physicochemical and Engineering Aspects*, 520:409–419, 2017.

[15] S. Brunauer, P. H. Emmett, and E. Teller. Adsorption of Gases in Multimolecular Layers. *Journal of the American Chemical Society*, 60(1):309–319, 1938.

Chapter 4

Thermodynamic Analysis for CO_2 Utilisation Reactions

In an attempt to ameliorate the burgeoning growth in greenhouse gas emissions, there are currently intense efforts, world-wide, aiming at the utilisation of CO_2, particularly in its conversion to fuels and high-value chemical products. [1–5] Chemical processes aimed at the utilisation and conversion of CO_2 are, of course, driven in a thermodynamic sense by the difference in Gibbs Free Energy between the resulting final chemical products, and CO_2 and the targeted reactants at the relevant experimental conditions. However CO_2 being a highly stable molecule will require a substantial amount of energy, effective catalysts and optimised reaction conditions for any chemical conversion processes of CO_2 into the target of fuels or high-value chemical products.

Thus the overwhelming majority of reactions for CO_2 conversion and utilisation are endothermic and will consume considerable amounts of energy. If such energy is provided by fossil fuels, the net effect based on any well-to-wheels analysis of the process will invariably result in a net production of CO_2; utilisation of CO_2 could only be deemed beneficial from a climate mitigation perspective if the necessary input process energy is provided from

renewable or sustainable sources.

Hence, the motivation behind this work is to understand the thermodynamics and the nature of selected reactions in which CO_2 is involved, and hopefully find a route to improve the reaction results (e.g. higher reactant conversion or product selectivity) by changing the reaction conditions. Comparing to enhancing the catalyst performance, changing the reaction conditions is more responsive and adjustable in the real world. Of course, a relatively robust catalyst is a precondition of the improvement by modifying conditions.

4.1 Potential of the Dry Methane Reforming (DMR) to Substitute Steam Methane Reforming (SMR) in Industry

It is well known that DMR ($CO_2 + CH_4 \rightarrow 2CO + 2H_2$) is more endothermic and perhaps requires even higher operating temperatures when comparing to SMR ($H_2O + CH_4 \rightarrow CO + 3H_2$) and the latter has been industrialised as the main production route to H_2. Hence, the thermodynamic calculations are necessary, aiming to compare the potential of both reactions to be applied in reality.

The multi-reaction calculations for DMR using Aspen Plus was carried out, which will show more straightforward calculation results by displaying the conversion of reactants, selectivity of products and by-product generation at the equilibrium state. The conditions are set as: 300-900℃, atmospheric overall pressure, $CH_4 : Oxidant = 1 : 1$.

4.1.1 Modelled Reaction System

The modelled reaction systems for the DMR and the SMR are shown in Table 4.1. When talking about the catalytic mechanism of both DMR and SMR, it is generally accepted that methane is always first adsorbed, then activated and decomposed to carbon and H_2 (**R.4.1**) firstly on catalyst surface, and the second step will be the gasification of generated

carbon by CO_2 or steam as oxidants (**R.4.2** and **R.4.3**). Moreover, it is straightforward to find that the side-reactions of DMR and SMR respectively, **R.4.4** and **R.4.5**, are reversal to each other.

Table 4.1: Modelled reaction system for the DMR and the SMR

Reaction Step	DMR	SMR
Decomposition of Methane	$CH_4 \rightleftharpoons 2H_2 + C$....**R.4.1**	
Carbon Oxidation	$C + CO_2 \rightleftharpoons 2CO$....**R.4.2**	$C + H_2O \rightleftharpoons CO + H_2$....**R.4.3**
Side Reaction	$H_2 + CO_2 \rightleftharpoons H_2O + CO$....**R.4.4**	$H_2O + CO \rightleftharpoons H_2 + CO_2$....**R.4.5**

The order of reaction with respect to a given substance (such as reactant, catalyst or product) is the index, or exponent, to which its concentration term in the rate equation is raised. Elementary (single-step) reactions do have reaction orders equal to the stoichiometric coefficients for each reactant. The overall reaction order, i.e. the sum of stoichiometric coefficients of reactants, is always equal to the molecularity of the elementary reaction. Hoever, complex (multi-step) reactions, such as the DMR and SMR processes, may or may not have reaction orders equal to their stoichiometric coefficients. From the kinetic study carried out by former researchers[6], the reaction order of the DMR process was calculated based on the reaction results over a series of $Pt-Ni/Al_2O_3$ catalysts, the achieved reaction order values suggested a nearly second order of reaction in DMR but the reaction order is also influenced by the Pt/Ni ratio in the catalyst series. The kinetic study for the SMR process was carried out by Wang et al.[7] with both theoretical and experimental study. The results showed that the reaction order of methane may vary between 0.85 and 1.4, whilst the reaction order of steam can shift from 1 to 0 (or even becomes negative) by changing the steam-to-carbon ratio.

4.1.2 Thermodynamic Calculation Results

To carry out the thermodynamic calculations, the method has already been completely described in Chapter 3.1, and the following Table 4.2 displays the necessary chemical properties for the calculations.

Table 4.2: Standard thermodynamic properties of chemical substance (at 298.15K): Standard molar enthalpy of formation ($\Delta_f H_m^\theta$), standard molar entropy (S_m^θ) and parameters of molar heat capacity at constant pressure ($C_{p,m}$).

Substance	$\Delta_f H_m^\theta$(298.15K)[8] ($KJmol^{-1}$)	S_m^θ[8] ($JK^{-1}mol^{-1}$)	$C_{p,m}/R = A + BT + CT^2 + DT^3 + ET^4$[9].				
			A(10^0)	B(10^{-3})	C(10^{-5})	D(10^{-8})	E(10^{-11})
H_2	0	130.684	2.883	3.681	-0.772	0.692	-0.213
CO	-110.53	197.67	3.912	-3.913	1.182	-1.302	0.515
CO_2	-393.51	213.74	3.259	1.356	1.502	-2.374	1.056
H_2O	-241.82	188.83	4.395	-4.186	1.405	-1.564	0.632
CH_4	-74.81	186.26	4.568	-8.975	3.631	-3.407	1.091
C(graphite)*	0	5.74	-0.977	9.458	-1.118	0.739	-0.207
*: $C_{p,m}$ parameters were calculated by regressing molar heat capacity data in handbook.[10]							

The $\Delta_r G_m^\theta$ data of each single reaction in the modelled reaction system are calculated and displayed in Figure 4.1. The $\Delta_r G_m^\theta$ of the decomposition of methane reaction **(R.4.1)** reaches to the negative value at roughly 550℃, which is lower than any other single reactions, and this means the potential difference between DMR and SMR will be mainly decided by the carbon oxidation step (**R.4.2** and **R.4.3**). The $\Delta_r G_m^\theta$ value of **R.4.3** is always lower than **R.4.2**, which explains why SMR has the advantage than DMR in the aspect of operating temperature. However, when looking at the side-reaction (**R.4.4**) - always has positive value throughout the selected temperature range - also indicates that its reverse reaction **R.4.5**, which is the side-reaction of SMR, has the negative value meanwhile. This result can tell us at the equilibrium state, CO_2 and H_2 are more likely to be left in the system rather than CO and H_2O, and this is advantageous to DMR because less by-products would be generated as compared to SMR.

When discussing the relationship between the entropy changes and the "slope" of the

lines, the change of reaction in enthalpy can be regarded as a constant due to the negligible difference when temperature is changed at 300-500℃. Hence, the equation: $\Delta_r G_m^\theta = \Delta_r H_m^\theta - T \cdot \Delta_r S_m^\theta$ turns to be a linear function of T, and the "slope" is $-\Delta_r S_m^\theta$.

It is obvious that the $\Delta_r G_m^\theta$ of **R.4.5** has a positive slope while the other ones are all negative. From the discussion above we have already known that the "slope" of $\Delta_r G_m^\theta$ reflects the change of entropy of reaction, and a positive slope means a negative change of entropy during the reaction. Another information directly dragged from Figure 4.1 is that the positive slope leads to a positive value of $\Delta_r G_m^\theta$ as temperature rises. Hence, we can conclude that the potential of reactions with negative changes of entropy can be straightforwardly inhibited by increasing the temperature.

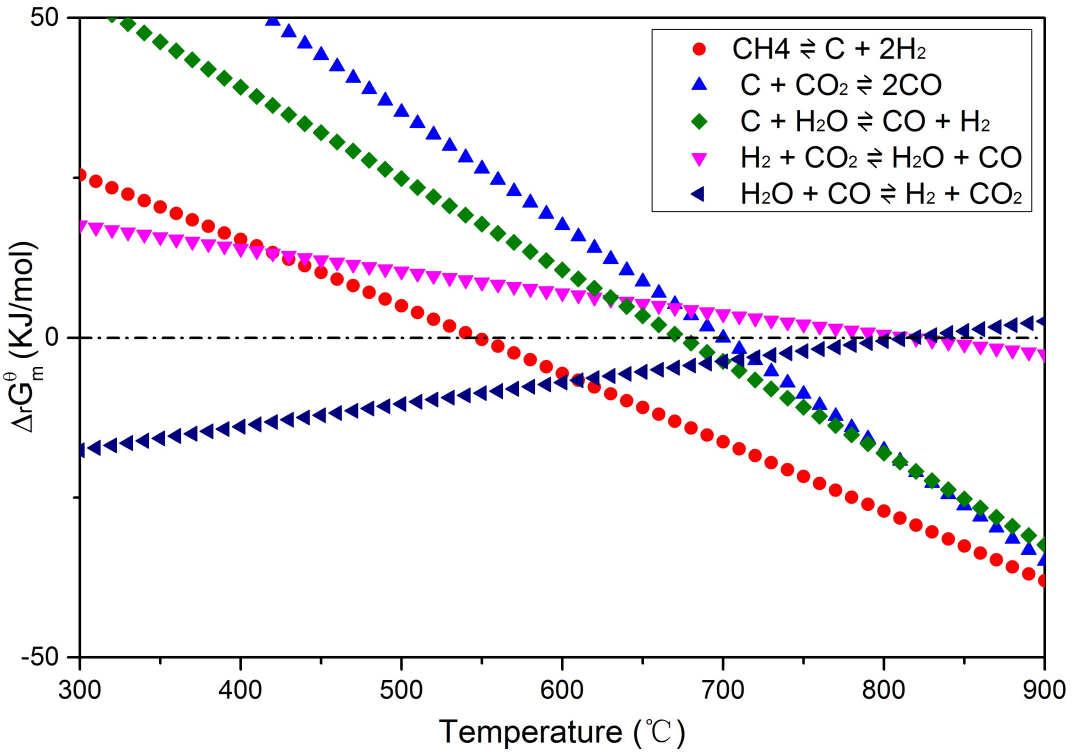

Figure 4.1: $\Delta_r G_m^\theta$ of the sub- and side-reactions for DMR and SMR systems (shown in Table 4.2) at 300-900℃.

4.1.3 Multi-reaction Calculation Results

The multi-reaction calculations for DMR and SMR were carried out using Aspen Plus software. The software calculation is based on the Gibbs free energy minimisation method (which is mentioned in Chapter 3.1.2), and the software manual is outlined in Chapter 3.1.3.

The multi-reaction calculation results carried out using Aspen Plus software can be easily interpreted to conversions and yields because the units of input and output chemicals are consistent (in mol/min). Here we define the "conversions of reactants" and the "yields of products" as following:

Conversion of reactant A: $C_A(\%) = \frac{F_A^{output}}{F_A^{input}} \times 100\%$

Yield of product B: $Y_B(\%) = \frac{F_B^{output}}{F_A^{input}} \times 100\%$

Where:

"A" stands for any kind of reactant;

"B" stands for any kind of product;

"F" stands for flow rate in mol/min.

Figure 4.2 and Figure 4.3 illustrate the conversions of reactants in SMR and DMR at equilibrium state. It is immediately apparent that at medium temperature (below 600℃), SMR is superior to DMR both in the aspects of CH_4 conversion and oxidant conversion. However, DMR catches up with SMR in relation to both aspects and the conversion of CO_2 overtakes the conversion of H_2O when the temperature reaches 700℃ or above.

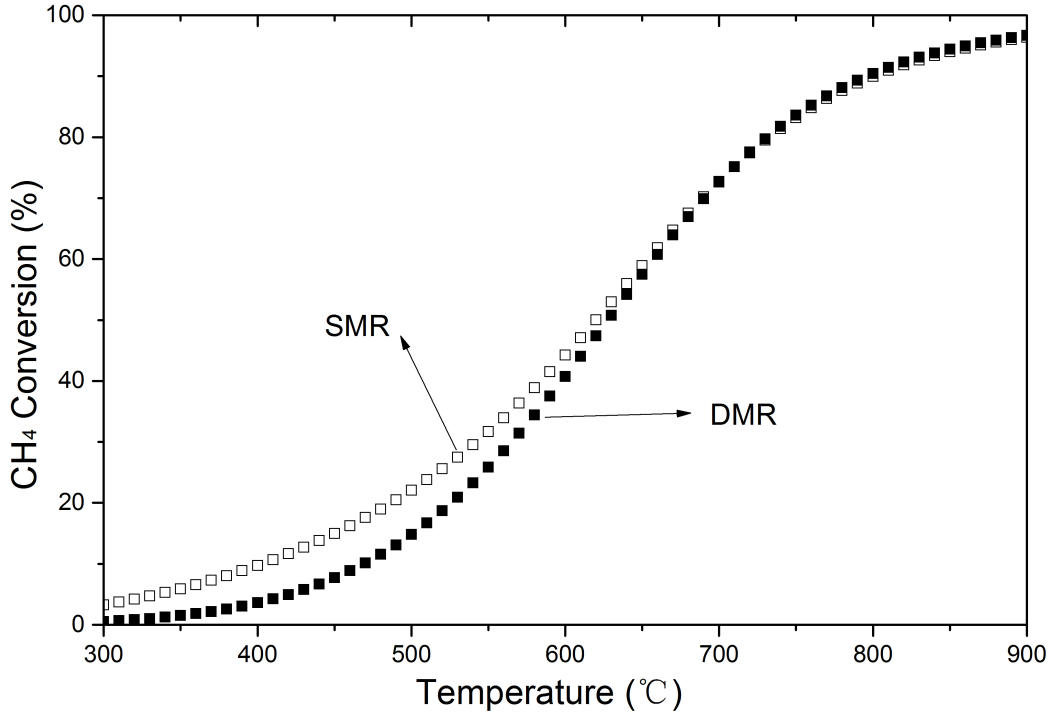

Figure 4.2: Theoretical CH_4 conversions of DMR and SMR at equilibrium state, 300-900℃. Based on multi-reaction calculation results using Aspen Plus.

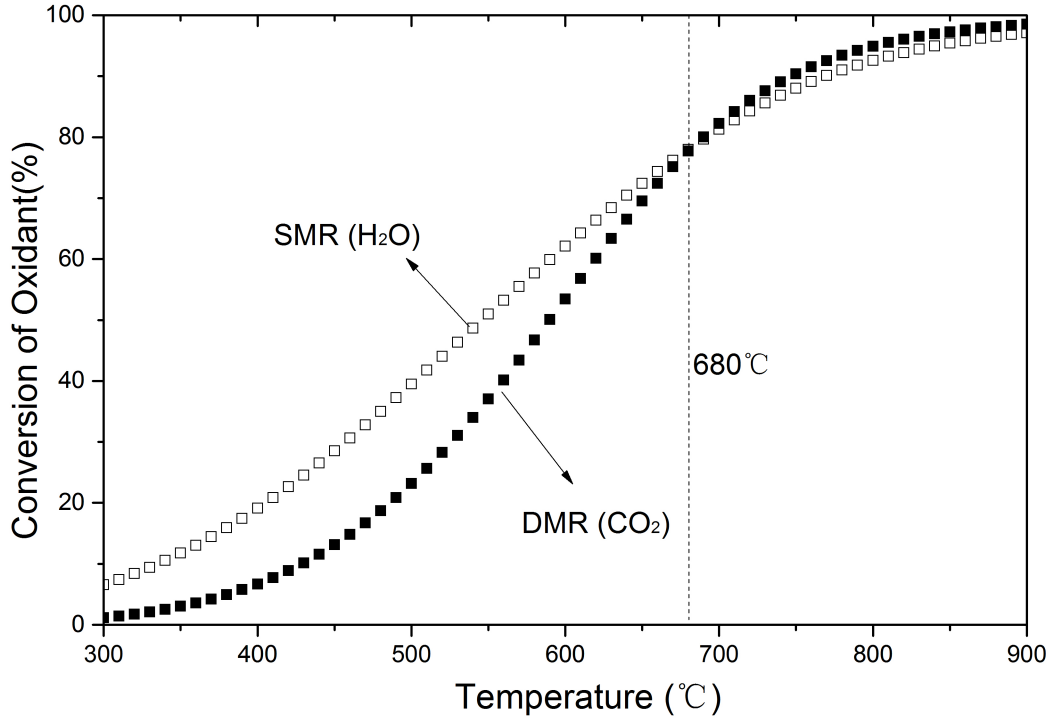

Figure 4.3: Theoretical oxidant's conversions (CO_2 in DMR and H_2O in SMR) at equilibrium state, 300-900℃. Based on multi-reaction calculation results using Aspen Plus.

Different from the conversions of reactants, DMR shows a much lower level of by-product generation than SMR as shown in Figure 4.4. This result matches to the thermodynamic calculation of the Reverse Water Gas Shift (RWGS, **R.4.4**) very well, and also, this is a strong support of DMR in the competition against SMR.

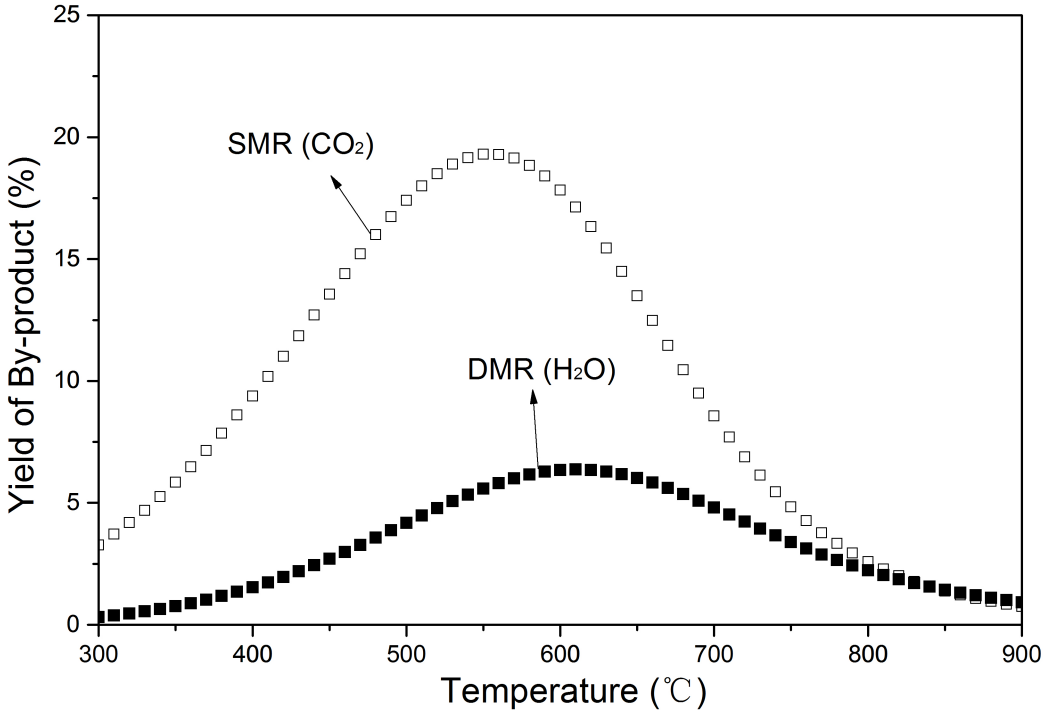

Figure 4.4: Theoretical by-product (H_2O in DMR and CO_2 in SMR) generations of DMR and SMR at equilibrium state, 300-900℃. Based on multi-reaction calculation results using Aspen Plus.

4.1.4 Discussion

Based on the thermodynamic calculation results together with some practical issue of SMR industrialisation, the merits and demerits between DMR and SMR to be applied in industry are listed in Table 4.3 as below. We can see the only commonly accepted advantage of SMR to DMR is the less endothermicity based on the calculated enthalpy change of reaction (ΔH).

The general belief that SMR has relatively lower operating temperature than DMR seems to be incorrect. Within the operating temperature at the range of 700-900℃ (at which SMR is usually carried out in industry in order to kinetically increase the reacting efficiency), DMR performs equal or even better than SMR in the perspective of reactants

conversions, and furthermore, DMR will generate much less by-product (H_2O) than SMR (CO_2). Importantly, this probably means DMR has higher potential than SMR at the range of temperatures where SMR is typically operated.

Table 4.3: Major issues between DMR and SMR when considering industrialisation.

Major Issues	SMR	DMR
Energy Consumption	$\Delta_r H_m^\theta = 206 KJ/mol$	$\Delta_r H_m^\theta = 247 KJ/mol$
Reactants Conversions	Better at 300-680℃	Equal or better at 680-900℃
By-product Generation	More	Less
Availability of Oxidants	Steam	CO_2

However, SMR is superior to DMR in any "decisive battle" from the aspect of oxidant resource. Interestingly, under the high concentration of oxidants as precondition (in order to be used in the real world), the capture and storage of CO_2 is much more expensive (in energy and monetary cost [11]) and difficult than heating water to steam even though H_2O looks more precious and useful than the famous greenhouse gas which we are trying to eliminate. The most practical problem for DMR to be industrialised is probably not the reaction performance and operating conditions but to find an economical source of CO_2 with relatively higher concentration. And one of the possible resolutions is to make a further usage of flue-gas.

4.1.4.1 The Effect on Reaction Performance via Diluting Reactants with N_2 (As a Mimic of a Flue-Gas Situation)

In a typical mixture of flue-gas, N_2 usually occupies the major proportion (over 60%), while CO_2, O_2 and H_2O share the remaining compounds (~30%) [12]. Hence, the issue to be discussed so far has been shifted to the effect on reaction performance of diluting reactants with N_2 from concentrating CO_2 in atmosphere.

Similar studies of DMR have been explored by Sun et al. under elevated pressure

of reactants [13]. They found an inhibited conversion of CH_4 and massive increase of coke formation when the system pressure reached $30bar$. However, it should be noticed that the DMR is overall a molecule-increasing reaction (the number of gas molecules at product side of the reaction is greater than the number at reactant side), and it should be thermodynamically favoured at relatively lower partial pressure of reactants. Hence in this project, the situation with lower partial pressure of reactants by diluting with N_2 has been simulated and discussed.

Figure 4.5 to Figure 4.7 show the multi-reaction calculation results using Aspen Plus of the reaction system, and it should be noticed that all of the values are the results when the system reaches to equilibrium state.

In Figure 4.5, both CO_2 and CH_4 conversions show the dilution of reactants by N_2 can effectively improve the reactivity of feedstock at any temperature, which is due to the partial pressure of reactants were decreased when the overall system pressure is kept constant (ambient). These results complementarily fit the trend calculated by Sun et al. [13] under situations of elevated pressure of reactants.

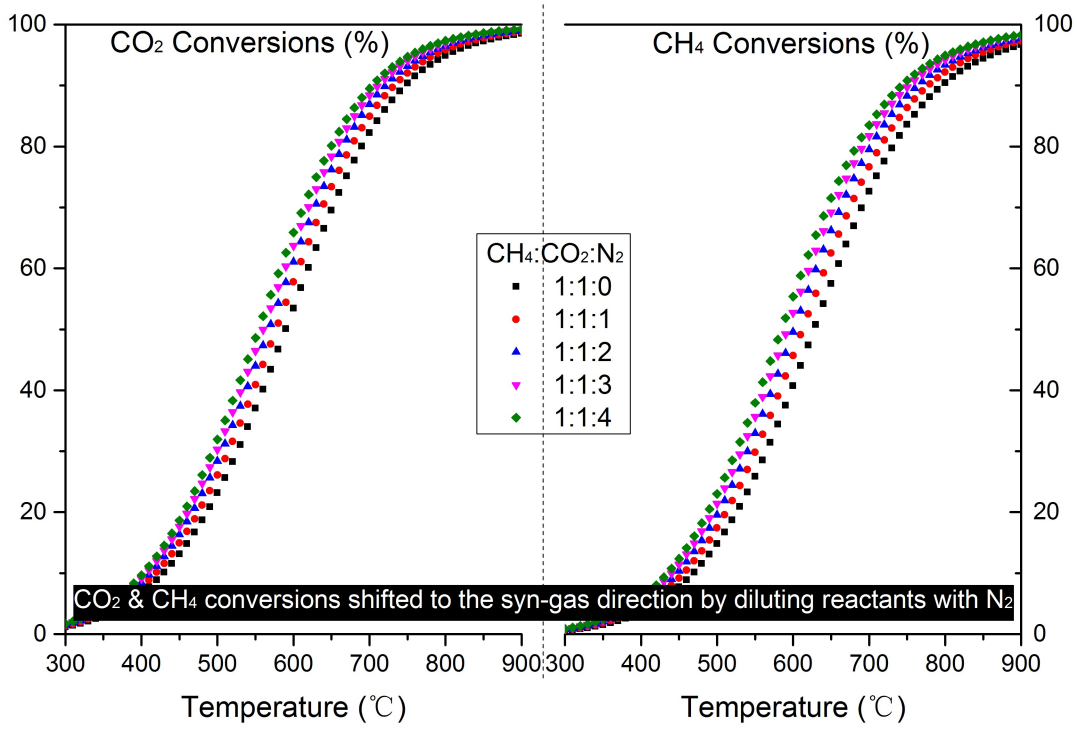

Figure 4.5: Calculated CO_2 and CH_4 conversions of the modelled system using Aspen Plus, 300-900℃, overall atmospheric pressure, various dilution of reactants by N_2.

When focusing on the H_2/CO ratio as shown in Figure 4.6, the resistance to the RWGS, **R.4.4** can be observed. Lower H_2/CO value indicates a higher domination of RWGS in the whole reaction system. It also can be observed that the dilution of reactants can effectively limit the facility of RWGS although this limitation reaches to high level only at 800℃ and above.

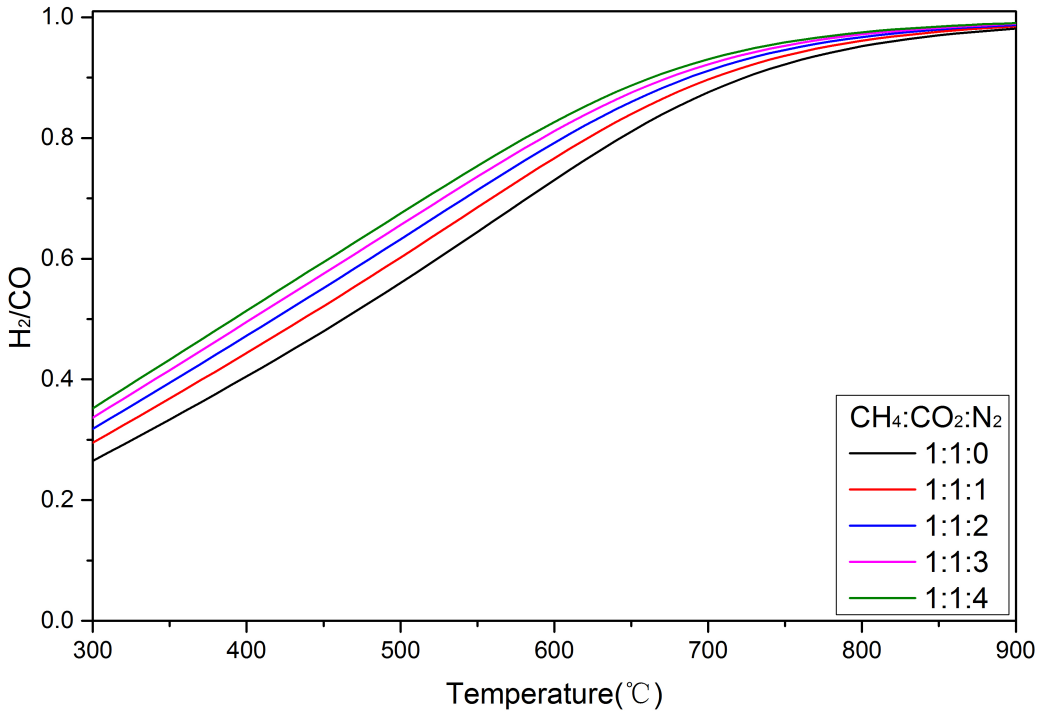

Figure 4.6: Calculated H_2/CO production ratio of the modelled system using Aspen Plus, 300-900℃, overall atmospheric pressure, various dilution of reactants by N_2.

The production of H_2O (as shown in Figure 4.7) can directly display the extent of RWGS. From the information of H_2O selectivity, both increasing the operation temperature and diluting the reactants can effectively diminish the domination of RWGS in the whole reaction system. Moreover, when looking at the yields of H_2O with different dilution of reactants, which directly show the amounts of by-product, each value peaks at a certain operating temperature, and the peak was shift to a lower temperature by increasing the dilution level.

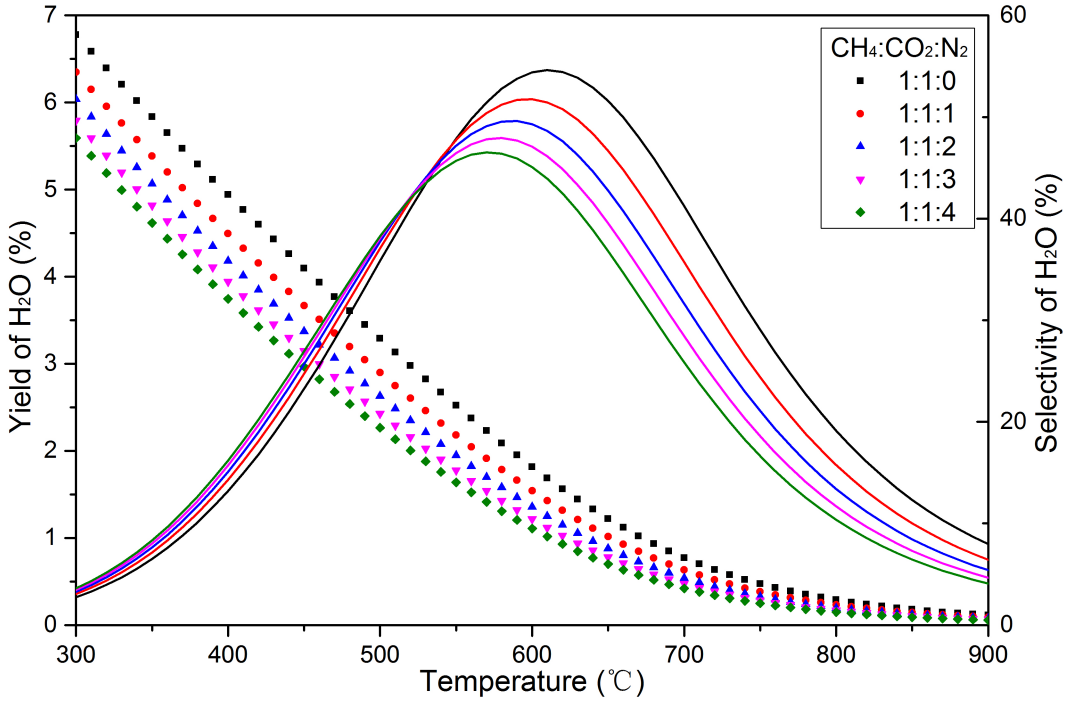

Figure 4.7: Yield of H_2O (solid lines) and selectivity of H_2O (dotted lines) from multi-reaction calculation results with various temperature and different levels of reactant dilution and fixed atmospheric pressure.

4.2 Dehydrogenation of Propane by CO_2 (DHP by CO_2)

In this work, propane was compared to its C_1 - C_4 homologues when dehydrogenated by CO_2. This work is to identify and develop specific chemical utilisation processes for CO_2 that can potentially be achieved by the application of relatively easily-accessible solar thermal energy and associated thermochemical processes, using so-called "Low and Medium Temperature Thermochemical Processes", typically operating for temperature ranges of 100-250℃ and 250-500℃, respectively [14].

The utilisation of solar thermal energy at these lower temperatures for thermochemical processes than the widely-utilised High Temperature Process regime [15] (T˜1000℃) creates

highly interesting and important challenges for catalysis science. Coupling and optimising the catalyst chemistry of CO_2 chemical reactions in the temperature/energy range of ca 300-500℃ with the engineering challenges of cheap, solar thermal collectors may indeed allow the prospect of accessible, sustainable CO_2 utilisation. These coupled challenges therefore provide a high level of opportunity for modern catalysis science and engineering.

4.2.1 Thermodynamic Advantages of the DHP by CO_2

To carry out the thermodynamic calculations, the method has already been completely described in Chapter 3.1, and the following Table 4.4 exhibits the chemical properties of substances related to the dehydrogenation of C_2 - C_4 alkanes ($C_nH_{2n+2} \rightleftharpoons C_nH_{2n} + H_2$) and decomposition of C_1 - C_4 hydrocarbons ($C_nH_m \rightleftharpoons nC + \frac{m}{2}H_2$).

Table 4.4: Standard thermodynamic properties of chemical substance (at 298.15K): Standard molar enthalpy of formation ($\Delta_f H_m^\theta$) standard molar entropy (S_m^θ) and parameters of molar heat capacity at constant pressure ($C_{p,m}$).

Substance	$\Delta_f H_m^\theta$[8] ($KJmol^{-1}$)	S_m^θ[8] ($JK^{-1}mol^{-1}$)	$C_{p,m}/R = A + BT + CT^2 + DT^3 + ET^4$[9]				
			A(10^0)	B(10^{-3})	C(10^{-5})	D(10^{-8})	E(10^{-11})
H_2	0	130.684	2.883	3.681	-0.772	0.692	-0.213
CO	-110.53	197.67	3.912	-3.913	1.182	-1.302	0.515
CO_2	-393.51	213.74	3.259	1.356	1.502	-2.374	1.056
H_2O	-241.82	188.83	4.395	-4.186	1.405	-1.564	0.632
CH_4	-74.81	186.26	4.568	-8.975	3.631	-3.407	1.091
C_2H_4	52.26	219.56	4.221	-8.782	5.795	-6.729	2.511
C_2H_6	-84.68	229.6	4.178	-4.427	5.660	-6.651	2.487
C_3H_6	20.42	267.05	3.834	3.893	4.688	-6.013	2.283
C_3H_8	-103.85	269.91	3.847	5.131	6.011	-7.893	3.079
1-C_4H_8	-0.13	305.71	4.389	7.984	6.143	-9.197	3.165
cis-2-C_4H_8	-6.99	300.94	3.689	19.184	2.230	-3.426	1.256
trans-2-C_4H_8	-11.17	296.59	5.584	-4.890	9.133	-10.975	4.085
i-C_4H_8	-17.10	295.29	3.231	20.949	2.313	-3.949	1.566
n-C_4H_{10}	-126.15	310.32	5.547	5.536	8.057	-10.571	4.134
i-C_4H_{10}	-134.73	291.82	3.351	17.883	5.477	-8.099	3.243
C(graphite)*	0	5.74	-0.977	9.458	-1.118	0.739	-0.207
*: $C_{p,m}$ parameters were calculated by regressing molar heat capacity data in handbook [10].							

In Figure 4.8 we illustrate the underlying thermodynamic considerations for the chemical utilisation of CO_2, where the Gibbs Free Energy of formation of CO_2 and various related substances are shown for comparison. Any attempt at utilising CO_2 as a chemical reactant must therefore take account of the relative stability (Gibbs Free Energy) of the CO_2 utilisation reaction products, as compared to CO_2 and the other reactant(s) Both contributing terms (ΔH and $T\Delta S$) for the Gibbs Free Energy are not favourable in converting CO_2 to other molecules. The carbon-oxygen chemical bonds are strong and substantial energy is needed for their dissociation and subsequent reduction. Similarly, the entropy term ($T\Delta S$) typically makes little or no contribution to the thermodynamic driving force for any CO_2 utilisation reaction.

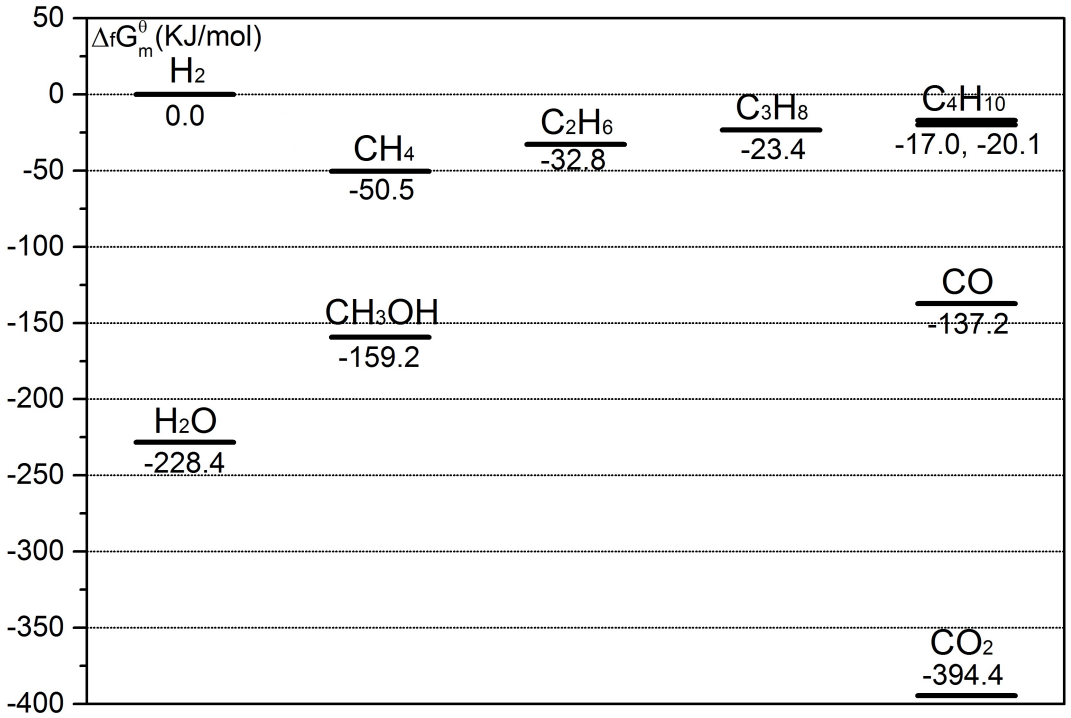

Figure 4.8: $\Delta_f G_m^\theta$ of CO_2 and related substances at normal temperature and pressure (NTP).

The resulting Gibbs Free Energy of the CO_2 chemical utilisation reaction, $\Delta_r G_m^\theta$, pro-

vides information as to the ultimate yield of reaction products at equilibrium, through the relationship $\Delta_r G_m^\theta = -RTln(K^\theta)$.

Figure 4.9 exhibits the standard change of reaction in Gibbs Free Energy ($\Delta_r G_m^\theta$) of the reactions compared. In the temperature range of 300-500℃, all dehydrogenation reactions show a similar trend. The most positive $\Delta_r G_m^\theta$ is found for the process to dehydrogenate C_2H_6 with CO_2 indicating that it is much harder to operate this reaction as compared to other "low-n" alkanes at 300-500℃. Importantly, $\Delta_r G_m^\theta$ does not keep falling as the carbon number of alkane increases, and to dehydrogenate C_3H_8 with CO_2 appears more feasible than some C_4 reactions.

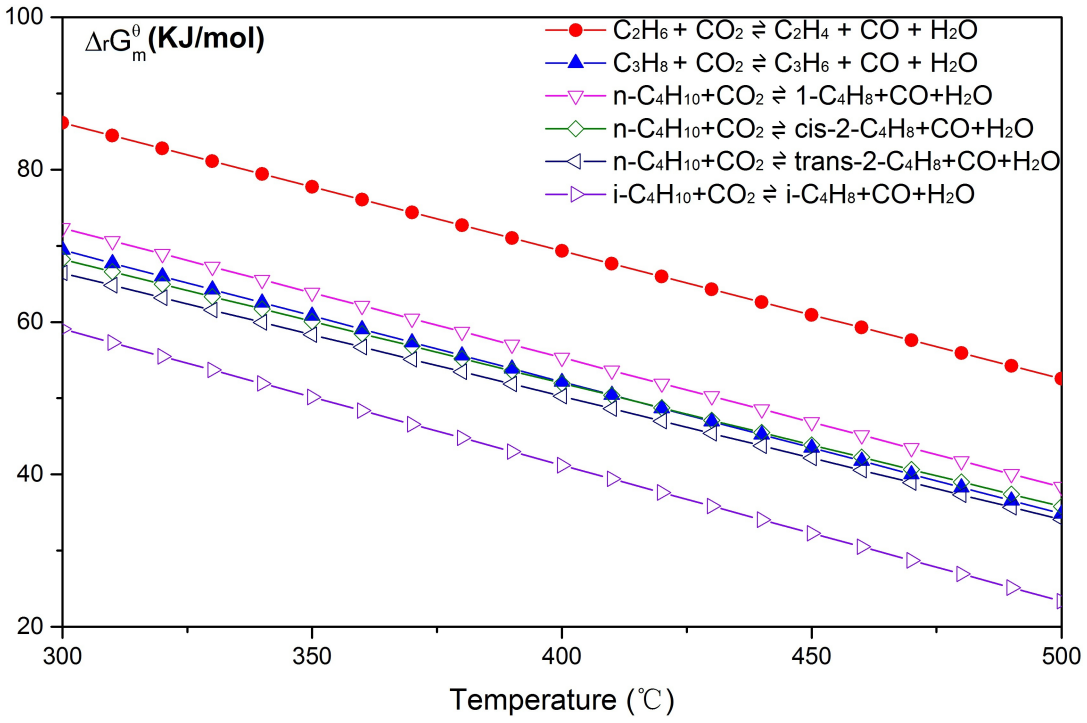

Figure 4.9: $\Delta_r G_m^\theta$ of the dehydrogenation of light alkane in the presence of CO_2 at 300-500℃.

The $\Delta_r G_m^\theta$ of alkanes and olefins cracking to generate carbon and H_2 are shown in Figure 4.10, The C_4 alkanes have multiple curves because of their constituent isomers.

In general, the lower the value of $\Delta_r G_m^\theta$ indicates a higher possibility of cracking for a family of hydrocarbons. Hence, the olefins show much higher cracking possibility than any alkanes, which imply that the selectivity of target products will be greatly affected by further cracking of olefins. For instance, C_3H_6 will be further cracked to lower level hydrocarbons or even carbon, so the selectivity will be reduced. It is also obvious that CH_4 has the highest resistance to coking, and as a sequence of step-wise mechanism of hydrocarbon decomposition, it will be a major by-product in these reaction systems when looking at olefins only, it is obvious that the carbon number is the most important indicator of the cracking possibility. With the similar $\Delta_r G_m^\theta$ of dehydrogenation of alkane with CO_2, C_3H_6 has much higher resistance to cracking than any isomers of butene. Although C_2H_4 has even higher resistance to subsequent cracking, it is even more difficult for C_2H_6 to be activated with CO_2 when the temperature is kept below 500℃. From this analysis, the dehydrogenation of C_3H_8 in the presence of CO_2 is recognisably the best alkane to be targeted for a chemical utilisation process for CO_2 operating in this temperature range - a range specifically chosen for ready-availability of solar heating technology for these conditions.

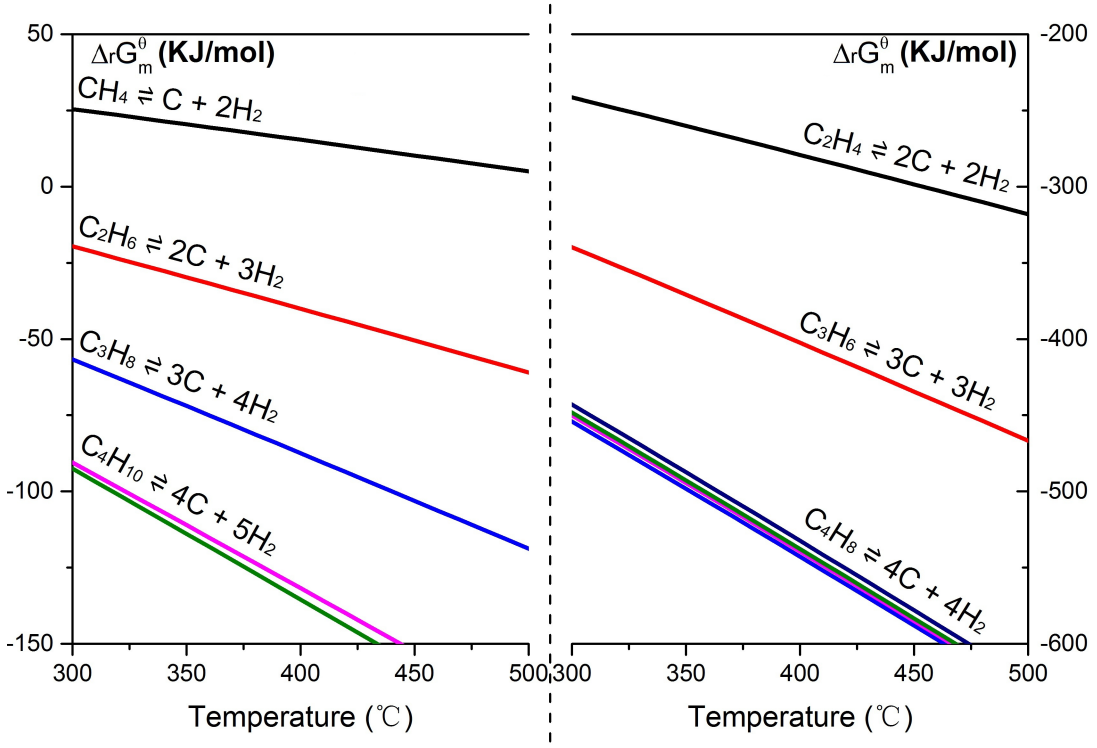

Figure 4.10: $\Delta_r G^{\theta}_m$ of the alkanes (left) and olefins (right) decomposition to generate carbon and H_2 at 300-500℃.

Our research, then, looks in detail at the thermodynamics of the DHP by CO_2 as a potential prospect for CO_2 utilisation in temperature and reaction conditions where the ultimate application of solar thermal energy may be a promising technology. This is a specific example of the broader challenge facing any CO_2 utilisation technology; namely due to the inevitable input energy required to convert CO_2 to useful products, reducing CO_2 emissions through CO_2 utilisation will only be possible if the energy inputs are solely from renewable energy sources. We believe that Low-to Medium Temperature Solar Thermochemical processes offer considerable opportunities in that regard and the research outlined here - setting out the complete thermodynamic analysis together with a catalytic chemistry study - may present a way forward for effective CO_2 utilisation.

4.2.2 Modelled Reaction System of DHP by CO_2

Compared to the DMR, the DHP by CO_2 has a much more complicated system, and lots of side-reactions will massively affect the product distribution. Just like DMR, the DHP by CO_2 can also be separated to two sub-reactions, or from a more accurate way of saying, the DHP by CO_2 is to coupling the traditional DHP (**R.4.6**) and RWGS (**R.4.7**) together. Besides the sub-reactions, cracking of propane to methane and ethylene (**R.4.8**), the decomposition of hydrocarbons ($C_nH_m \rightleftharpoons nC + \frac{m}{2}H_2$) and the Reverse Boudouard reaction (**R.4.10**) were also taken into account. Hence, the reaction system is listed in the following Table 4.5.

Table 4.5: modelled reaction system for the DHP by CO_2.

Reaction Code	Reaction Formula
R.4.6	$C_3H_8 \rightleftharpoons C_3H_6 + H_2$
R.4.7	$H_2 + CO_2 \rightleftharpoons H_2O + CO$
R.4.8	$C_3H_8 \rightleftharpoons C_2H_4 + CH_4$
R.4.9	$C_nH_m \rightleftharpoons nC + \frac{m}{2}H_2$
R.4.10	$C + CO_2 \rightleftharpoons 2CO$

4.2.3 Results of Thermodynamic Calculations

With the standard thermodynamic property data displayed in Table 4.4, the $\Delta_r G_m^\theta$ data of each reaction in Table 4.5 are exhibited as following (Figure 4.11), while the ones of hydrocarbons cracking (**R.4.9**) are already displayed in Figure 4.10. From 300-500℃, only the cracking of C_2 and C_3, including **R.4.8**, can reach to a negative value of $\Delta_r G_m^\theta$, which means these reactions are thermodynamically favoured. On the contrary, the decomposition of CH_4 is not favoured in this temperature range. Considering C_3H_8 is the feedstock in this system and the step-wise mechanism of hydrocarbons to be decomposed, the generation of CH_4 can be an important indicator to measure the degree, and extent of side-reactions during the reaction process. CO_2, as a mild oxidant, is not favoured to gasify the formed

carbon deposition. Hence, CO_2 is always applied in order to shift the equilibrium without increasing the temperature. It is obvious that all other reactions in this system depend strongly on the conversion of C_3H_8 in **R.4.6**. Thus, when considering only **R.4.6**, this is a decomposition reaction which is favoured under lower partial pressure of C_3H_8. With the equilibrium constants calculated from $\Delta_r G_m^\theta$ ($K^\theta = exp[(-\Delta_r G_m^\theta)/RT]$) at the temperature range of 300-500℃, the conversions of C_3H_8 under different partial pressure is calculated as shown in Figure 4.12.

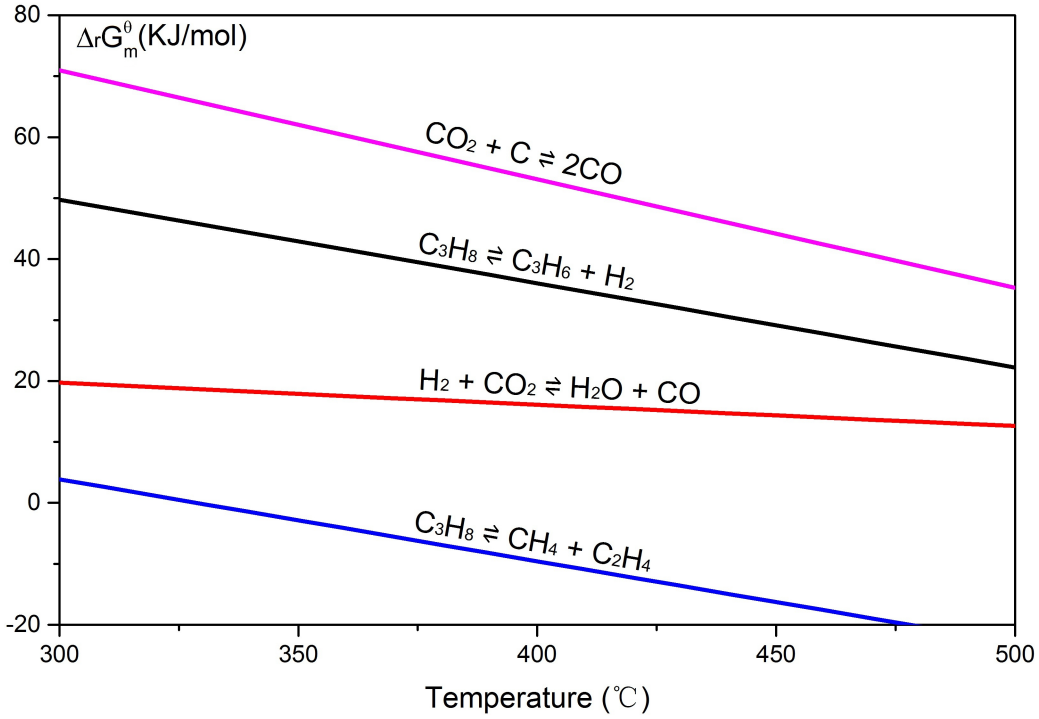

Figure 4.11: $\Delta_r G_m^\theta$ of **R.4.6**, **R.4.7**, **R.4.8** and **R.4.10** in the modelled system of the DHP by CO_2, at 300-500℃.

It is obvious from Figure 4.11 that the $\Delta_r G_m^\theta$ of RWGS reaction decreases much slower than the other 3 reactions as T increases. This is because RWGS is the only one reaction (in Figure 4.11) with the equal numbers of gas molecules at both sides of the reaction

formula. Matters in gas phase are usually much more disordered than liquid and solid state, in another words, the entropy value of gas is much higher than liquid and solid. An increase of gas molecule number at the product side of a reaction can highly increase the overall entropy change of the reaction, and the "slope" , $-\Delta_r S_m^\theta$, becomes more negative.

The C_3H_8 conversion is observed (in Figure 4.12) to be significantly affected by the partial pressure of C_3H_8 within the temperature range of 300-500℃; it is for this reason that the DHP by CO_2 process should be carried out with very low partial pressure of C_3H_8 when designing experiments.

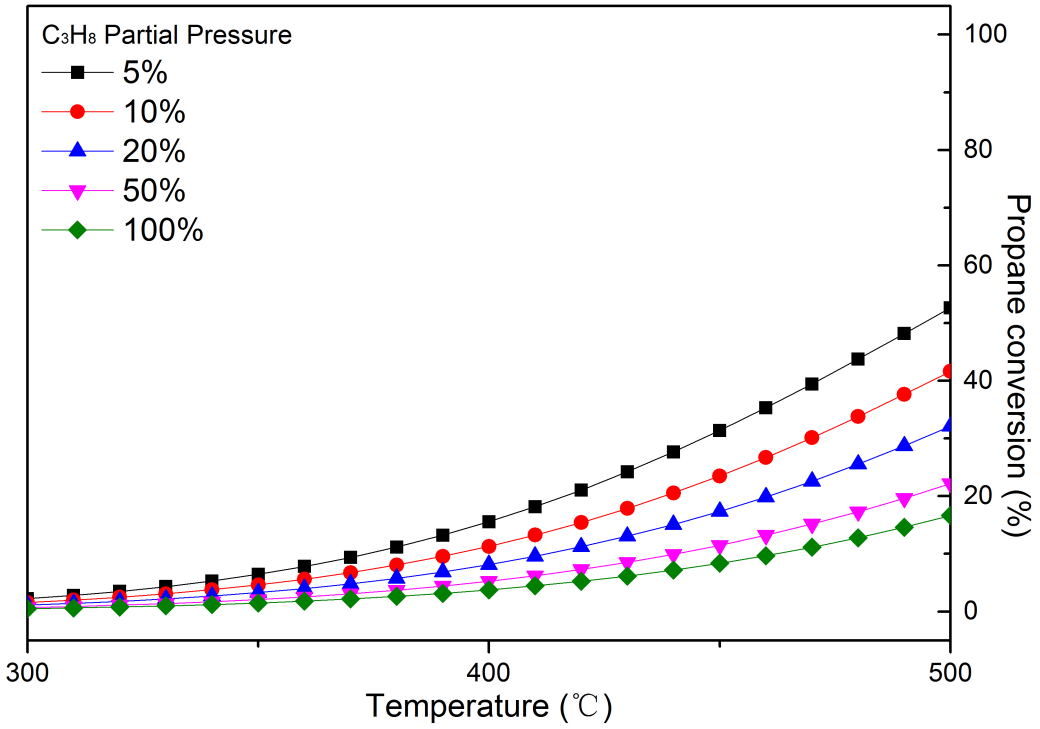

Figure 4.12: Calculated C_3H_8 conversions (mol %) at equilibrium state, considering **R.4.6** only; various C_3H_8 partial pressure; 300-500℃. (Notice: to consider **R.4.6** only means no other by-products and side-reactions are counted.)

Apart from the improvement of catalysts, higher C_3H_6 selectivity can also be achieved by changing the conditions of reaction. A general way to inhibit the reaction extent is to

limit the residence time of reactants on a catalyst surface by increasing the space velocity of gas flow [16]. As a comparison we model this and also increase the partial pressure of reactants operating under these conditions.

4.2.4 Multi-reaction Calculation Results

Multi-reaction calculation results for the DHP by CO_2 process under certain conditions are shown in Figure 4.13. When setting the parameter in Aspen Plus of the input flow, 20ml/min of C_3H_8, 20ml/min of CO_2 and 40ml/min of N_2 was mixed. The overall pressure in the reactor was kept constant at ambient pressure. With a precondition that the system reaches to the equilibrium state regardless the time to achieve this, it was indicated that the consumption of C_3H_8 was a bit more than CO_2at the temperature range of 300℃ below, and this is due to the reverse water gas shift (**R.4.7**) occured. At the temperature range of 300-500℃, both $C_3H_8$and CO_2 are fully converted; meanwhile, a 1:1 ratio of CO:CH_4 production was estimated at the equilibrium state. The element balances of C, H and O between reactants consumption and products generation can be assumed as a reaction formula as $C_3H_8 + CO_2 \rightleftharpoons 2CH_4 + 2CO$ with an overall perspective. Above 500℃, another consumption of CH_4 was observed with the production of C_2H_4 and H_2, and this period can be assumed as $2CH_4 \rightleftharpoons C_2H_4 + 2H_2$ occurred to approach system equilibrium.

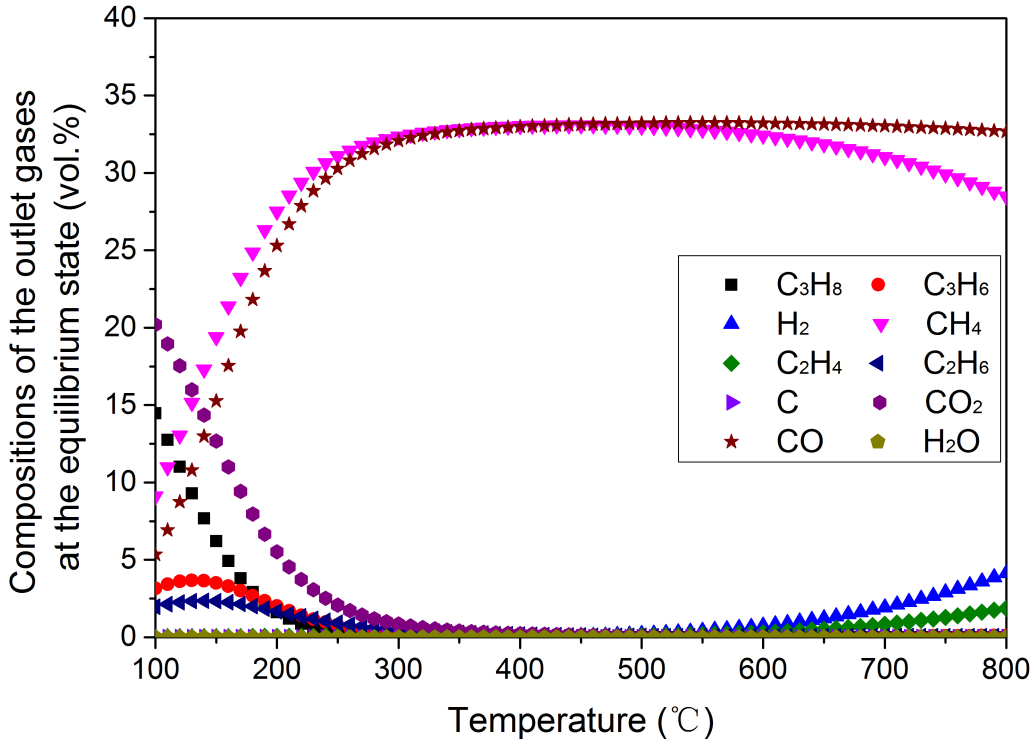

Figure 4.13: Multi-reaction calculation results of the DHP by CO_2 using Aspen Plus (Conditions: 100-800℃, atmospheric pressure, C_3H_8:CO_2:N_2=1:1:2)

Thermodynamically, there seems to be no target product (C_3H_6) produced in the system at equilibrium state, which is totally different from the real world (with catalysts at 500℃) where C_3H_6 can be produced with high selectivity but much lower C_3H_8 conversion in this system. This is mainly attributed to the insufficiently long residence time for substances attached on catalyst surface to be reacted so that the equilibrium state can hardly be achieved. Hence, the core issue for this reaction to achieve higher C_3H_6 selectivity becomes a kinetic one, which means the further cracking effect, which dominates the reaction system as approaching to the equilibrium state, can be inhibited by limiting the adsorption of C_3H_6 over the catalyst surface.

It is also important to notice that both C_3H_8 and CO_2 are reacted even below 100℃

in Figure 4.13, which is impossible in reality. This disagreement indicates that thermodynamic calculations can only suggest the relative potential of a reaction, and the conversions of reactants in the real world are also affected by the kinetic matters. However, it is too arbitrary to judge the value of this Aspen model. This model is in essence to help calculating the thermodynamic equilibrium of a system with multiple reactions involved. The thermodynamic equilibrium, as shown in Figure 4.13, indicates that the reactivity of "olefins cracking" is much more favoured than propane dehydrogenation,which implies the further cracking and low production of propylene during the DHP by CO_2 process in real world.

4.3 Conclusions

4.3.1 For DMR

From the thermodynamic perspective, DMR and SMR were compared through multi-reaction calculations using Aspen Plus software. We have to accept that DMR has a higher energy requirement (according to the enthalpy change). However, from the viewpoint of reactant conversion and by-product mitigation, DMR is calculated to have more potential than SMR at 700℃ or above, and this temperature range, where DMR is more favoured, covers the operation temperature for DMR in industry.

Aiming to increase the conversion of reactants while at the same time inhibiting any side-reactions, dilution of reactants (in order to decrease the feedstock partial pressure), was also introduced as a variable in multi-reaction calculations using Aspen Plus. The results indicated an effective diminishment of H_2O production by increasing the dilution level of reactants, which means with the inhibition of H_2O production as a precondition, the operating temperature can be slightly decreased when the reactants are diluted by non-reacting ingredients such as N_2.

With the conclusions above, we can foresee that the dilution of reactants, by a cycled

N_2 supply, will push the DMR reaction closer to industrialisation, and this also provides a solid basis for a way to utilise CO_2 more effectively, especially the flue-gas conversion via the tri- methane reforming (TMR) [1].

4.3.2 For DHP by CO_2

With the aim of attempting to correlate (ultimately) the DHP by CO_2 process with the energy source from solar heating technology, thermodynamic calculations were carried out for chemical processes operating in the temperature range 300-500℃. An important outcome is the great potential of C_3H_8 comparing to its lighter and heavier homologues (C_2H_6 and C_4H_{10}, respectively) from both the perspective of CO_2 activation and also coking resistance across this temperature range. The $\Delta_r G_m^\theta$ of each reaction in our thermodynamic modelling of the DHP by CO_2 also indicated that neither the RWGS nor the coke gasification with CO_2 are favoured at 300-500℃.

It is important to notice that thermodynamics analysis cannot give the optimised temperature for a process in the real world - the kinetic study will indicate more information on optimising reaction conditions. However, the as calculated thermodynamic results were still instructive to exhibit the potential of this process at 300-500℃. Besides, the thermodynamic results also showed the much more favoured reactivity of "olefins cracking" than "propane dehydrogenation", which hints that further cracking effect will severely happens during the DHP by CO_2 process in real world.

Hence, we still believe that the results presented here are promising in terms of the underpinning catalyst science for establishing the potential industrialisation of CO_2 utilisation through C_3H_8 dehydrogenation. This type of CO_2 utilisation, operating in the relatively low temperature range of 300-500℃, and easily accessible by solar thermochemical routes, could help shift the focus of CO_2 interest from the disposal of an inconvenient by-product, typified by the process of Carbon Capture and Storage (CCS), towards the production and

use of CO_2 as a commodity chemical in Carbon Capture and Utilisation (CCU). However, one must stress again that any proposed CCU process to be realistic for emission reduction potential can only be beneficial if any necessary energy input is from renewable sources. As noted here, our view is that solar thermal chemical processes for CO_2 utilisation, accessible across these temperature ranges, offer very considerable potential in that important regard.

Bibliography

[1] C. Song. Global Challenges and Strategies for Control, Conversion and Utilization of CO2 for Sustainable Development Involving Energy, Catalysis, Adsorption and Chemical Processing. *Catalysis Today*, 115(1-4):2–32, 2006.

[2] Z. Jiang, T. Xiao, V. L. Kuznetsov, and P. P. Edwards. Turning Carbon Dioxide into Fuel. *Philosophical Transactions of the Royal Society of London A*, 368(1923):3343–3364, 2010.

[3] F. T. Zangeneh, S. Sahebdelfar, and M. T. Ravanchi. Conversion of Carbon Dioxide to Valuable Petrochemicals: An Approach to Clean Development Mechanism. *Journal of Natural Gas Chemistry*, 20(3):219–231, 2011.

[4] S. J. Bennett, D. J. Schroeder, and S. T. McCoy. Towards a Framework for Discussing and Assessing CO2 Utilisation in a Climate Context. *Energy Procedia*, 63:7976–7992, 2014.

[5] C. Ampelli, S. Perathoner, and G. Centi. CO2 Utilization: An Enabling Element to Move to a Resource- and Energy-Efficient Chemical and Fuel Production. *Philosophical Transactions of the Royal Society of London A*, 373(2037):1–35, 2015.

[6] S. Ozkara-Aydinoglu and A. Erhan Aksoylu. A Comparative Study on the Kinetics of Carbon Dioxide Reforming of Methane over Pt-Ni/Al2O3 Catalyst: Effect of Pt/Ni Ratio. *Chemical Engineering Journal*, 215-216:542–549, 2013.

[7] B. Wang, J. Zhu, and Z. Lin. A Theoretical Framework for Multiphysics Modeling of Methane Fueled Solid Oxide Fuel Cell and Analysis of Low Steam Methane Reforming Kinetics. *Applied Energy*, 176:1–11, 2016.

[8] P. W. Atkins and J. de Paula. *Atkins' Physical Chemistry.* Oxford University Press, 7th edition, 2002.

[9] J. Kunesh. *The Properties of Gases and Liquids.* McGraw-Hill, 5th edition, 2002.

[10] W. M. Haynes. *CRC Handbook of Chemistry and Physics on DVD.* CRC Press, 95th edition, 2015.

[11] E. S. Rubin, J. E. Davison, and H. J. Herzog. The Cost of CO2 Capture and Storage. *International Journal of Greenhouse Gas Control*, 40:378–400, 2015.

[12] C. Song and W. Pan. Tri-reforming of Methane: A Novel Concept for Catalytic Production of Industrially Useful Synthesis Gas with Desired H2/CO Ratios. *Catalysis Today*, 98(4):463–484, 2004.

[13] Y. Sun, T. Ritchie, S. S. Hla, S. McEvoy, W. Stein, and J. H. Edwards. Thermodynamic Analysis of Mixed and Dry Reforming of Methane for Solar Thermal Applications. *Journal of Natural Gas Chemistry*, 20(6):568–576, 2011.

[14] P. Phelan, T. Otanicar, R. Taylor, and H. Tyagi. Trends and Opportunities in Direct-Absorption Solar Thermal Collectors. *Journal of Thermal Science and Engineering Applications*, 5(2):021003, 2013.

[15] D. B. Fox, E. H. Lee, and M.-H Rei. Carbon Dioxide as Hydrogen Acceptor in Dehydrogenation of Alkanes. *Industrial and Engineering Chemistry, Product Research and Development*, 11:444–446, 1972.

[16] H. Liu, Z. Zhang, H. Li, and Q. Huang. Intrinsic Kinetics of Oxidative Dehydrogenation of Propane in the Presence of CO2 over Cr/MSU-1 Catalyst. *Journal of Natural Gas Chemistry*, 20(3):311–317, 2011.

Chapter 5

Dry Methane Reforming (DMR) over ZrO_2-Supported Metal Carbide Catalysts

The work presented in Chapter 5 is mainly based on the research published in *Applied Petrochemical Research*[1].

5.1 Introduction

The DMR reaction ($CO_2 + CH_4 \rightarrow 2CO + 2H_2$, $\Delta H^{\theta}_{298} = +247 KJmol^{-1}$) is an effective method to utilise CO_2, via a reaction with CH_4 to produce a mixture of CO and H_2 which is called "synthesis gas (syn-gas) [2]" This reaction is, however, highly endothermic and generally high temperatures are required to reduce side-reactions. The DMR process provides several advantages over Steam Methane Reforming (SMR, $H_2O+CH_4 \rightarrow CO+3H_2$, $\Delta H^{\theta}_{298} = +206 KJmol^{-1}$), and perhaps the most important one is the production of syn-gas with a low H_2/CO ratio, which is suitable for use in forming the higher level alcohols [3].

(In a stoichiometric reaction, the H_2/CO ratio of DMR production is 1:1 while SMR has a product ratio of 3:1.) Additionally, of course, DMR does not require the use of water to produce syn-gas.

Metal carbide is a relatively new family member of catalysts for DMR. York and co-workers [4] studied DMR reactions over β-Mo_2C and WC with a direct comparison with noble metal catalysts. The results showed that β-Mo_2C has an activity for DMR comparable to certain noble metals, while the price of molybdenum is much cheaper than noble metals. Furthermore, compared to Ni based catalysts, (arguably the earliest-found material to have a high activity in DMR), Mo_2C has higher stability due to its enhanced resistance to coking. However, the shortcoming of Mo_2C is that the catalyst can hardly be regenerated in-situ if it is oxidised by CO_2 during the reaction, and probably the introduction of bi-metallic carbide catalysts to enhance the Mo_2C lattice is the solution to this problem.

In recent years, supported transition metal carbide catalysts have gained increased prominence since the support can improve both the efficiency and the stability of carbide in the DMR reaction. Systematic studies on Mo_2C loaded on different supports have been carried out by Brungs et al. [5] and Darujati et al. [6]. Their results revealed that during a long-term DMR test, when Mo_2C is supported by ZrO_2 andγ-Al_2O_3, the activity and stability was higher than the materials loaded on other oxide based supports. The advantage of γ-Al_2O_3 appears to be its significantly higher surface area compared to other kinds of support. But the advantage of ZrO_2 is its amphoteric nature [7]. The Lewis acid sites enhance the dispersion of catalysts due to the preference of metal ions to reside at Lewis acid sites on the support [8]; while the Lewis base sites can enhance the adsorption of CO_2 on the support in conjunction with Lewis acid sites [9]. Moreover, on ZrO_2, CO_2 activation takes place at the interface between carbide and support, which leads to a low oxidation effect on carbides [10].

Hence, in seeking catalysts with high activities (including both the conversion of reac-

tants and the yields of products) and high stabilities, here we prepared the ZrO_2-supported Mo_2C and *Co-Mo* carbide catalysts for the DMR. The selection of *Co* is not only because of its high activity in CH_4 decomposition [7] with a relatively high resistance to coking when comparing to the nickel metal [11] but also to enhance the Mo_2C lattice. The *Co-Mo* bi-metallic carbide catalysts have earlier been used for the DMR as an alternative to expensive noble metal [12]; such *Co-Mo* bi-metallic carbide catalysts were systematically prepared and characterised by Xiao and co-workers [13].

5.2 Experimental

5.2.1 Catalyst Preparation

The catalyst support is usually pre-calcined in order to remove moisture and stabilise the oxide, as it would be used at high temperature. Hence, before the wetness impregnation step, the commercial zirconia catalyst support (Alfa-Aesor, 43815) was preheated firstly at 400℃ (marked as -400) which is the same temperature as the slurry calcination process. To make a comparison, this purchased ZrO_2 was also preheated at 750℃ (marked as -750) which is the same temperature as the carburization process.

Stoichiometric ammonium molybdate tetrahydrate (Sigma-Aldrich, A7302) and zirconia support were added to distilled water before stirring to get a slurry. The slurry was stirred and heated at 100℃ to make it as dry as possible before calcination in muffle oven for 10h at 400℃ to which the ramping rate was set at 10℃/min. After the calcination process, the sample of MoO_3/ZrO_2 is obtained. With the aim of preparing Co-Mo bimetallic carbide samples, stoichiometric ammonium molybdate tetrahydrate (Sigma-Aldrich, A7302) and cobalt(II) nitrate hexahydrate (Sigma-Aldrich, 239267) were dissolved in water with the same method as above and the Co/Mo ratio was kept at 0.4/0.6 which has been proved to have the highest stability in pyridine hydrodenitrogenation reactions.[13]

To obtain the carbide materials, the prepared oxides were carburized in a quartz tube under a gas flow of CH_4/H_2 (8ml/min-32ml/min) for 3h at 750℃ to which the ramping rate was 3℃/min. After carburization, the carbide samples were passivated in static air for 48h. Besides the supported carbide catalysts, the pure ZrO_2 support and the bulk Mo_2C carbide were also prepared from zirconia catalyst support (Alfa-Aesor, 43815) and ammonium molybdate tetrahydrate (Sigma-Aldrich, A7302) respectively via the same method of calcination and carburization processes.

As shown in Table 5.1, the carbide samples were labeled with a percentage of Mo_2C loading in terms of their oxide precursors. To be noticed, the "-750" and "-400" appearing in the catalyst labels indicate the temperature (in ℃) to which ZrO_2 support was preheated before the doping procedure.

Table 5.1: Labeling of the carbide catalyst series and their oxide precursors.

Labeled carbide catalysts	Oxide precursors
6%-Mo-750	6wt%-MoO_3/ZrO_2-750
9%-Mo-400	9wt%-MoO_3/ZrO_2-400
12%-Mo-400	12wt%-MoO_3/ZrO_2-400
12%-Mo-750	12wt%-MoO_3/ZrO_2-750
18%-Mo-400	18wt%-MoO_3/ZrO_2-400
24%-Mo-750	24wt%-MoO_3/ZrO_2-750
10%-Co-Mo-400	10wt%-$Co_{0.4}Mo_{0.6}O_x$-400
15%-Co-Mo-400	15wt%-$Co_{0.4}Mo_{0.6}O_x$-400
20%-Co-Mo-400	20wt%-$Co_{0.4}Mo_{0.6}O_x$-400

5.2.2 Catalyst Activity Test

For catalyst activity and stability tests, samples were examined in a custom-designed micro-reactor (M-R-10A, KUNLUN YONGTAI Company, China) under temperature-programmed reaction conditions. The catalyst bed was heated to 600℃ with a 10℃/min ramping rate and then heated up to 850℃ at 5℃/*min*. The gas products were analysed with an on-line Gas Chromatograph (PerkinElmer, Clarus 580 GC) 40 minutes after the temperature

reached 850℃ (see the explanation in Chapter 3.3.1). The reaction occurred under a calibrated mixed gas flow including 1:1 CH_4/CO_2 and N_2 which is the internal standard. The inlet gas flow was kept at $40ml/min$ so that the Gas Hourly Space Velocity (GHSV) is $4.8 \times 10^3 ml \cdot h^{-1} \cdot g_{cat}^{-1}$. The amount of catalysts was kept at $0.5000 \pm 0.0005g$.

With the online GC measurements for the compositions of outlet gases (X_i^{out}, i = N_2, CH_4, CO_2, H_2 and CO), the reactant conversion (CH_4 and CO_2) and the yields of products (H_2 and CO) can be determined with the following equations:

Reactant conversion (%) = $C_i = 1 - \frac{X_i^{out}.X_{N_2}^{in}}{X_i^{in}.X_{N_2}^{out}}) \times 100$ (i = CH_4 and CO_2)

Fractional flow of gas in products (ml/min) = $F_j^{out} = \frac{X_j^{out}.F_{N_2}}{X_{N_2}^{out}}$ (j = H_2 and CO)

Yield of $H_2(\%) = Y_{CH_4} = \frac{F_{H_2}^{out}}{2 \times F_{CH_4}^{in}} \times 100$

Yield of $CO(\%) = Y_{CO} = \frac{F_{CO}^{out}}{2 \times F_{CO_2}^{in}} \times 100$

The calculated reactant conversion and product yield are generally used in catalytic process. The reactant conversion shows the percentage of reactant to be activated and converted when passing through the reactor, whilst the product yield shows efficiency (in percentage) of target product formation by using a certain amount of reactant. In short, these two kinds of values can be respectively considered as indexes of reactivity and productivity in a process.

5.2.3 Pre- and Post-Characterisation

In this chapter, the pre- and post- reaction catalysts were mainly characterised using X-ray Diffraction (XRD), Laser-Raman spectroscopy, Brunauer, Emmett and Teller analysis (BET) and Thermal Gravimetric Analysis (TGA) in air, and the characterisation method in details are outlined in Chapter 3.4.

5.3 Results and Discussions

5.3.1 Reactions over Mo_2C/ZrO_2 Catalysts

Figure 5.1 shows the XRD patterns of ZrO_2-supported Mo_2C with different loading levels at different pre-heating temperatures. The peaks at 2θ=23.267° , 25.879° and 27.250°, corresponding to the 1-1-0, 1-2-0 and 0-2-1 reflections of MoO_3 (pattern reference code:00-005-0506), are not observable in this figure, and this probably means most of the MoO_3 is carburized during the preparation procedure. It is apparent that Mo_2C is dispersed differently over the surface of two kinds of ZrO_2 supports which are pre-heated at 400℃ and 750℃, respectively. The peak of Mo_2C at 2θ=39.49° can be clearly observed on $6\%-Mo-750$ while the peaks at the same position can hardly be observed on $9\%-Mo-400$ and $12\%-Mo-400$, indicating that Mo_2C has a considerably enhanced dispersion on the 400℃-pre-heated support (this has been shown to have a higher surface area according to Table 5.4.) On the other hand, the sharper peaks observed in XRD patterns of "$750-samples$" show that ZrO_2 is more sintered. According to the average grain size of ZrO_2 calculated via the Scherrer Equation with the FWMH (full width at half maximum) of the -1-1-1 reflection, the catalyst support - ZrO_2 - is sintered from less than 300nm to more than 430nm as the pre-heating temperature rises, and the increase of particle size of catalyst support immediately leads to decreased surface area of catalyst during the pre-heating step.

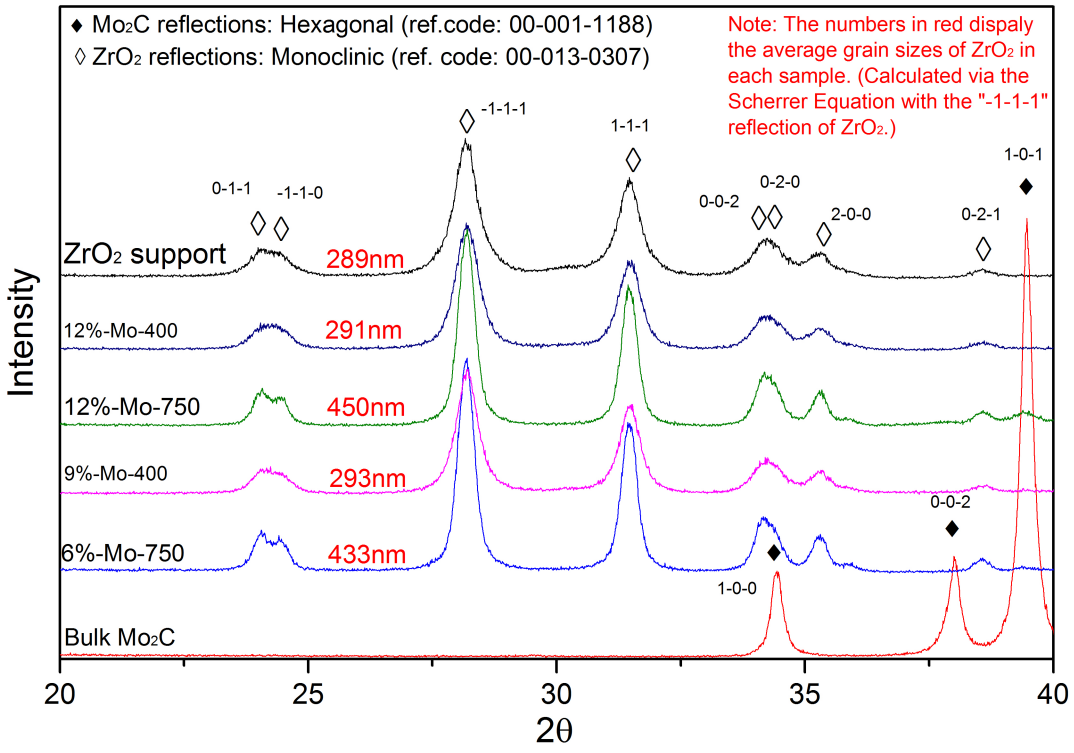

Figure 5.1: X-ray Diffraction patterns of ZrO_2 supported Mo_2C with different loading level (6wt% to 12wt%) and on ZrO_2 supports with different pre-heating temperature (750℃ 400℃, as indicated).

In Figure 5.2, Laser-Raman spectra of the pure ZrO_2, 12%-Mo-400, 18%-Mo-400 and the bulk Mo_2C are presented. The spectrum of ZrO_2 support clearly display the large numbers of monoclinic ZrO_2 assignments which are Zr-O vibrations (380, 349 and 308 cm^{-1}), Zr-Zr vibrations (334, 224 cm^{-1} and so on) and O-O vibrations (105, 382, 476 cm^{-1} and so on), respectively [14]. In the bulk Mo_2C spectrum, the bands observed in fact are due to MoO_3 and correspond to the V_{as} Mo=O stretch (995cm^{-1}), V_{as} Mo-O-Mo stretch (817cm^{-1}), V_s Mo-O-Mo stretch (665cm^{-1}), Mo=O bending (379,335 and 280cm^{-1}), Mo-O-Mo deformation (245, 218,196,150,127 and 114cm^{-1}); [15, 16]. No Mo_2C assignments are observed on Mo_2C catalysts (neither the ZrO_2 supported ones nor the bulk one), which is due to oxidation of Mo_2C by oxygen when exposing the samples in atmosphere. On

12%-Mo-400 and 18%-Mo-400, the bands at 1596 and 1313cm^{-1}, corresponding to the D-band and G-band of carbon, indicate that coke formed on the sample surface during the carburization procedure [16].

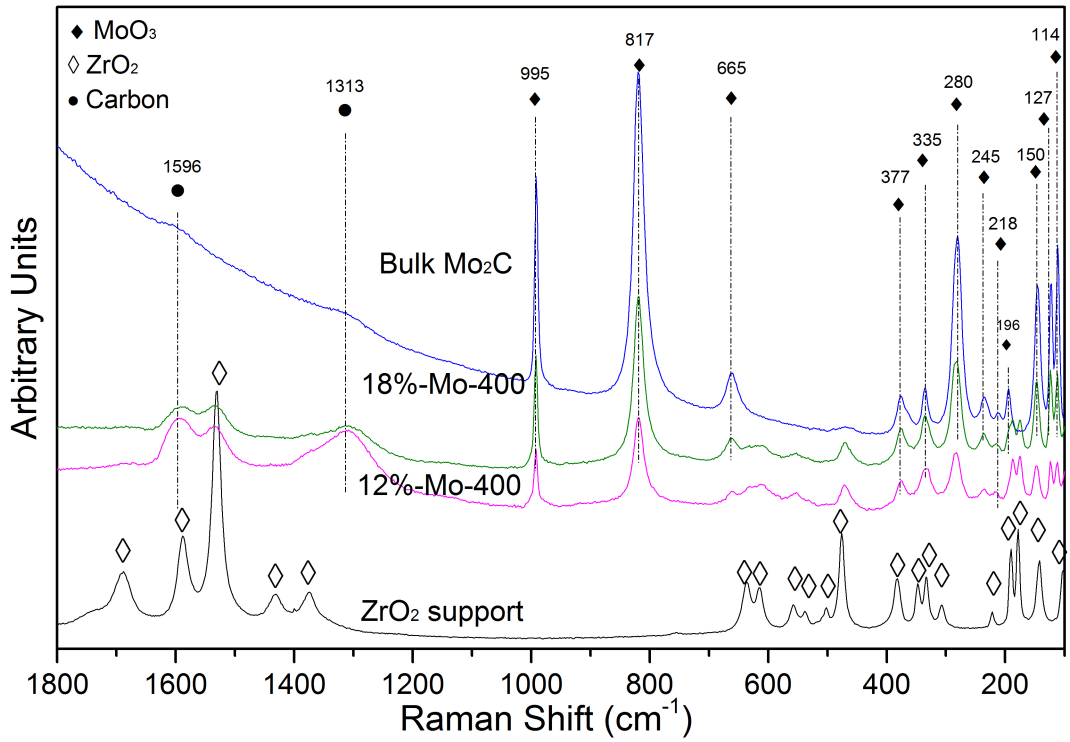

Figure 5.2: Laser-Raman spectra of Mo_2C 6%-24% loaded on 400℃-pre-heated ZrO_2 (Notice: The appearance of MoO_3 in Laser-Raman spectra is because the outer layer Mo_2C was oxidised during the passivation step after carburisation, and the very thin layer of MoO_3 cannot be observed in the XRD patterns in Figure 5.1.)

When discussing the process of the DMR reaction, CH_4 absorption and subsequent dissociation is usually recognised to be the first step as well as the rate determining step (**R.5.1**) [17–20], followed by the oxidation of carbonaceous species (adsorbed carbon and CH_x) on a catalyst surface by CO_2, to form CO (**R.5.2**):

$$CH_4 \rightleftharpoons CH_x + (4-x)H \rightleftharpoons C + 2H_2 \quad \text{....R.5.1}$$

$$CO_2 + C \rightleftharpoons 2CO \quad \text{....R.5.2}$$

Besides the DMR, a side-reaction known as "Reverse Water Gas Shift" (RWGS, **R.5.3**) can lead to a higher conversion of CO_2 and the consumption of generated H_2.

$$H_2 + CO_2 \rightleftharpoons CO + H_2O \quad \text{....R.5.3}$$

Table 5.2 lists the gas compositions and the total flow rates during the DMR reactions over various catalysts. The data were collected at 3 time points: **a,** before the reaction (or saying feedstock); **b,** at 40 minutes of the time on stream (first GC measurement); **c,** at 4 hours of the time on stream. Based on these data, more interpreted results such as reactant conversions and product yields were calculated and shown in Table 5.3.

Table 5.2: Gas compositions (X_i) and the total outlet flow rates during the DMR reactions over different samples (Bulk Mo_2C, Pure ZrO_2 support and ZrO_2 supported Mo_2C catalysts). Conditions: 850℃, Atmospheric pressure, 4-hour duration (the first measurement was taken at 40min after the reaction started), CH_4/CO_2=~1, GHSV=$4.8\times10^3 ml\cdot h^{-1}\cdot g_{cat}^{-1}$). **To be noticed, the error due to the GC measurement is** ±2.0%**.**

Sample	Total Flow (ml/min)			X_{CH_4}(vol.%)			X_{CO_2}(vol.%)		
	Inlet flow	40min	4h	Inlet flow	40min	4h	Inlet flow	40min	4h
Bulk-Mo_2C	43	47	46	33	26	26	35	21	26
ZrO_2-Support	39	43	43	34	24	24	39	25	24
9%-Mo-400	43	49	48	32	16	18	35	13	15
12%-Mo-400	45	50	49	32	17	18	34	13	15
12%-Mo-750	44	48	47	30	17	18	35	13	15
18%-Mo-400	44	49	48	30	16	17	35	14	17
24%-Mo-750	45	49	48	30	18	19	36	15	16
Sample	X_{H_2}(vol.%)			X_{CO}(vol.%)			X_{N_2}(vol.%)		
	Inlet flow	40min	4h	Inlet flow	40min	4h	Inlet flow	40min	4h
Bulk-Mo_2C	0	5	4	0	18	13	31	29	29
ZrO_2-Support	0	6	6	0	17	18	34	31	31
9%-Mo-400	0	16	14	0	27	24	31	27	28
12%-Mo-400	0	17	14	0	26	24	30	27	27
12%-Mo-750	0	16	14	0	27	24	30	28	29
18%-Mo-400	0	16	14	0	26	24	30	27	28
24%-Mo-750	0	17	14	0	26	24	30	28	29

The activity test results presented in Table 5.3 show very poor performance of the

bulk Mo_2C to activate and convert both CH_4 and CO_2 at atmospheric pressure, and the conversions are even lower than the ZrO_2 support which is "carburised" under the same conditions to prepare carbide catalysts. This can be attributed to the low surface area of the bulk Mo_2C, which leads to a low availability of Mo_2C active sites on the surface of the material (which is different from the high-surface-area metal carbide materials prepared by Claridge et al. [21]). The activity in converting both CH_4 and CO_2 over pure ZrO_2 support is attributed to its amphoteric property [7, 22]. Both Lewis acid sites and base sites can enhance the adsorption of CH_4 and CO_2 on ZrO_2 surface [9] where the reactants can be activated and converted. According to the product ratio, significantly more CO was generated than H_2, and this is due to the RWGS (**R.5.3**).

Table 5.3: Conversion of CH_4 and CO_2, Yield of H_2 and CO, and the product ratio over different samples (Bulk Mo_2C, Pure ZrO_2 support and ZrO_2 supported Mo_2C catalysts) during the DMR reactions. Conditions: 850℃, Atmospheric pressure, 4-hour duration (the first measurement was taken at 40min after the reaction started), CH_4/CO_2=~1, GHSV=$4.8 \times 10^3 ml \cdot h^{-1} \cdot g_{cat}^{-1}$). **To be noticed, the error due to the GC measurement is** ±2.0%.

Sample	C_{CH_4}(%)		C_{CO_2}(%)		Y_{H_2}(%)		Y_{CO}(%)		H_2/CO	
	40min	4h	40min	4h	40min	4h	40min	4h	40min	4h
Bulk-Mo_2C	13	15	37	21	7	6	28	19	0.26	0.29
ZrO_2-Support	19	23	31	33	9	9	24	25	0.35	0.35
9%-Mo-400	42	38	57	52	29	25	44	39	0.65	0.61
12%-Mo-400	41	37	56	52	27	23	41	39	0.63	0.57
12%-Mo-750	41	36	55	48	31	24	44	39	0.66	0.59
18%-Mo-400	40	37	55	51	28	23	41	38	0.63	0.58
24%-Mo-750	31	28	47	43	27	23	42	39	0.60	0.55

Importantly, higher activities and stabilities were observed over supported Mo_2C compared to the bulk Mo_2C. The support effect caused by ZrO_2 was particularly noticed, which enhanced both reactant's conversions and product yields.

Comparison of the catalysts with the same pre-treated supports (400℃ or 750℃) showed there was a trend that a higher Mo_2C loading level it led to a lower conversion of CH_4 and CO_2. This may be due to the high loading levels of Mo_2C which led to a poor dispersion

on the ZrO_2 surface by crystalising into a 3D Mo_2C phase.

The results of the surface area and pore volume of samples both prior to ("Pre-") and post-reaction ("Post-") are presented in Table 5.4. A noticeable difference between the surface areas of the two samples pre-reaction was observed, indicating a more highly sintered ZrO_2 support after being heated at 750℃.

Moreover, the difference between the post-reaction surface areas of the two samples is much smaller, which is caused by a further sintering effect when the catalyst was heated up to 850℃ during the reaction, and this sintering effect was possibly one of the main routes of deactivation during the DMR.

Table 5.4: Surface area and pore volume of samples (ZrO_2 supported Mo_2C catalysts) pre- and post- reactions.

Sample name	Surface area ($m^2 \cdot g^{-1}$)		Pore volume ($cm^3 \cdot g^{-1}$)	
	Pre−	*Post−*	*Pre−*	*Post−*
9%-Mo-400	55.8	35.5	0.26	0.23
12%-Mo-750	29.8	24.4	0.22	0.16

Comparison of the XRD patterns of the supported carbide catalysts pre- and post-reaction are presented in Figure 5.3. They showed that MoO_2 peaks at 2θ=26.11° and 2θ=37.12° were observed in the post-reaction catalysts. This phenomenon indicates the oxidation of Mo_2C to MoO_2 with CO_2 (**R.5.4**), which is known to be another main deactivation mechanism of DMR.

$$Mo_2C + 5CO_2 \rightarrow 2MoO_2 + 6CO \quad ....\mathbf{R.5.4}$$

A new peak corresponding to the Mo_2C 1-0-1 reflection at 2θ=39.49° is observed. From the XRD patterns in Figure 5.1, we know that most MoO_3 on ZrO_2 surface is successfully carburized during the preparation, and the disappearance of the Mo_2C peaks over 9%-Mo-400 and 12%-Mo-400 is just due to the high level dispersion of Mo_2C on the surface. Hence,

here Figure 5.3 also indicates that Mo_2C crystallised when the surface area of the ZrO_2 support decreased during the 4-hour activity test (shown in Table 5.4).

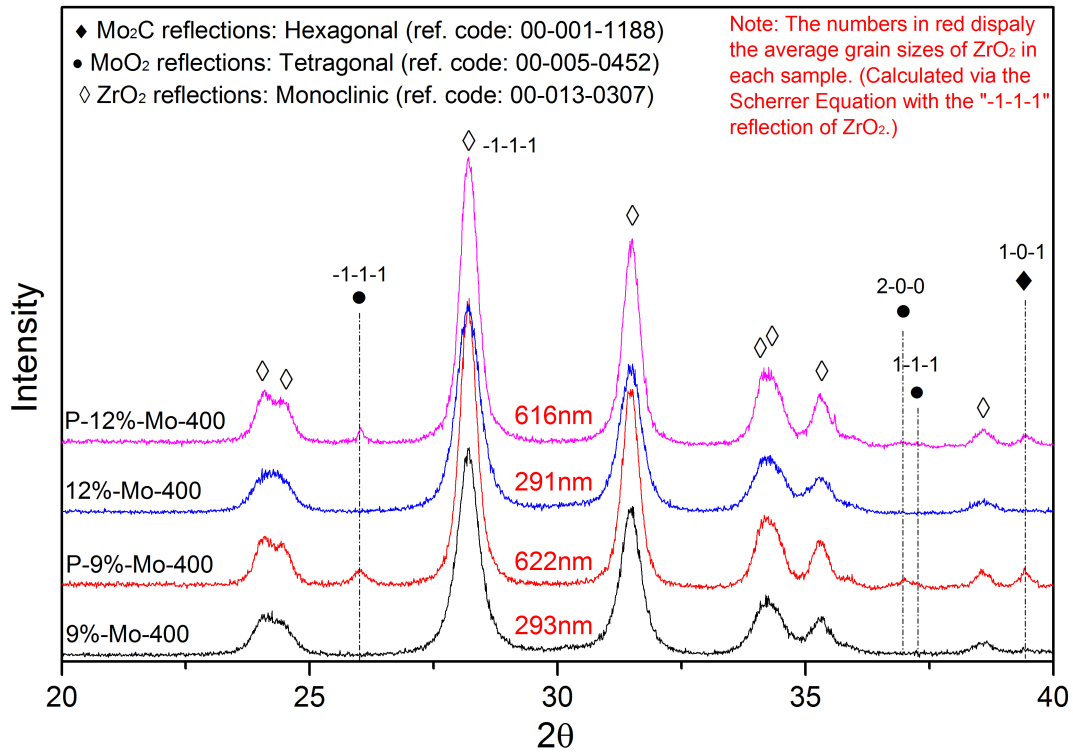

Figure 5.3: X-ray Diffraction patterns of the ZrO_2 supported Mo_2C catalysts before and after DMR (P: post-reaction).

In order to elucidate whether the catalysts experienced carbon deposition over the catalyst surface during the DMR, TGA was carried out for the spent catalyst samples. Results for the pre- and post- reaction 18% catalysts are displayed in Figure 5.4. The weight increased between 200-460℃, which indicated the oxidation of Mo_2C to MoO_3. Weight loss was observed starting at 460℃ and 800℃ and related to the combustion of amorphous carbon [23] and the sublimation of MoO_3 [24], respectively. The graphitic carbon which is expected to be combusted between 600-800℃ [25] can hardly be observed from the TGA curves. Upon comparison of these two TGA curves, more amorphous carbon

was observed on the post-reaction catalyst, which means the generation of carbon via the decomposition of CH_4 (**R.5.1**) occurred on the surface of catalyst during the DMR.

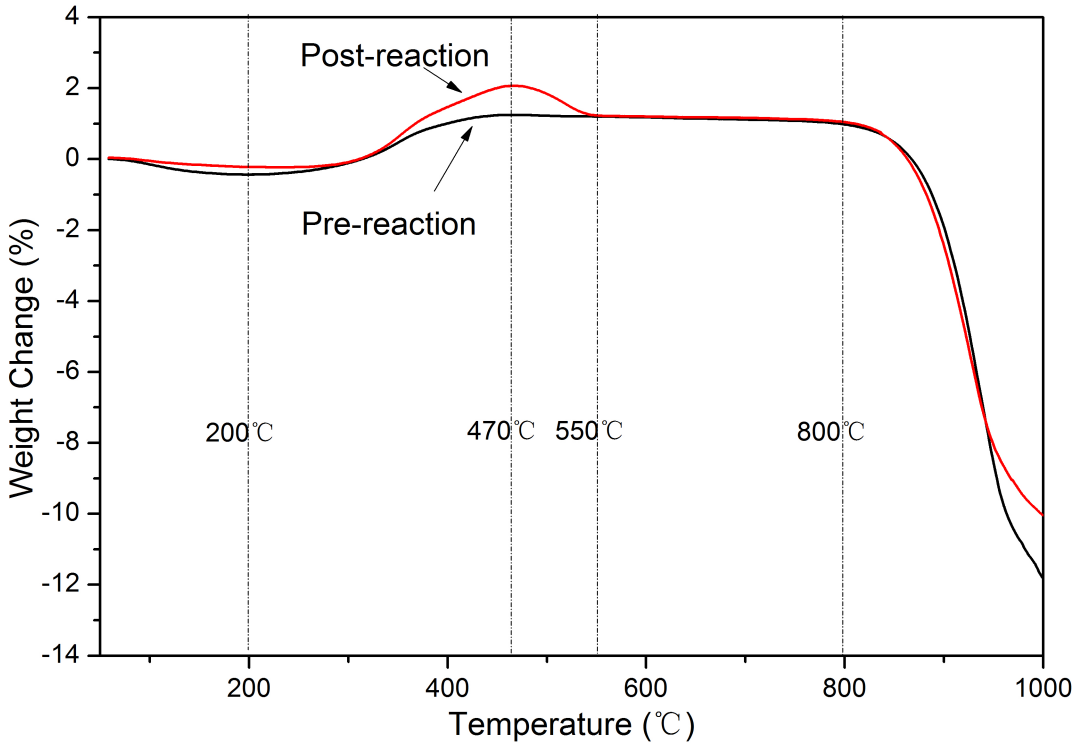

Figure 5.4: TGA results of the pre- and post- reaction 18%-Mo-750 catalysts.

Theoretical and actual weight changes at different temperature ranges are outlined in Table 5.5. The theoretical weight changes are calculated based on stoichiometric loading of Mo_2C and MoO_3 during the catalyst preparation procedures, whilst the actual weight changes are the data directly counted from the TGA curves. The weight gains at 200-470℃ are related to the oxidation of Mo_2C ($Mo_2C + 4O_2 \rightarrow 2MoO_3 + CO_2$), and big differences between the theoretical and the actual values are observed. This phenomenon is attributed to the weight gains at 200-470℃ are overlapped with the following weight losses at 470-550℃ (related to coke combustion in air), and the overlapping means the weight gains and losses are canceling each other in values. Moreover, due to the unknown extent of the Mo_2C

oxidation before the TGA measurement, from both the carbide passivation (see Chapter 3.2.4) and the oxidation effect in DMR (see Figure 5.3), the precise quantification is hardly achieved without more data such as the differential thermal gravimetric curve (D-TGA). Unfortunately, all catalysts mentioned in this chapter were measured for TGA data only, and it was a pity to ignore the data collection of D-TGA from which more information should have been derived.

Table 5.5: List of weight changes on the of the pre- and post- reaction 18%-Mo-750 catalysts. (Including: temperature range, reaction/mechanism corresponded, theoretical weight change and actual weight change.)

Temperature Range	Mechanism	Theoretical Wt. Change		Actual Wt. Change	
		pre-	post-	pre-	post-
200℃ below	Moisture Evaporation	no theoretical amount		-0.5%	-0.5%
200-470℃	Mo_2C Oxidation	5.54%	<5.54% *	1.68%	2.29%
470-550℃	Coke Combustion	no theoretical amount		-0.04%	-0.86%
800℃ above	MoO_3Sublimation	19.00%	< 19.00% *	-13% **	- 11% **
*: The percentages of Mo_2C and MoO_3 are diluted by the coke on post-reaction catalysts.					
**: The weight losses continued as the temperature went above 1000℃.					

5.3.2 Reactions over $Co_{0.4}Mo_{0.6}C_x/ZrO_2$ Catalysts

As an extension of this work based on the results of metal carbide catalysts, bi-metallic carbide catalyst systems were also investigated to enhance the activity and stabilities of catalysts in the DMR. The results can be summarised as follows.

In the XRD patterns after adding cobalt to the catalyst in Figure 5.5, the peaks corresponding to the $CoMoO_4$ structure at 2θ = 23.33°, 25.50° and 26.50° were observed. In addition, the Co_3O_4 phase was not observed. This indicated that only $CoMoO_4$ had been formed during the calcination process. After carburisation, phases of Mo_2C at the angles of 2θ=38.101° and 39.492° were observed clearly and there appeared to be no evidence of Co metal particles or Co carbide in the XRD patterns. According to Xiao et al. [13], this phenomenon is attributed to the direct incorporation of cobalt into the lattice of Mo_2C

carbide, and due to the smaller atomic radius of Co (r≈126pm) compared with that of Mo (r≈154pm), the framework of Mo_2C did not significantly change even though the lattice was partially substituted by Co atoms.

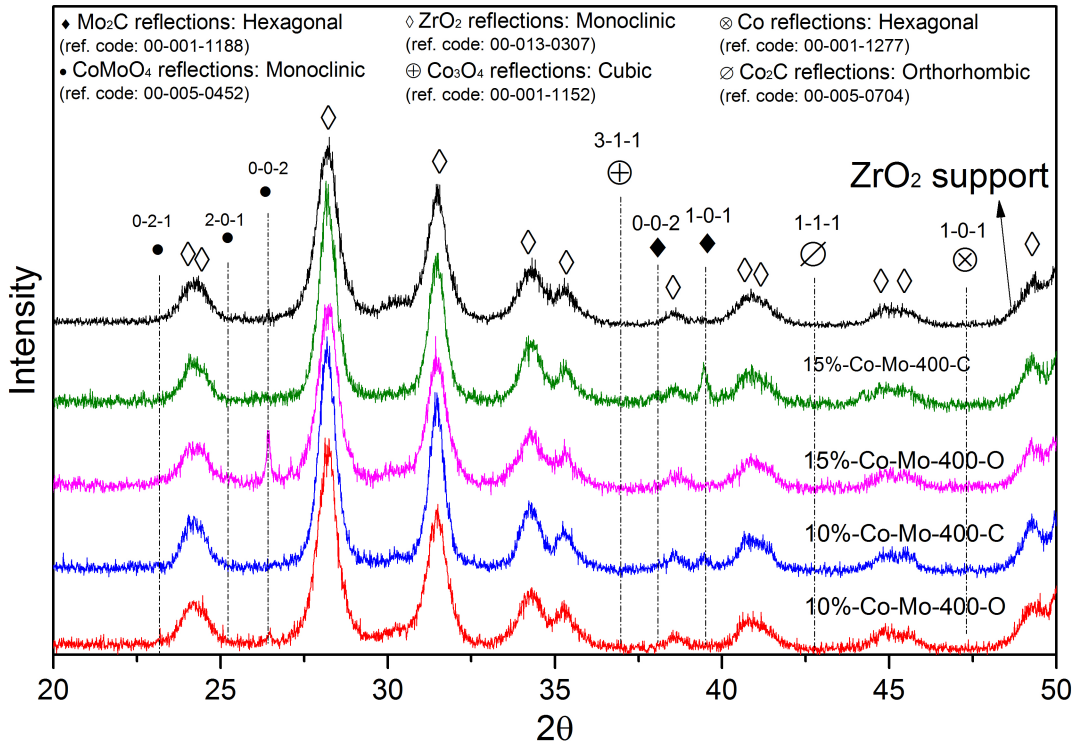

Figure 5.5: XRD patterns of ZrO_2 supported 10%/15% $Co-Mo$ bi-metallic oxides and carbides (C: carbide; O: oxide).

The TGA results of the pre-reaction bi-metallic catalysts are exhibited in Figure 5.6. There are weight gains for all 3 catalysts from 230℃, which are corresponding to the carbide oxidation reactions: $CoMoC_x + (2+x)O_2 \rightarrow CoMoO_4 + xCO_2$ and $Mo_2C + 4O_2 \rightarrow 2MoO_3 + CO_2$. However, the weight gains from 230℃ and the weight losses from 470℃ are overlapped, so it is unable for us to separate these 2 weight changes based on the TGA curves only. Hence,both the weight gains by carbide oxidation and the weight losses by coke combustion can hardly be precisely quantified from this TGA figure.

Still in Figure 5.6, from the weight loss observed starting at 470℃ which is related to the coke combustion, it indicates that the increased loading level of the bi-metallic carbide enhanced the coke formation during the carburisation step preparing catalysts. A much larger amount of coke formed on 20%-Co-Mo-400 was observed, and this may be due to the different dispersion (agglomeration) level of $CoMoC_x$ on the surface of ZrO_2. To be noticed, the weight loss after 800℃, corresponding to MoO_3 sublimation still observable but was much less than that exhibited by the monometallic catalysts (shown in Figure 5.4). This is because the molar ratio of Mo/Co was 6:4 during the catalyst preparation step, and the Co-Mo bimetallic material ($CoMoO_4$) was formed in a Mo/CO ratio at 1:1 as shown in the XRD patterns (Figure 5.5). Hence, there was a small proportion of Mo element left in the form of monometallic materials (Mo_2C or MoO_3).

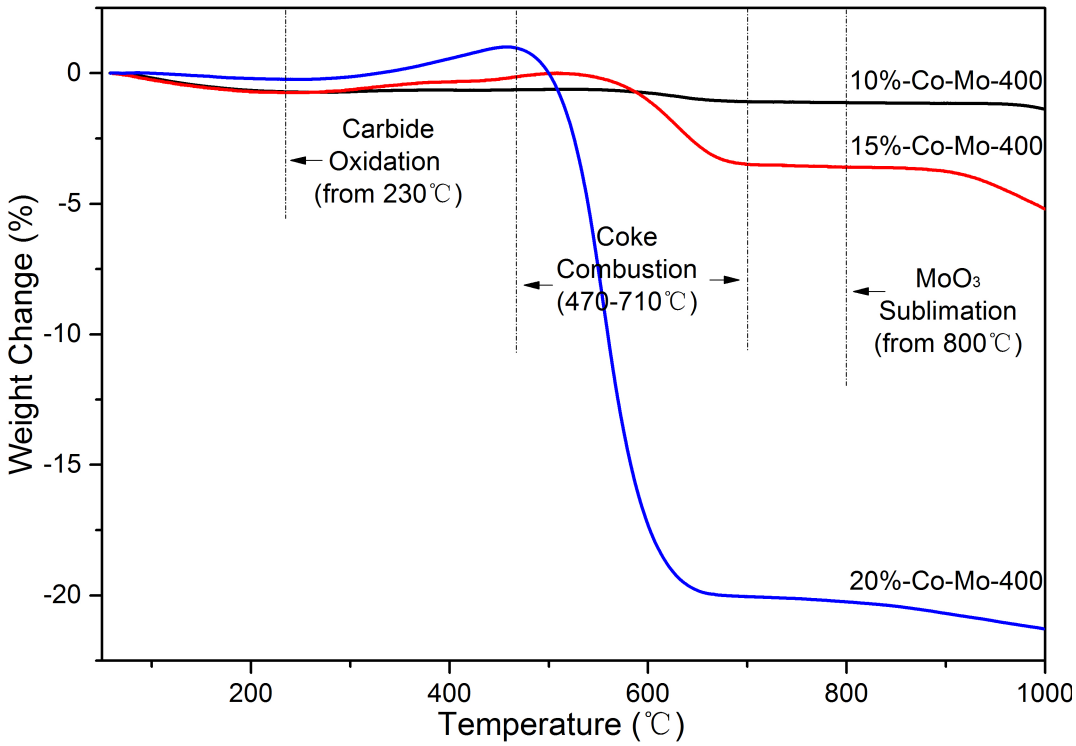

Figure 5.6: TGA results of the pre-reaction $Co-Mo$ bi-metallic catalysts.

The catalyst activity test results over 10%, 15% and 20% bi-metallic carbide catalysts are shown in Table5.6 and Table 5.7. Table 5.6 lists the gas compositions and the total flow rates during the DMR reactions. The data were collected at 3 time points: **a,** before the reaction (or saying the actual inlet flow); **b,** at 40 minutes of the time on stream (first GC measurement); **c,** at 4 hours of the time on stream. Based on these data, more interpreted results such as reactant conversions and product yields were calculated (shown in Table 5.7).

Table 5.6: Gas compositions (X_i) and the total outlet flow rates during the DMR reactions over the bi-metallic carbide samples. Conditions: 850℃, Atmospheric pressure, 4-hour duration (the first measurement was taken at 40min after the reaction started), CH_4/CO_2=~1, GHSV=$4.8 \times 10^3 ml \cdot h^{-1} \cdot g_{cat}^{-1}$). **To be noticed, the error due to the GC measurement is ±2.0%.**

Sample	Total flow (ml/min)			X_{CH_4}(vol.%)			X_{CO_2}(vol.%)		
	Inlet flow	40min	4h	Inlet flow	40min	4h	Inlet flow	40min	4h
10%-Co-Mo-400	40	71	70	33	<1	<1	35	3	3
15%-Co-Mo-400	42	73	72	34	<1	<1	35	<1	<1
20%-Co-Mo-400	41	73	71	35	<1	<1	38	<1	<1
Sample	X_{H_2}(vol.%)			X_{CO}(vol.%)			X_{N_2}(vol.%)		
	Inlet flow	40min	4h	Inlet flow	40min	4h	Inlet flow	40min	4h
10%-Co-Mo-400	0	35	36	0	34	36	33	19	19
15%-Co-Mo-400	0	38	38	0	36	35	32	18	19
20%-Co-Mo-400	0	38	38	0	36	36	33	18	19

With the addition of Co into Mo_2C, there was a significant increase in both CH_4 and CO_2 conversion: The conversion of CH_4 was nearly complete and the conversion of CO_2 also reached above 95% when the loading level of the bi-metallic carbide reached 15% or higher. This very large activity improvement is due to the introduction of Co which has been proven to be very active component in the DMR reaction. In conjunction with the above, the stabilities of both CH_4 and CO_2 conversions were significantly improved with the addition of Co components. In addition, the stabilities of both H_2 and CO yields were enhanced as the loading level increased.

Table 5.7: Conversion of CH_4 and CO_2, Yield of H_2 and CO, and the product ratio over the bi-metallic carbide samples during the DMR reactions. Conditions: 850℃, Atmospheric pressure, 4-hour duration (the first measurement was taken at 40min after the reaction started), CH_4/CO_2=~1, GHSV=$4.8 \times 10^3 ml \cdot h^{-1} \cdot g_{cat}^{-1}$. **To be noticed, the error due to the GC measurement is** ±2.0%.

Sample	C_{CH_4}(%)		C_{CO_2}(%)		Y_{H_2}(%)		Y_{CO}(%)		H_2/CO	
	40min	4h	40min	4h	40min	4h	40min	4h	40min	4h
10%-Co-Mo-400	98	97	87	85	94	88	88	83	1.13	1.13
15%-Co-Mo-400	97	97	98	96	98	95	90	86	1.09	1.10
20%-Co-Mo-400	98	98	98	97	97	95	90	87	1.09	1.09

The H_2/CO product ratio over all the three bi-metallic carbide catalysts (as shown in Table 5.7) were above 1, which indicated the CH_4 decomposition (reaction 1) was favoured over the bi-metallic catalysts. As mentioned in monometallic carbide catalyst discussion, the availability of ZrO_2 gives contributions to the conversions of both CH_4 and CO_2, and on the other hand, it also improves the side-reactions which can lead to the observed difference between the conversions and the product yields. As exhibited in Table 5.7, the conversions of CH_4 and the yields of H_2 were arguably at the same level. This phenomenon indicated that the addition of Co component in the Mo_2C catalysts can highly depress the RWGS (**R.5.3**).

The TGA results of the post-reaction bi-metallic catalysts are exhibited in Figure 5.7. No weight losses are observed on 10%-Co-Mo-400 and 15%-Co-Mo-400, and arguably, there is a reduction of weight loss from 470℃ on 20%-Co-Mo-400. This phenomenon on bi-metallic catalysts indicated the consumption of carbon by CO_2 (**R.5.2**) during the DMR reaction. From the curve of 15%-Co-Mo-400, the temperature range of the weight gain by carbide oxidation is clearly displayed at 230-620℃, which proves the weight gains by carbide oxidation and the weight losses by coke combustion are truly overlapped in Figure 5.6 and Figure 5.7.

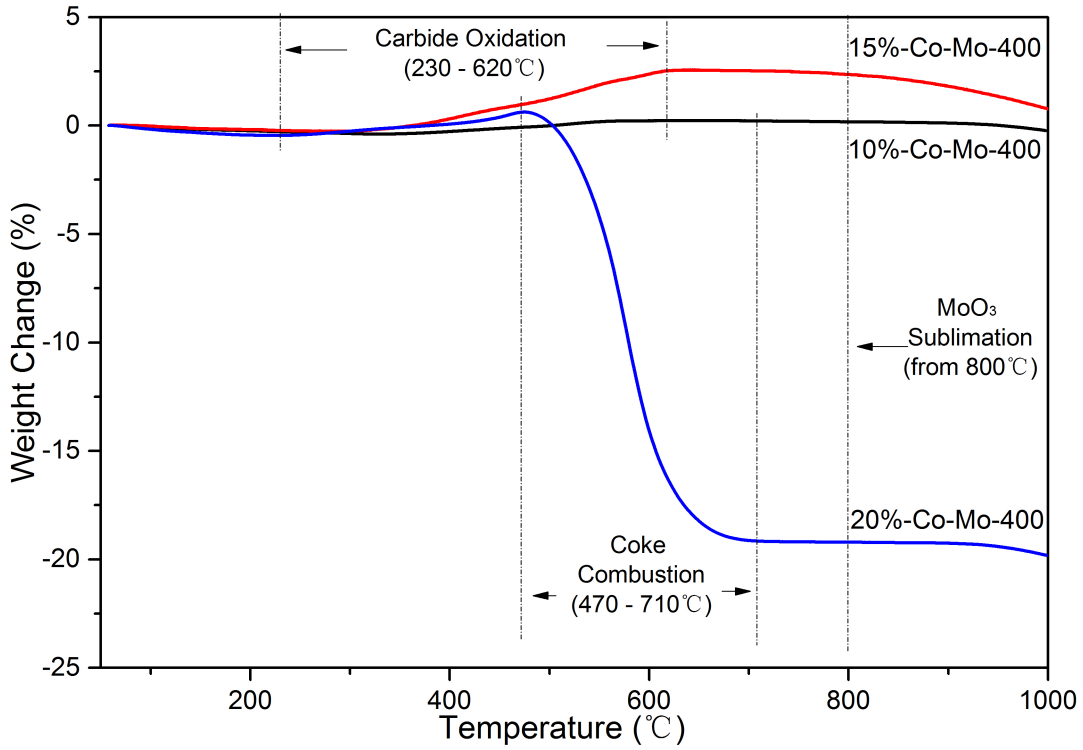

Figure 5.7: TGA results of the post-reaction $Co-Mo$ bi-metallic catalysts.

The very high stabilities of Co-Mo bi-metallic carbide catalysts were also exhibited in their XRD patterns after being tested in the DMR. In Figure 5.8, only the peaks corresponding to $CoMoC_x$ were observed on the ZrO_2 support and there appeared to be no evidence of MoO_2 or $CoMoO_x$ generation. Compared to the formation of MoO_2 over ZrO_2 supported Mo_2C catalysts (shown in Figure 5.3), these catalysts exhibited significantly enhanced oxidation resistance of the bi-metallic carbide phase, this could be explained by the presence of cobalt in the carbide, which may directly enhance the oxidative resistance of the carbide, or provide a re-carburisation route for the oxidised molybdenum.

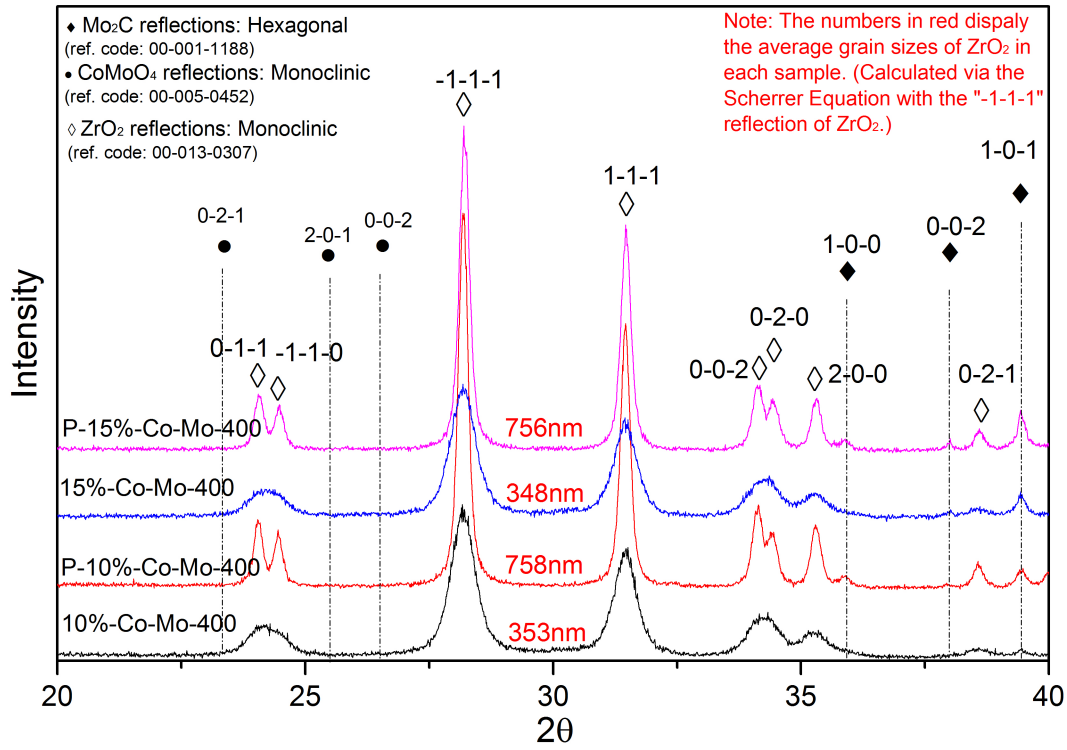

Figure 5.8: XRD patterns of ZrO_2 supported 10%/15% $Co-Mo$ bi-metallic carbide catalysts before and after the DMR. (P-: post-reaction).

5.3.3 Discussions on Catalyst Performances (Conversion, Selectivity and Stability)

When judging the catalyst performance, the conversion of reactant, selectivity of target products and catalyst stabilities are always referred as the most important parameters. Generally speaking, the conversions intuitively show the robust acts of a catalyst (in other words, the reactivity of substances over catalyst surface); the selectivity is indicating how much feedstock can be successfully converted to the target product(s); stability reflects how long the catalyst can perform properly in the real world.

Fortunately, the DMR is a reaction we are aiming to fully open each CH_4 molecule, indicating that the high reactivity and high selectivity can be favoured simultaneously.

This has been proved by comparing the reaction data between mono-metallic and bi-metallic catalysts (the selectivity of target products was enhanced when conversions were massively increased).

Turnover numbers (TON) and turnover frequency (TOF) are often used in evaluating the activity of a catalyst. The TON is more common in homogeneous catalysis and relatively straightforward because moles of catalyst correspond to the amount of organometallic catalyst employed in the test. Hence, TON can be used for the estimation of the longevity of a catalyst system. TOF is quite common in heterogeneous catalysis [26], which expresses the rate at which the catalytic cycle turns over. TON and TOF can be calculated as: $TOF = \frac{converted\ moles\ of\ reactant}{moles\ of\ active\ sites}$; $TOF = \frac{converted\ moles\ of\ reactant}{moles\ of\ active\ sites \times unit\ time}$. Unfortunately, the dispersion of the active phase hasn't been measured so the moles of active sites are unknown. Hence, it would be unreliable to reported the TON/TOF data.

The stability interpreted from reaction data can immediately tell us how quick the catalyst will lose its normal performance and need to be regenerated, and the different levels of deactivation rate will enable us to determine what kind of reactors should be applied in the real world industry. For instance, the catalysts used in the fixed-bed reactors can usually keep their own activity during the time scale of months or years, while for the catalysts with low stabilities, only moving-bed or even fluid-bed reactors can be applied and as a consequence they will cost much more than the fixed-bed reactors. The good news is that the stability of catalytic performance can be greatly enhanced during the time on stream by impregnating cobalt into the Mo_2C catalysts, and the high level performance during a long term is predictable according to the trend in the short term.

Besides the stability of catalytic performance, the stability of a catalyst itself, often related to the deactivation mechanism, is also very important in screening proper catalysts for a specific reaction. A heavy oxidation of Mo_2C can be observed on the mono-metallic post-reaction samples in Figure 5.3, indicating the major deactivation mechanism of catalyst

is the reaction between CO_2 and carbide. Bi-metallic carbide catalyst has shown a high level resistance to the oxidation effect (in Figure 5.8), which is due to structure enhancement of carbide material with the help of cobalt impregnation. There are some hints that can prove this enhancement from the TGA results as shown in Figure 5.4 and Figure 5.7:

1. It is easy to find the MoO_3 sublimation on mono-metallic catalysts according to the massive weight loss after 800℃, while no similar phenomenon can be found on bi-metallic samples;

2. The oxidation of carbide can be observed on TGA curves with a weight increase starting from around 300℃. From mono-metallic carbide data, the mass gains stopped at the temperature before the mass loss which is corresponding to the burning of coke, and this may be implying that the carbon atoms trapped in Mo framework are easier to oxidise than for generated coke. The mechanism is hypothesised that Mo_2C catalyzes the activation of oxygen and its subsequent incorporation into the Mo_2C framework, to produce molybdenum oxicarbide ($MoOC_x$), and this incorporation is probably faster than coke can do. Mo_2C has metallic properties like noble and base metals so it should be able to speed up the dissociation of oxygen even at room temperature and eventually oxidise Mo_2C itself. As a comparison, the oxidation of bi-metallic carbide species extends to the temperature after coke has been completely burned, which is attributed to the more stable carbon atoms in the bi-metallic framework, which is achieved by adding cobalt into the system.

From the industrial application perspective, the anti-oxidation ability of the catalyst is more important than the coke resistance. That is because the carbide material can hardly be regenerated in-situ, which will take massive labour, time and cost to change the catalyst regularly. Compared to this, the coking effect is much less harmful to the industry because of the relatively lower rate of generation with CO_2 as feedstock, and also the possibility to remove the coke in-situ by changing the CO_2 proportion in feedstock. Obviously, there is nothing more important than maintaining the industrial facilities running continuously

and steadily in the long term.

5.4 Conclusions

It was shown that bulk Mo_2C did not exhibit a significantly high activity in the DMR under atmospheric pressure; this was caused by the very low surface area when using the preparation method as described. On the other hand, when ZrO_2 was calcined and carburised with the same method to give ZrO_2 supported Mo_2C catalyst; this exhibited a higher activity compared to the bulk Mo_2C. It appeared that Lewis acid and base sites on the support ZrO_2 had contributed to this enhanced activity.

The catalytic activity decreased slightly with time on stream for the supported Mo_2C over a period of 4 hours. It was thought that this deactivation was caused by two effects: one was the oxidation effect on Mo_2C by CO_2, and the other one was the loss of surface area caused by sintering of the ZrO_2 support.

ZrO_2-supported Co-Mo bi-metallic carbide catalysts were also prepared and examined for catalytic performance for the DMR reaction. Significantly enhancements were observed for both the activities and the stabilities of the catalysts in the DMR reaction. Besides, it was observed that the incorporation of cobalt ions in the supported carbide catalysts significantly improved the materials' resistance to oxidation. Compared to the mono-metallic carbide, the bi-metallic catalysts clearly have significantly higher CH_4 conversion. Moreover, an increase of Co loading in the mixed carbide also reduced the influence of RWGS, which improved H_2 yields.

Bibliography

[1] X. Du, L. J. France, V. L. Kuznetsov, T. Xiao, P. P. Edwards, H. AlMegren, and A. Bagabas. Dry Reforming of Methane Over ZrO2-Supported Co-Mo Carbide Catalyst. *Applied Petrochemical Research*, 4(1):137–144, 2014.

[2] A. T. Ashcroft, A. K. Cheetham, and M. L. H Green. Partial Oxidation of Methane to Synthesis Gas Using Carbon Dioxide. *Nature*, 352:225–226, 1991.

[3] P. Courty, D. Durand, E. Freund, and A. Sugier. C1-C6 Alcohols from Synthesis Gas on Copper-Cobalt Catalysts. *Journal of Molecular Catalysis*, 17(2-3):241–254, 1982.

[4] A. P. E. York, J. B. Claridge, A. J. Brungs, S. Tsang, and M. L. H. Green. Molybdenum and Tungsten Carbides as Catalysts for the Conversion of Methane to Synthesis Gas Using Stoichiometric Feedstocks. *Chemical Communications*, (1):39–40, 1997.

[5] A. J. Brungs, A. P. E. York, J. B. Claridge, C. Marquez-Alvarez, and M. L. H. Green. Dry Reforming of Methane to Synthesis Gas over Supported Molybdenum Carbide Catalysts. *Catalysis Letters*, 70:117–122, 2000.

[6] A. R. S. Darujati and W. J. Thomson. Stability of Supported and Promoted-Molybdenum Carbide Catalysts in Dry-Methane Reforming. *Applied Catalysis A: General*, 296(2):139–147, 2005.

[7] A. W. Budiman, S.-H. Song, T.-S. Chang, C.-H. Shin, and M.-J. Choi. Dry Reforming of Methane Over Cobalt Catalysts: A Literature Review of Catalyst Development.

Catalysis Surveys from Asia, 16(4):183–197, 2012.

[8] M. Masai, H. Kado, A. Miyake, S. Nishiyama, and S. Tsuruya. Methane Reforming by Carbon Dioxide and Steam Over Supported Pd, Pt, and Rh Catalysts. *Studies in Surface Science and Catalysis*, 36:67–71, 1988.

[9] K. Bhattacharyya, A. Danon, B. K. Vijayan, K.A. Gray, P. C. Stair, and E. Weitz. Role of the Surface Lewis Acid and Base Sites in the Adsorption of CO2 on Titania Nanotubes and Platinized Titania Nanotubes: An In Situ FT-IR Study. *Journal of Physical Chemistry C*, 117(24):12661–12678, 2013.

[10] S. Naito, M. Tsuji, and T. Miyao. Mechanistic Difference of the CO2 Reforming of CH4 over Unsupported and Zirconia Supported Molybdenum Carbide Catalysts. *Catalysis Today*, 77(3):161–165, 2002.

[11] I. Luisetto, S. Tuti, and E. Di Bartolomeo. Co and Ni Supported on CeO2 as Selective Bimetallic Catalyst for Dry Reforming of Methane. *International Journal of Hydrogen Energy*, 37(21):15992–15999, 2012.

[12] H. Shao, E. L. Kugler, W. Ma, and D. B. Dadyburjor. Effect of Temperature on Structure and Performance of In-House Cobalt-Tungsten Carbide Catalyst for Dry Reforming of Methane. *Industrial & Engineering Chemistry Research*, 44(14):4914–4921, 2005.

[13] T. Xiao, A. P. E. York, H. Al-Megren, C. V. Williams, H. Wang, and M. L. H. Green. Preparation and Characterisation of Bimetallic Cobalt and Molybdenum Carbides. *Journal of Catalysis*, 202(1):100–109, 2001.

[14] B. Kim and H. Hamaguchi. Mode Assignments of the Raman Spectrum of Monoclinic Zirconia by Isotopic Exchange Technique. *Physica Status Solidi (B)*, 203(2):557–563, 1997.

[15] G. Mestl and T. K. K. Srinivasan. *Raman Spectroscopy of Monolayer-Type Catalysts: Supported Molybdenum Oxides*, volume 40. 1998.

[16] T. Mo, J. Xu, Y. Yang, and Y. Li. Effect of Carburization Protocols on Molybdenum Carbide Synthesis and Study on its Performance in CO Hydrogenation. *Catalysis Today*, 261:101–115, 2016.

[17] O. Takayasu, N. Hongo, and I. Matsuura. *New Aspects of Spillover Effect in Catalysis-For Development of Highly Active Catalysts, Proceedings of the Third International Conference on Spillover(Studies in Surface Science and Catalysis, Volume 77)*. Elsevier, 1993.

[18] A. Erdohelyi. Activation of CH4 and Its Reaction with CO2 over Supported Rh Catalysts. *Journal of Catalysis*, 141(1):287–299, 1993.

[19] V. A. Tsipouriari, Z. Zhang, and X. E. Verykios. Catalytic Partial Oxidation of Methane to Synthesis Gas over Ni-Based Catalysts. *Journal of Catalysis*, 179(1):283–291, 1998.

[20] Z.-F. Yan, R.-G. Ding, L.-H. Song, and L. Qian. Mechanistic Study of Carbon Dioxide Reforming with Methane over Supported Nickel Catalysts. *Energy & Fuels*, 12(10):1114–1120, 1998.

[21] J. B. Claridge, A. P. E. York, A. J. Brungs, C. Marquez-Alvarez, J. Sloan, S. C. Tsang, and M. L. H. Green. New Catalysts for the Conversion of Methane to Synthesis Gas: Molybdenum and Tungsten Carbide. *Journal of Catalysis*, 180(1):85–100, 1998.

[22] B. Xu, B. Zheng, W. Hua, Y. Yue, and Z. Gao. Support effect in Dehydrogenation of Propane in the Presence of CO2 over Supported Gallium Oxide Catalysts. *Journal of Catalysis*, 239:470–477, 2006.

[23] A. H. Fakeeha, W. U. Khan, A. S. Al-Fatesh, and A. E. Abasaeed. Stabilities of Zeolite-Supported Ni Catalysts for Dry Reforming of Methane. *Chinese Journal of Catalysis*, 34(4):764–768, 2013.

[24] S. A. Halawy, M. A. Mohamed, and G. C. Bond. Characterization of Unsupported Molybdenum Oxide Cobalt Oxide Catalysts. *Journal of Chemical Technology and*

Biotechnology, 58(3):237–245, 1993.

[25] D. Bom, R. Andrews, D. Jacques, J. Anthony, B. Chen, M. S. Meier, and J. P. Selegue. Thermogravimetric Analysis of the Oxidation of Multiwalled Carbon Nanotubes: Evidence for the Role of Defect Sites in Carbon Nanotube Chemistry. *Nano Letters*, 2(6):615–619, 2002.

[26] M. Boudart. Turnover Rates in Heterogeneous Catalysis. *Chemical Reviews*, 95:661–666, 1995.

Chapter 6

The Dehydrogenation of Propane by CO_2 (DHP by CO_2) over ZrO_2-Supported Cr-Based Oxide Catalysts

6.1 Introduction

As a raw material for the production of a variety of polymers and chemical intermediates, propylene is well-known to be one of the most important commodities in the petrochemical industry. Currently, propylene is mainly produced as a by-product of ethylene production via naphtha steam-cracking or a fluid catalytic cracking (FCC) of petroleum, which can hardly meet the huge demand for it in the future [1]. Therefore, much effort has been made into discovering a new route to propylene production, and the most popular one is the Dehydrogenation of Propane (DHP, **R.6.1**).

$$C_3H_8 \rightleftharpoons C_3H_6 + H_2 \quad \text{....R.6.1}$$

As an "improved" the DHP process, DHP by CO_2 (**R.6.2**) has been heavily studied over the last decade [2–6]. In this promising reaction, CO_2 acts as a mild oxidant to combine a simple DHP (**R.6.1**) with a reverse water gas shift (RWGS, **R.6.3**), and hence, the equilibrium of DHP reaction can be shifted to the product side. Moreover, CO_2 can also reduce the coking effect of catalyst by the reverse Boudouard reaction (**R.6.4**). Competitive adsorption among propane, CO_2 and generated water vapour can also explain the relatively lower initial conversion of propane, less coking effect, and higher stabilities of catalysts in a CO_2 atmosphere [7].

$$C_3H_8 + CO_2 \rightleftharpoons C_3H_6 + CO + H_2O \quad \text{....R.6.2}$$

$$H_2 + CO_2 \rightleftharpoons CO + H_2O \quad \text{....R.6.3}$$

$$CO_2 + C \rightleftharpoons 2CO \quad \text{....R.6.4}$$

6.1.1 Supposed Redox Cycle Between $Cr(III)$ and $Cr(VI)$

In pursuit of high efficiency in producing propylene, chromium oxides have been documented as potentially promising catalysts for the DHP by CO_2 process. Shishido et al. [7] studied the role of CO_2 in DHP over Cr-based catalysts and concluded the catalytic mechanism involved a redox cycle between $Cr(III)$ and $Cr(VI)$ regardless of the support. As shown in Figure 6.1, $Cr(VI)$ species provide an oxidative dehydrogenation process which is kinetically more efficient than DHP provided by $Cr(III)$ species, and CO_2 acts as an mild oxidant to regenerate the $Cr(VI)$ species from the $Cr(III)$ species after the oxidative dehydrogenation process, which enhanced the dehydrogenating efficiency of the chromium oxide catalyst.

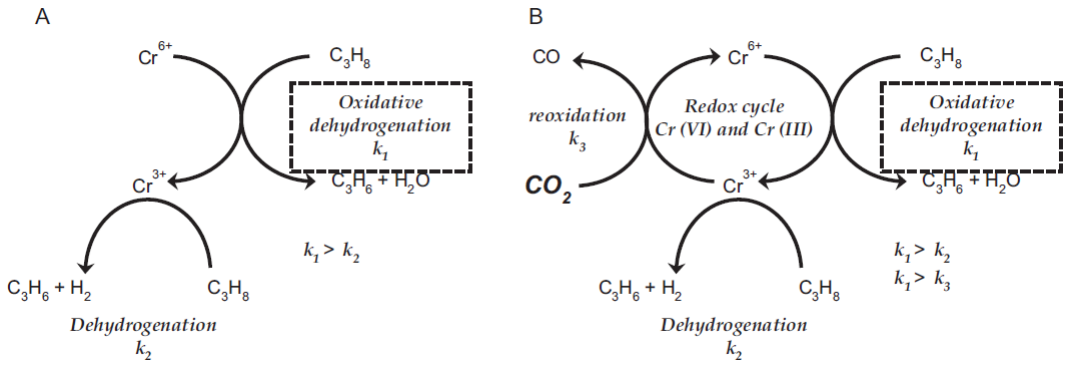

Figure 6.1: Proposed reaction mechanism of dehydrogenation of C_3H_8 in the (A): absence of CO_2 and (B): presence of CO_2 [7].

In fact, this supposed mechanism seems to be not verified by any immediate evidence. So before starting the modification and improvement of Cr-based catalyst, it is necessary to have some quick tests on whether Cr_2O_3 can be oxidised by CO_2 (Section 6.3.1).

6.1.2 The Effect of Support Basicity on Catalytic Performance

Different catalyst supports can also affect the properties of catalysts. Similar phenomena were described by Shishido et al. [7], where the increase of the CO_2 partial pressure made a positive effect on propane conversion over SiO_2 supported catalyst, while negative effects were observed over Al_2O_3 and ZrO_2 supported catalysts. According to the study carried out by Xu et al. [8], this kind of difference is mainly due to the different levels of surface basicity.

In Table 6.1, the CO_2−TPD results (TPD stands for Temperature Programmed Desorption) and propane chemisorption at 300℃ were carried out by Xu et al. [8], demonstrating surface basicity of material and also the real amount of propane adsorbed on catalyst surface respectively. The results clearly showed a rough trend that the adsorption of propane would be more greatly affected by the addition of CO_2 when the surface basicity is relatively higher. It is generally accepted that the competitive adsorption between propane

and other substances (CO_2, H_2O and so on) will highly affect the conversion of propane in reactions [7]. Hence, it is apparent to conclude from this table that the positive effect over SiO_2 supported catalyst results achieved by Shishido et al. [7] is mainly due to the very low surface basicity and no competitive adsorption from CO_2.

Table 6.1: CO_2−TPD results for Ga-based catalysts doped on different kinds of metal oxide support [8].

Metal Oxides	Amount of desorbed CO_2	Propane chemisorption (300℃)($\mu mol/g$)	
	120-600℃($mmol/g$)	in absence of CO_2	in presence of CO_2
Ga_2O_3/TiO_2	0.06	4.2	2.5
Ga_2O_3/Al_2O_3	0.07	5.3	3.7
Ga_2O_3/ZrO_2	0.08	8.1	5.9
Ga_2O_3/SiO_2	0.01	1.1	1.1
Ga_2O_3/MgO	0.18	2.0	1.5

From the perspective of propane conversion, it is likely that higher basicity is harmful to reactions due to the competitive adsorption effect. However, the competitive adsorption effect may also enhance the propylene selectivity in the DHP by CO_2 process through resisting the further adsorption and cracking of propylene on the catalyst surface. Furthermore, from the perspective of CO_2 utilisation, the larger amount of CO_2 may also lead to a higher consumption of itself, and the resultant coke could be oxidised to improve the catalyst stability. Based on these studies, we selected ZrO_2 as our catalyst support. Apart from its relatively higher surface basicity, ZrO_2 is also known for its amphoteric behavior which indicates its high surface acidity as well, and the acidity mainly decides the extent of propane chemisorption on surfaces [9].

To modify the acidity and basicity of ZrO_2−supported catalysts, rare-earth-based promoters are often introduced to slightly enhance the basicity without damaging acid sites. It has been proved that some rare earth oxides have light basicities on their surfaces (usually no more than 200 $\mu mol/g$, quantified by CO_2-TPD) [10, 11], and the adsorption of CO_2 would be improved because the quantification of surface bsicity is usually measured by

CO_2-TPD. Hence, lanthanum, cerium and praseodymium were introduced as promoters in the Cr/ZrO_2 catalyst system. Moreover, sodium and potassium oxides were also introduced as additives to explore how the catalyst performs with very strong surface basicity.

6.2 Experimental

6.2.1 Preparation of Catalysts

In this project we set $5wt\%Cr_2O_3/ZrO_2$(which means 5% in weight of Cr_2O_3 doped on ZrO_2 support) as a reference to the material development by doping additives as promoters.

To prepare the $5wt\%Cr_2O_3/ZrO_2$ catalyst by the wetness impregnation method, ZrO_2 (Alfa-Aesor, 43815) was pre-heated at 600℃ for 6 hours before being ground and sieved to <125μm in particle size. Then, $Cr(NO_3)_3 \cdot 9H_2O$ precursor (Sigma-Aldrich, 239259) was dissolved into distilled water, and this solution was mixed with the ground ZrO_2 support and stirred at room temperature for 24 hours. To achieve Cr_2O_3/ZrO_2, the as prepared suspensions were dried to obtain a slurry or paste, which were finally calcined at 600℃ for 6 hours in a muffle furnace using a heating ramp of 10℃/min. The solid sample was ground to obtain fine particles <125μm. Stoichiometric amounts of nitrate precursors of rare-earth (La, Ce, Pr) and alkali (Na, K) additives was added to the $Cr(NO_3)_3$ solution before mixing with the ZrO_2 particles. The purchase information for these precursors are listed in the table of Chapter 3.2.1. Table 6.2 lists the designed catalysts (may shift the doping level of additives) and the precursors of added promoting oxides.

Table 6.2: The Designated Catalyst System and their Precursors

Catalyst	Code	Precursors
$xwt\%Cr_2O_3/ZrO_2$	xCr/Zr	$Cr(NO_3)_3 \cdot 9H_2O$; ZrO_2
$xwt\%La_2O_3 - ywt\%Cr_2O_3/ZrO_2$	xLa-yCr/Zr	$La(NO_3)_3 \cdot 6H_2O$; $Cr(NO_3)_3 \cdot 9H_2O$; ZrO_2
$xwt\%CeO_2 - ywt\%Cr_2O_3/ZrO_2$	xCe-yCr/Zr	$Ce(NO_3)_3 \cdot 6H_2O$; $Cr(NO_3)_3 \cdot 9H_2O$; ZrO_2
$xwt\%Pr_2O_3 - ywt\%Cr_2O_3/ZrO_2$	xPr-yCr/Zr	$Pr(NO_3)_3 \cdot 6H_2O$; $Cr(NO_3)_3 \cdot 9H_2O$; ZrO_2
$xwt\%Na_2O - ywt\%Cr_2O_3/ZrO_2$	xNa-yCr/Zr	$NaHCO_3$; $Cr(NO_3)_3 \cdot 9H_2O$; ZrO_2
$xwt\%K_2O - ywt\%Cr_2O_3/ZrO_2$	xK-yCr/Zr	KNO_3; $Cr(NO_3)_3 \cdot 9H_2O$; ZrO_2

6.2.2 Catalytic Activity Tests in Micro-Reactor

The stability test of the DHP by CO_2 process was operated in an M-R-10A micro-reactor (KUNLUN YONGTAI Company, China) over the Cr-based catalyst prepared as above. All tests were operated under atmospheric pressure and 500℃ for 5 hours. The first measurement was take at 60 minutes after the beginning of a time-on-stream reaction for outlet flow stabilisation (see the explanation in Chapter 3.3.1). The mole ratio of feedstock (the inlet flow) was kept at $C_3H_8 : CO_2 : N_2 = 5\% : 10\% : 85\%$.

The compositions of outlet gases (X_i^{out}, i = N_2, CH_4, CO_2, H_2 and CO) were analysed using an online Gas Chromatograph (PerkinElmer, Clarus 580 GC). The reactant conversion (C_3H_8 and CO_2), the product yield ($H_2, CO, CO_2, CH_4, C_2H_4, C_2H_6$ and C_3H_6), and the element balance in gaseous products can be determined with the following equations:

Reactant conversion (%) = $C_i = (1 - \frac{X_i^{outlet} . X_{N_2}^{inlet}}{X_i^{inlet} . X_{N_2}^{outlet}}) \times 100$ (i =C_3H_8 or CO_2)

Fractional flow of gas in product (ml/min) = $F_j^{oulet} = \frac{X_j^{outlet} . F_{N_2}}{X_{N_2}^{outlet}}$

(j = $H_2, CO, CO_2, CH_4, C_2H_4, C_2H_6, C_3H_6, C_3H_8$)

Yield of Hydrocarbon (%) = $S_{C_nH_m} = \frac{n \times F_{C_nH_m}^{outlet}}{3 \times F_{C_3H_8}^{inlet}} \times 100$

Yield of CO (%) = $Y_{CO} = \frac{F_{CO}^{outlet}}{2 \times F_{CO_2}^{inlet}} \times 100$

Carbon-balance (%) = $B_C = \frac{F_{CH_4}^{outlet} + 2 \times F_{C_2H_4}^{outet} + 2 \times F_{C_2H_6}^{outlet} + 3 \times F_{C_3H_6}^{outlet} + 3 \times F_{C_3H_8}^{outlet} + F_{CO}^{outlet} + F_{CO_2}^{outlet}}{3 \times F_{C_3H_8}^{inlet} + F_{CO_2}^{inlet}} \times$ 100

Oxygen-balance (%) = $B_O = (\frac{2\times F_{CO_2}^{outlet} + F_{CO}^{outlet}}{2\times F_{CO_2}^{inlet}}) \times 100$

The calculated reactant conversion and product yield are generally used in catalytic process. The reactant conversion shows the percentage of reactant to be activated and converted when passing through the reactor, whilst the product yield shows the efficiency (in percentage) of target product formation by using a certain amount of reactant. In short, these two kinds of values can be respectively considered as indexes of reactivity and productivity in a process.

The product selectivity is another index used in catalytic process, which can be indirectly calculated using the following **(Eq.6.1**.). This equation shows a strong relationship among these three value, and the product selectivity is usually defined as the product formation from the converted reactant. The meaning of product selectivity calculation is to indicate the extent of the side reactions generating byproducts.

$$Product\ Selectivity = \frac{Product\ Yield}{Reactant\ Conversion} \times 100\% \ldots . \textbf{Eq.6.1.}$$

The element balance (carbon-balance and oxygen-balance) are also generally used in catalytic process, counting the mass change of oxygen and carbon elements through the reactions. The change of carbon-balance usually indicates the coke formation or the carbon species oxidation on the catalyst surface. The change of oxygen-balance usually indicates the H_2O generation (too small amount to be collected neither by GC nor by reactor cooling tower), and the reduction/oxidation of catalyst can also be hinted by this index.

6.2.3 Pre- and Post-Characterisation of Catalysts

In this chapter, the pre- and post- reaction catalysts were mainly characterised by Laser-Raman spectroscopy and Thermal Gravimetric Analysis (TGA) in different atmospheres, and the detailed characterisation methods outlined in Chapter 3.4.

6.3 Results and Discussion

6.3.1 The Existence of a $Cr(III) - Cr(VI)$ Redox Cycle

In order to prove the existence of the so-called redox cycle between $Cr(III)$ and $Cr(VI)$, TGA in different atmospheres and Laser-Raman spectroscopy were operated over Cr-based catalysts in different scenarios.

First of all, pure Cr_2O_3 was put into a CO_2 atmosphere to monitor the weight change. In principle, if Cr_2O_3 was oxidised, there would be a positive change in TGA profiles and negative value on Derivative-TGA (D-TGA) line, which is indicating a gain of weight. In Figure 6.2, apart from the major weight loss at the beginning of test (below 150℃) which was corresponding to the desorption of the catalyst moisture, only two weight losses (approximately 150-300℃ and 500-800℃) were observed. The amount of these two weight losses was tiny, which can almost be ignored, but decomposition of oxides with high Cr oxidation state can be neglected.

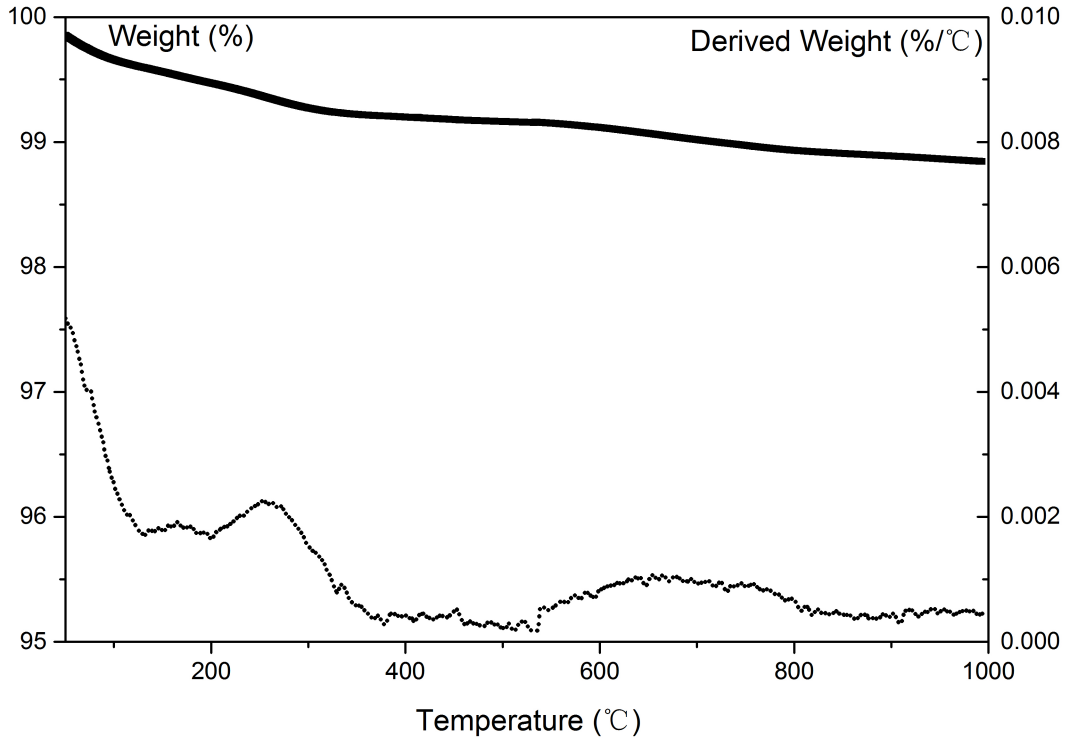

Figure 6.2: TGA (solid line) and D-TGA (dashed line) data of pure Cr_2O_3 in CO_2 atmosphere.

Figure 6.3 exhibits the TGA and D-TGA data of $5Cr/Zr$ in the atmospheres of CO_2 and N_2 respectively. The data shows negligible weight change. On D-TGA lines, all the data are above zero which means the material was losing its weight, rather than gaining, throughout the tests. Hence, we can conclude that $Cr(III)$ species cannot be oxidised in a CO_2 atmosphere. On the other hand, when temperature reaches to 550℃ or above, there are two wide, but clear bands indicating the weight loss of material, which may be corresponding to the decomposition of oxides at higher valent Cr to lower valent Cr, and if the correspondence of the CrO_x decomposition is true, It is reasonable to conclude from the results that the ZrO_2 support enhances formation of CrO_x (probably $Cr(VI)$ species) with higher thermal-stability (because the decomposition temperature was 500℃ and above).

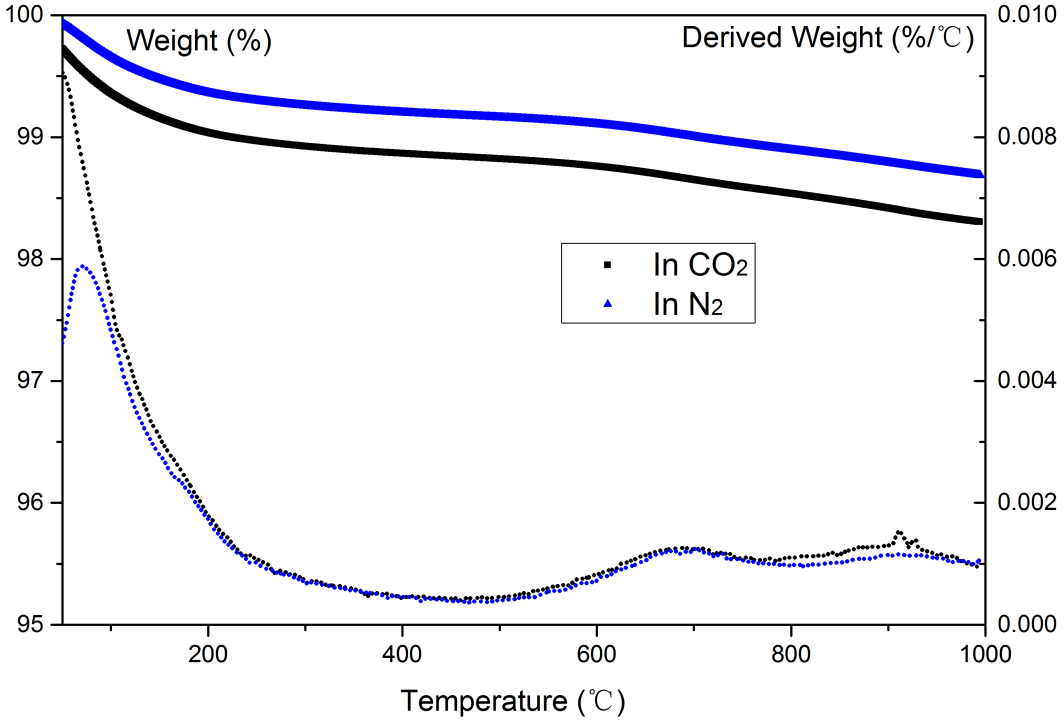

Figure 6.3: TGA (solid lines) and D-TGA (dotted lines) data of $5Cr/Zr$ in CO_2 or N_2 atmosphere.

Raman spectra as shown in Figure 6.4 may offer an explanation to the TGA results. From the spectra of pure Cr_2O_3, it is apparent that the Raman bands at $550cm^{-1}$ and $608cm^{-1}$ are belonging to Cr-O-Cr vibration of distorted octahedral chromium atoms in crystalline Cr_2O_3 [12, 13]. However, due to the overlap of bands between ZrO_2 and Cr_2O_3, these two bands can hardly be observed on ZrO_2-supported catalysts. Besides the multiple bands of ZrO_2 and crystalline Cr_2O_3 respectively, the most distinct band at $884cm^{-1}$ over fresh $5Cr/Zr$ was related to the $Cr(VI)$ species (V_{as} stretching mode of tetrahedral-symmetry chromate) [12], and the formation of chromate species was indicating a strong interrelationship between Cr_2O_3 and ZrO_2 support. The $884cm^{-1}$ band intensity over $5Cr/Zr$ after TGA in CO_2 was much weaker, which can be related to the loss of $Cr(VI)$

species due to the formation of Cr_2O_3 at high temperature during the TGA test. The weight loss after 550℃ can also be related to the decomposition of chromate species to lose oxygen atoms.

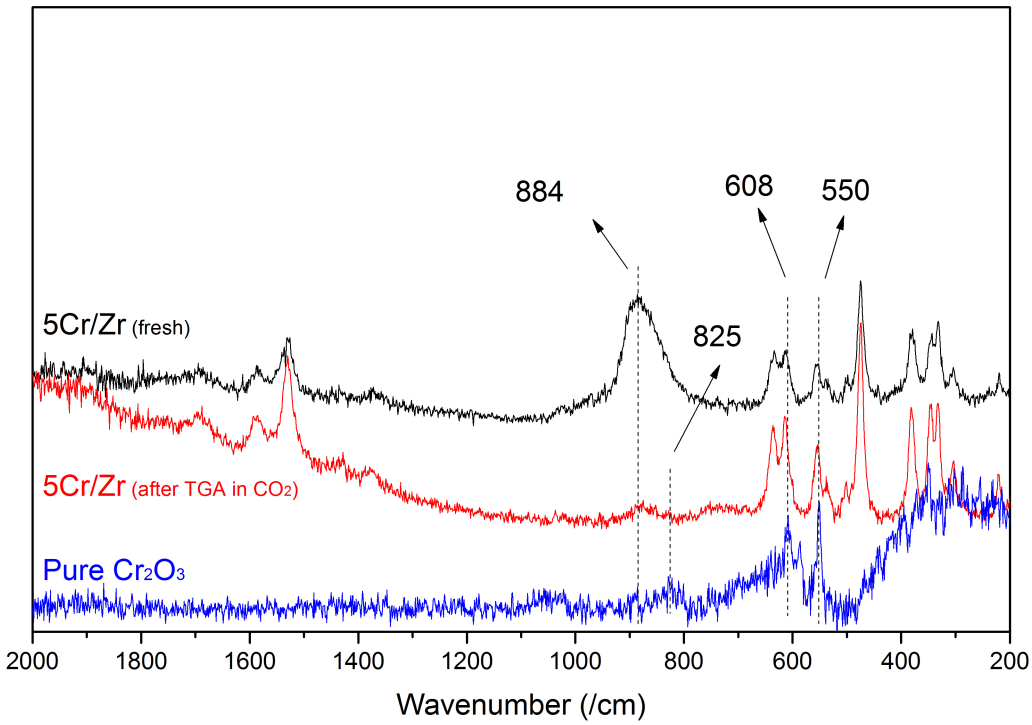

Figure 6.4: Raman spectra of pure Cr_2O_3 and 5Cr/Zr (before and after TGA) in CO_2 atmosphere.

According to previous studies [14, 15], $Cr(VI)$ species can mainly be formed by the interaction between Cr_2O_3 and support, and they claimed that the $Cr(VI)$ species can perform at higher activities during the DHP by CO_2 than Cr_2O_3. Moreover, $Cr(VI)$ species can only be formed with a good dispersion of Cr_2O_3 on the surface, and the $Cr(VI)$ formation will be reduced by increasing the doping level of Cr_2O_3, for instance, above $10wt\%$ of loading as discussed in the research paper. This finding can also be supported by our Raman data, as shown in Figure 6.5, and it is noticed that the $884cm^{-1}$ band over $10Cr/Zr$

had a lower intensity than the one over $5Cr/Zr$. Catalytic stability tests at 500℃ were also operated over these two catalysts (as shown in Table 6.3), and we can see that $10Cr/Zr$ had even a lower activity than $5Cr/Zr$, which can be assumed to derive from the more crystallisation of Cr_2O_3 with an increased doping level, and a decreased amount of $Cr(VI)$ formed as consequence.

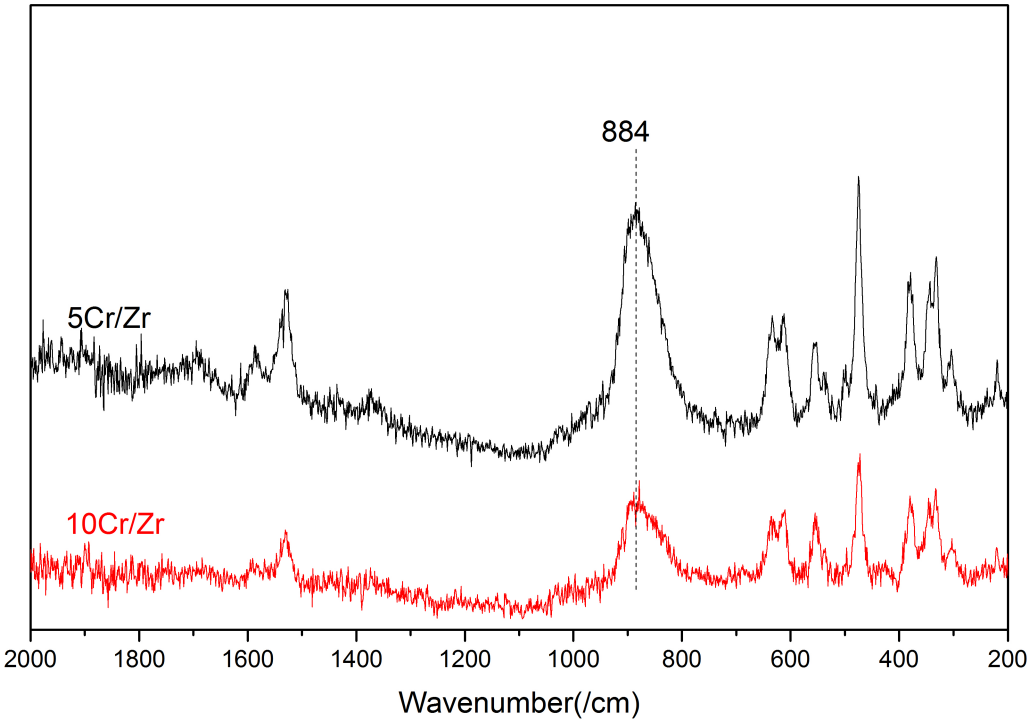

Figure 6.5: Raman spectra of 5Cr/Zr and 10Cr/Zr.

Table 6.3: Conversions of propane ($C_{C_3H_8}$), Selectivity of propylene ($S_{C_3H_6}$), conversions of CO_2 (C_{CO_2}) and selectivity of CO (S_{CO}) in the reaction of DHP by CO_2 over 5Cr/Zr and 10Cr/Zr. Conditions: 500℃, atmospheric pressure, 5-hour duration (the first measurement was taken at 1h after the reaction started), $C_3H_8 : CO_2 : N_2$=5%:10%:85%, $GHSV = 1.2 \times 10^4 ml \cdot h^{-1} \cdot g_{cat}^{-1}$). **To be noticed, the error due to the GC measurement is** ±2.0%

Sample	$C_{C_3H_8}$(%)		$S_{C_3H_6}$(%)		C_{CO_2}(%)		S_{CO}(%)	
Time on stream	60min	300min	60min	300min	60min	300min	60min	300min
5Cr/Zr	16	17	79	63	5	4	86	89
10Cr/Zr	15	16	72	64	4	6	86	88

In conclusion, we cannot prove the existence of a redox cycle between $Cr(VI)$and $Cr(III)$ species because no evidence of Cr_2O_3 oxidation was observed. However, we can observe that $Cr(VI)$ was actually formed through an interrelationship with catalyst support, and this species is the key to the higher performance of catalysts during the DHP by CO_2 process.

6.3.2 Reactions over ZrO_2-supported Cr-Based Catalysts with Surface Basicity Promotion

Figure 6.6 and Figure 6.7 show the performances of ZrO_2-supported rare-earth-doped catalysts in DHP by CO_2 process. With the conversion and selectivity of $5Cr/Zr$, it is apparent to observe that the promotional effects from rare-earth-doping on these two aspects are very little. $1La-5Cr/Zr$ (refer to Table 6.2) gives a relatively higher activity for propane conversion, but the yield of propylene is similar to others due to the relatively lower propylene selectivity ("Propylene Yield" equals to "Propane conversion" multiplied by "Propylene Selectivity").

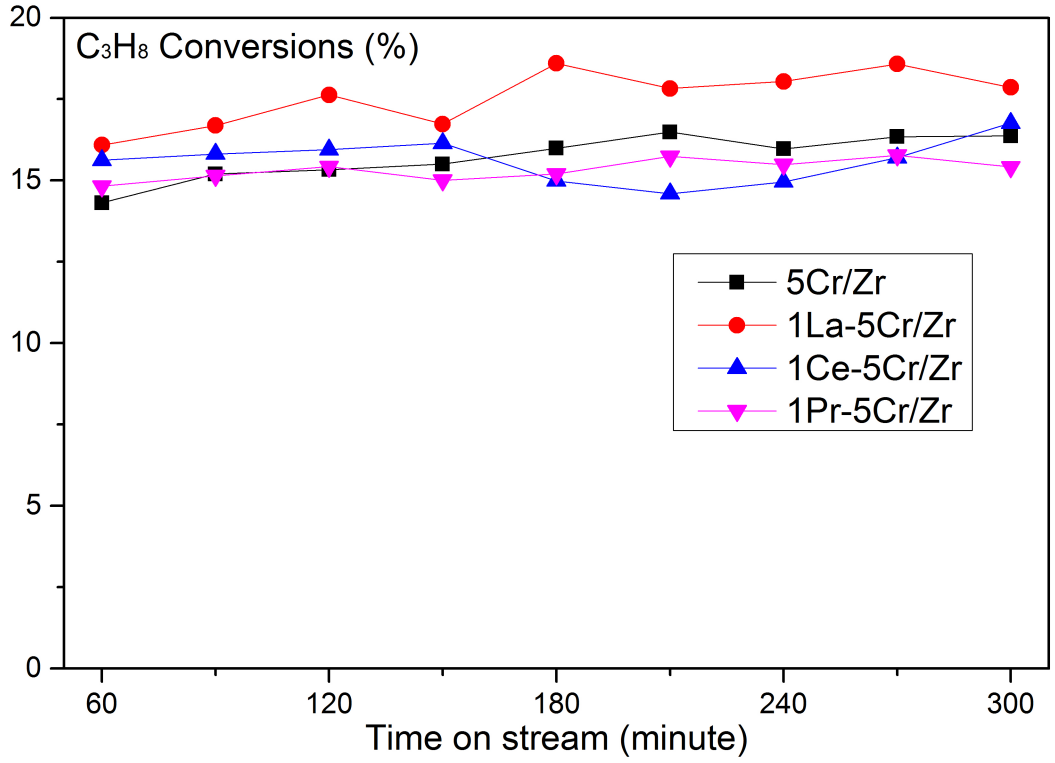

Figure 6.6: Propane conversions over the ZrO_2-supported rare-earth-doped catalysts (conditions: various temperature, atmospheric pressure, $C_3H_8 : CO_2 : N_2 = 5\% : 10\% : 85\%$, GHSV=$1.2\times10^4 ml \cdot h^{-1} \cdot g_{cat}^{-1}$).

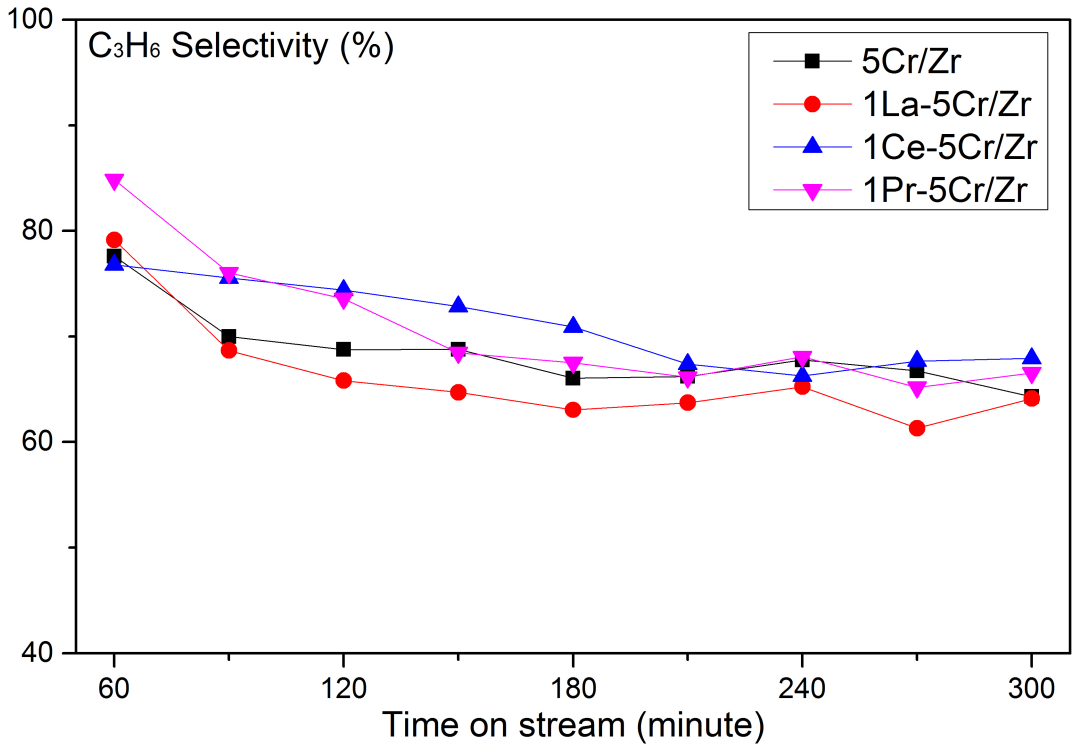

Figure 6.7: Propylene selectivity over the ZrO_2-supported rare-earth-doped catalysts(conditions: various temperature, atmospheric pressure, $C_3H_8 : CO_2 : N_2$ = 5% : 10% : 85%, GHSV=$1.2\times10^4 ml \cdot h^{-1} \cdot g_{cat}^{-1}$).

The propylene yields (~11%) over all the catalysts above were low because of the low propane conversions (~15%). To improve the conversions, the catalyst development is one way to go. Besides, according to the discussion in Chapter 4 (for Figure 4.12), the propane conversion can be improved when diluting the feedstock (propane and CO_2) more with N_2. Another method to improve propane conversion is adding a feedstock reflux, separating propane and CO_2 out from the outlet gas and flowing them back to the reactor. Aspen Plus software is capable to simulate this reflux when modelling the reactors and flows, which is worthy to be carried out in the future work.

However, our results were totally different when looking at CO_2 conversions over each catalyst (shown in Figure 6.8). With any form of rare-earth-doping, the consumption of

CO_2 increased to 2-3 times as much as over $5Cr/Zr$. The improved CO_2 consumption also indicated the real enhancement of the concept "CO_2 Activation and Utilisation", which is always emphasised by us.

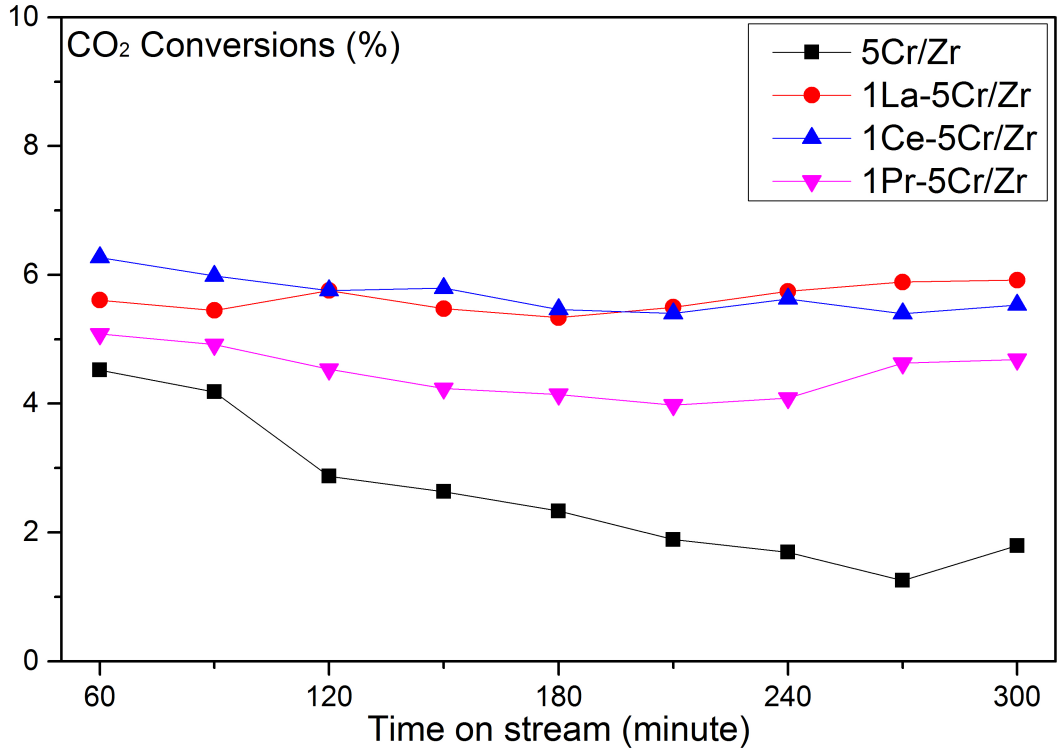

Figure 6.8: CO_2conversions over the ZrO_2-supported rare-earth-doped catalysts(conditions: various temperature, atmospheric pressure, $C_3H_8 : CO_2 : N_2 = 5\% : 10\% : 85\%$, GHSV=$1.2 \times 10^4 ml \cdot h^{-1} \cdot g_{cat}^{-1}$).

Importantly, the enhanced CO_2 utilisation by rare-earth-doping also led to a reduced degree of coking taking place on the catalyst surface. From the colour of spent catalysts as shown in Figure 6.9, the rare-earth-doped catalysts turned to gray rather than black as compared to $5Cr/Zr$, and this matches the TGA result in Figure 6.9 that the weight loss of $5Cr/Zr$ at 300℃ (corresponding to the combustion of coke species) was apparently larger than other rare-earth-promoted catalysts. Considering that the coking rate affects the stabilities of catalysts significantly, the rare-earth-doping will significantly enhance the

stabilities of catalysts over a long period of time, which is an important practical significance if industrial application is one of the ultimate goals of this research.

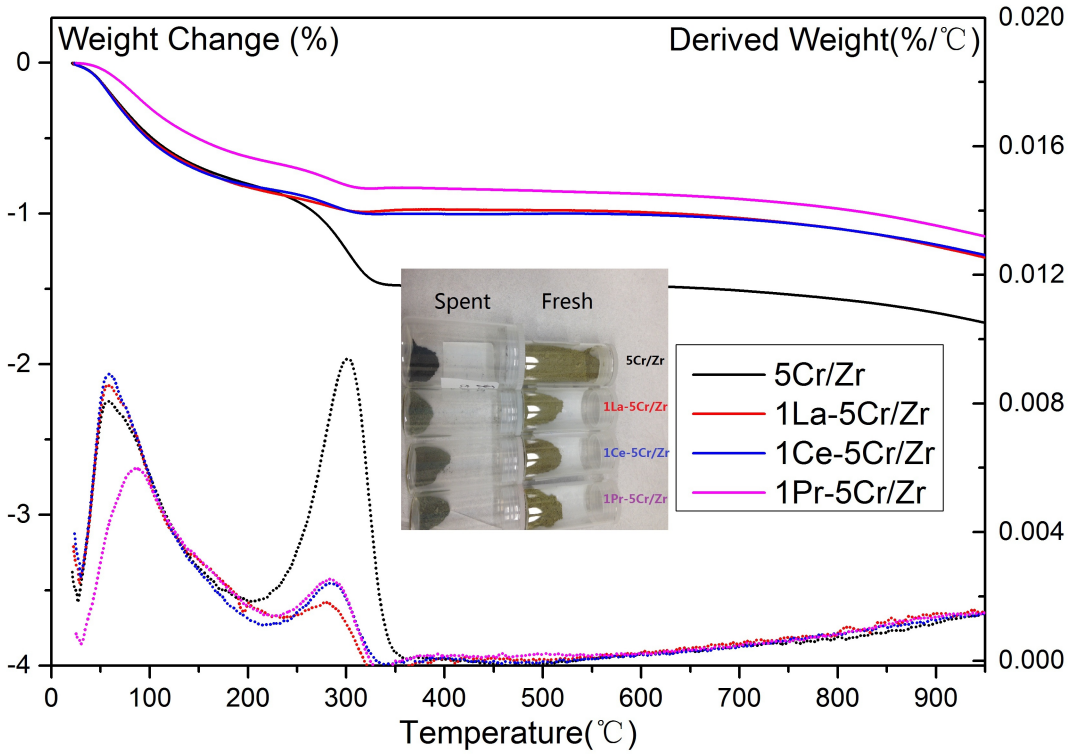

Figure 6.9: TGA (solid lines) and D-TGA (dotted lines) results of the post-reaction ZrO_2-supported rare-earth-doped catalysts. (measured in air)

6.3.2.1 Additional Discussion on Ce-Promoted Catalysts

Besides the theory of surface basicity, cerium oxide has the potential to be both an electron donor and acceptor as a redox cycle between $Ce(III)$ and $Ce(IV)$ [16]. So here we tried to dope CeO_2 in different ways:

a), together with Cr_2O_3, coded as "$1Ce-5Cr/Zr$";

b), before Cr_2O_3 to modify ZrO_2 support, coded as "$5Cr/1Ce-Zr$".

As shown in Table 6.4, by changing the doping order to modify ZrO_2 support (sample b), propane conversion were inhibited for a little bit while propylene selectivity was enhanced.

It is apparent that to mix Ce and Cr together can only improve the activation of propane but is not helpful to produce more propylene due to the relative lower selectivity.

Table 6.4: Propane Conversion ($C_{C_3H_8}$), propylene selectivity ($S_{C_3H_6}$) and propylene yield ($Y_{C_3H_6}$) over Ce-Cr based catalysts with different Ce-doping orders, (conditions: various temperature, atmospheric pressure, 5-hour duration (the first measurement was taken at 1h after the reaction started), $C_3H_8 : CO_2 : N_2 = 5\% : 10\% : 85\%$, GHSV=$1.2 \times 10^4 ml \cdot h^{-1} \cdot g_{cat}^{-1}$). **To be noticed, the error due to the GC measurement is** ±2.0%

Sample	$C_{C_3H_8}(\%)$		$S_{C_3H_6}(\%)$		$Y_{C_3H_6}(\%)$	
Time on stream	60min	300min	60min	300min	60min	300min
a, $1Ce-5Cr/Zr$	20	22	57	44	11	10
b, $5Cr/1Ce-Zr$	17	21	66	45	11	10

Laser-Raman spectroscopy was also used to check if any changes occurred over the catalyst surface during the reactions. In Figure 6.10, the mixture of Ce and Cr oxides led to a red-shift to of the Raman band which is corresponding to $Cr(VI)$ species from 889 to 879 cm^{-1}, and the $Cr(VI)$ band shifted more (to $869 cm^{-1}$) when CeO_2 was doped before Cr_2O_3 on catalyst surface. This difference indicated that the Ce-Cr mixed oxides were formed at different levels. However, after 5-hour time on stream, $Cr(VI)$ bands of both catalysts were red-shift to $851 cm^{-1}$, which probably suggests that Ce-Cr mixed oxides were dissociated to separated Cr and Ce oxides. On the other hand, no evidence can be observed to prove the existence of $Ce(III)$ or $Ce(IV)$ both before and after reaction, and this is probably due to the very low loading of Ce oxides. Hence, the enhancement of Ce via the redox cycle between $Ce(III)$ and $Ce(IV)$ cannot be validated from our Laser-Raman data.

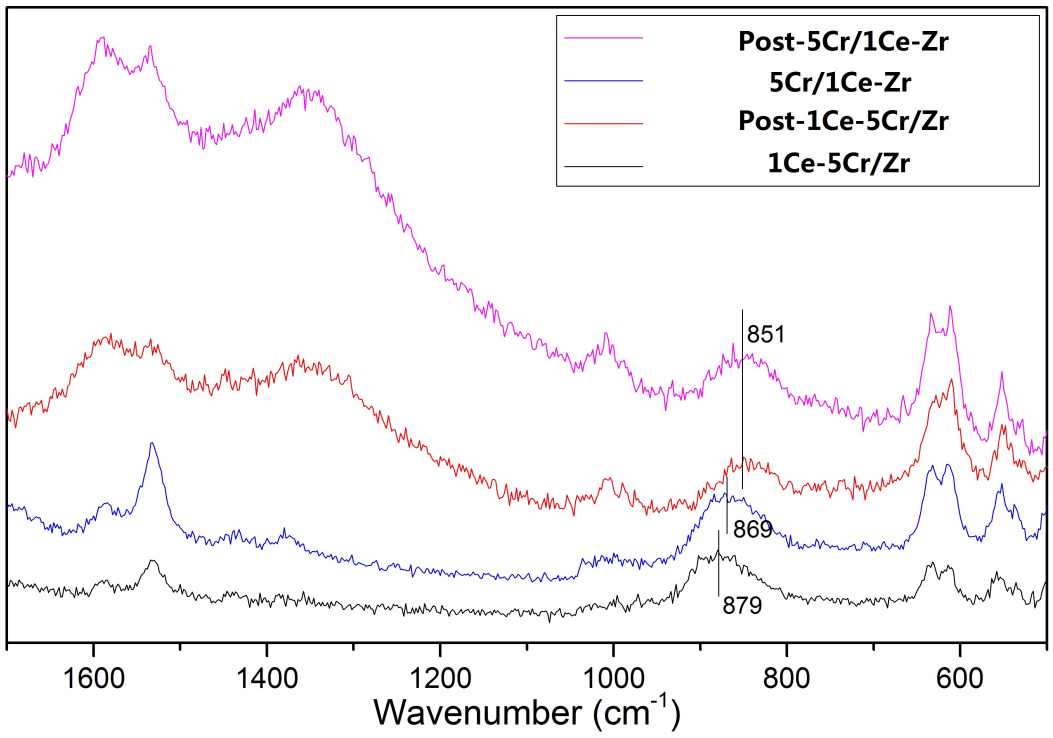

Figure 6.10: Raman spectra of Ce-Crbased catalysts with different doping orders.

Yet, the red-shift of $Cr(VI)$ band from $870cm^{-1}$ to $850cm^{-1}$ cannot confirm the reduction of $Cr(VI)$ to $Cr(III)$. The band shift was caused by a change of laser power when operating Laser-Raman. On fresh catalysts, its easy for the laser beam to access the Cr species dispersed on the surface; however on spent catalysts, the generated coke species fully cover the catalyst surface. To quickly eliminate surface coke, a higher power of laser beam was used to "burn" carbon species (displayed as a bright spot under the camera in Figure 6.11), and the band was shifted as a result. To see the band shift (or the shift of band shape), fresh $5Cr/Zr$ was characterised by different level of laser power in Raman spectroscopy (Figure 6.11), and the shift was reversible when switching laser power between these two stages.

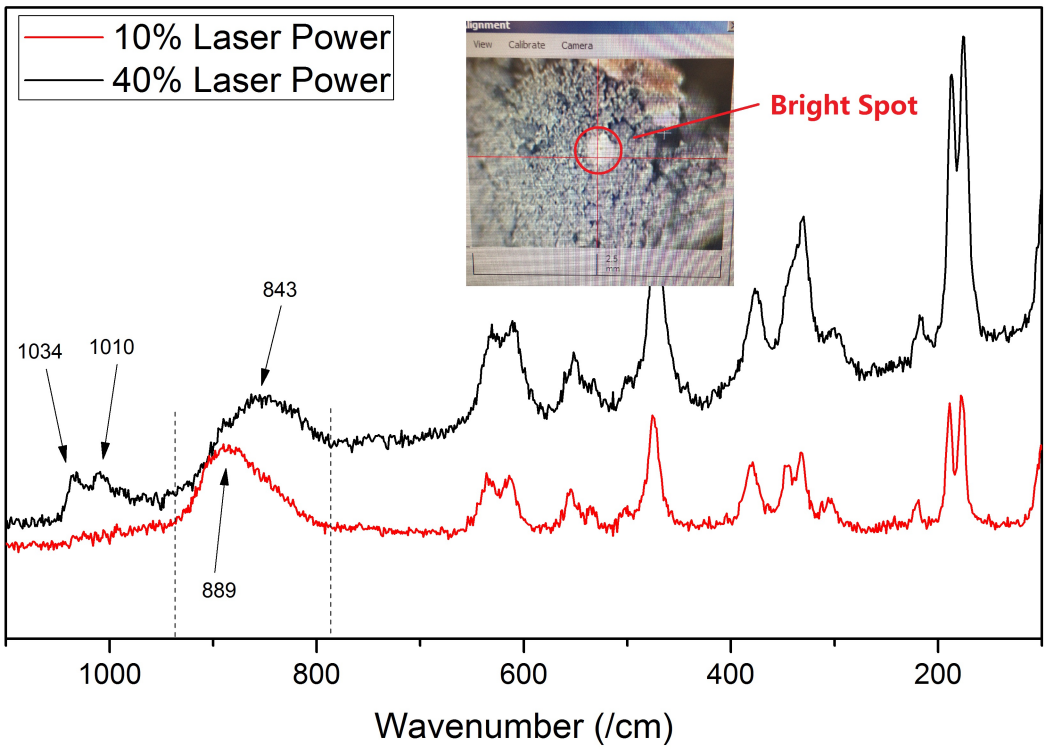

Figure 6.11: Raman spectra of $5Cr/Zr$ with different levels of laser power.

6.3.2.2 The Effect of Alkali Metal Oxide Doping on the Catalyst Performance

Compared to the rare-earth doping which moderately modifies the surface basicity of Cr-based catalysts, alkali metal oxides such as K_2O and Na_2O might give much stronger changes on the catalyst surface. In an attempt to explore the catalyst performance with stronger surface basicity, two catalysts with K_2O and Na_2O doping (coded as $1K-5Cr/Zr$ and $1Na-5Cr/Zr$) have been prepared and studied.

The results showed extremely low conversions of propane, which were below 5% over both catalysts, and these numbers were smaller than systematic errors that allowed when operating with micro-reactors (we regarded "no more than 5% difference" as reproducible). However, the detrimental effect of alkali metal oxides was apparent. The lack of activity

of these two catalysts can be attributed to these strongly basic additives which "killed" the acid sites on the surface.

As a summary of this section, we can see that both acidic and basic sites are critically important to the catalyst performance. The existence of acid sites determines the adsorption and activation of propane, which is absolutely the precondition of any other catalytic performances. Surface basicity helps to attract and consume CO_2, which not only makes this reaction more suitable for "CO_2 Utilisation" , but can also diminish the formation of coke species to enhance the lifetime of catalyst; however, too strongly basic additives will damage the acid sites on surface. Thus, *both* mild acidity and basicity should be controlled and balanced precisely.

6.3.3 Reactions over $5Cr/Zr$ When the Mixed-flow of Feedstock Changed

A series of DHP by CO_2 reactions were carried out over the consistent catalyst $5Cr/Zr$ but under different mixed-flows of feedstock. The flow was modified as shown in Table 6.5. To be noticed, "R-4800" was the reference reaction carried out under the same conditions described in Chapter 6.2.2, and the overall GHSV was set at $4800 ml \cdot h^{-1} \cdot g_{cat}^{-1}$. To shorten the average time for C_3H_8 molecules to stay on catalyst surface, the GHSV of $C_3H_8$was decreased by increasing the proportion of $C_3H_8 (X_{C_3H_8})$ in "R-4800×2" and "R-4800×3"; whilst the GHSV of $C_3H_8$was lifted up to the same value by increasing the overall GHSV (accelerate the flow of feedstock) in "R-9600" and "R-14400".

Table 6.5: Mole fractions of C_3H_8 ($X_{C_3H_8}$), overall GHSV and C_3H_8 GHSV of the coded reactions.

Reaction code	$X_{C_3H_8}$ $(mol\%)$	GHSV $(ml \cdot h^{-1} \cdot g_{cat}^{-1})$	GHSV of C_3H_8 $(ml \cdot h^{-1} \cdot g_{cat}^{-1})$
R-4800	5	4800	240
R-4800×2	10	4800	480
R-4800×3	15	4800	720
R-9600	5	9600	480
R-14400	5	14400	720

The C_3H_8 conversion and C_3H_6 selectivity of the reaction under different C_3H_8 partial pressures and overall GHSV are shown in Figure 6.12. The results reveal effective C_3H_8 conversions at each specified condition while the C_3H_6 selectivity drops at the beginning of reactions. The results with different mole fractions of C_3H_8 were displayed with solid symbols and the conclusion drawn from the data in these figures is an inhibition of C_3H_8 conversion, but also an improvement in C_3H_6 selectivity. However, with the same increase of C_3H_8 fractional GHSV (by increasing the overall GHSV), the C_3H_8 conversion was inhibited to a similar extent while the C_3H_6 selectivity also decreased. These comparative results indicate that even though the C_3H_8 conversion was similarly inhibited by the two routes to increase the C_3H_8 fractional GHSV, the underpinning mechanisms were fundamentally different.

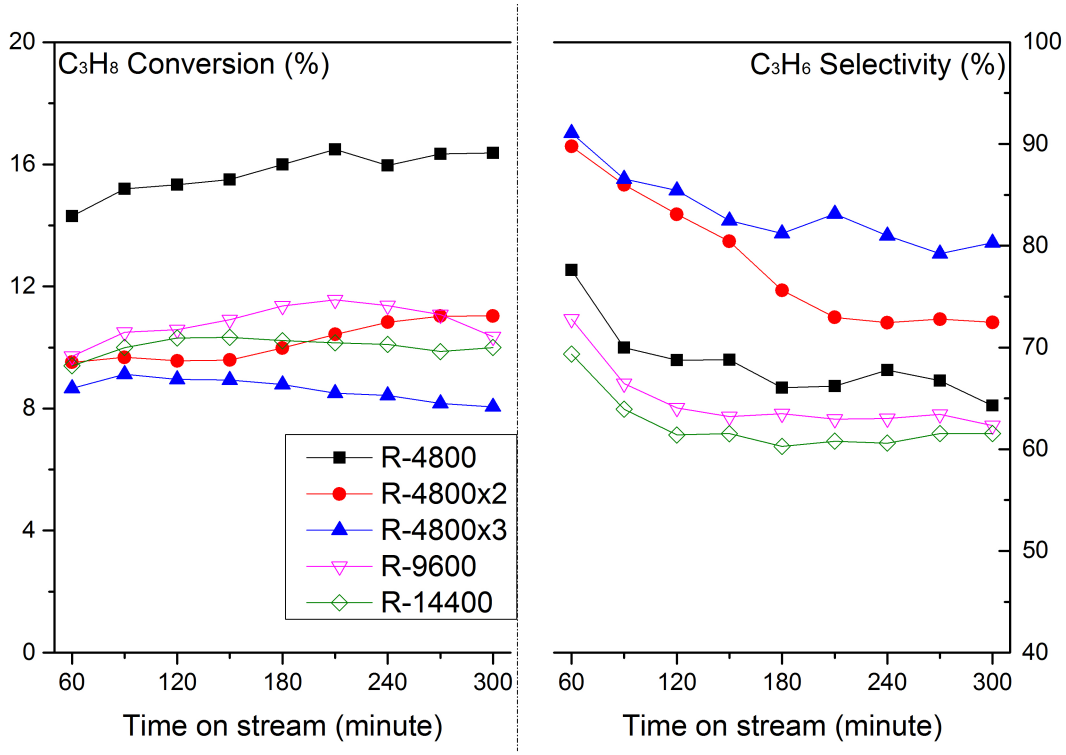

Figure 6.12: C_3H_8conversion and C_3H_6 selectivity over 5wt%-Cr_2O_3/ZrO_2 upon operation time at various C_3H_8 partial pressure and overall GHSV; 500℃ and C_3H_8/CO_2 = 0.5.

Figure 6.13 exhibits the production of CH_4, the main by-product. The initial selectivity of CH_4 was decreased from 6% to 3% as an increase of C_3H_8 fractional GHSV. The CH_4 selectivity can roughly indicate the cracking capability of catalyst on higher level hydrocarbons, which indirectly exhibits the extent of further cracking effect on C_3H_6 during the reaction.

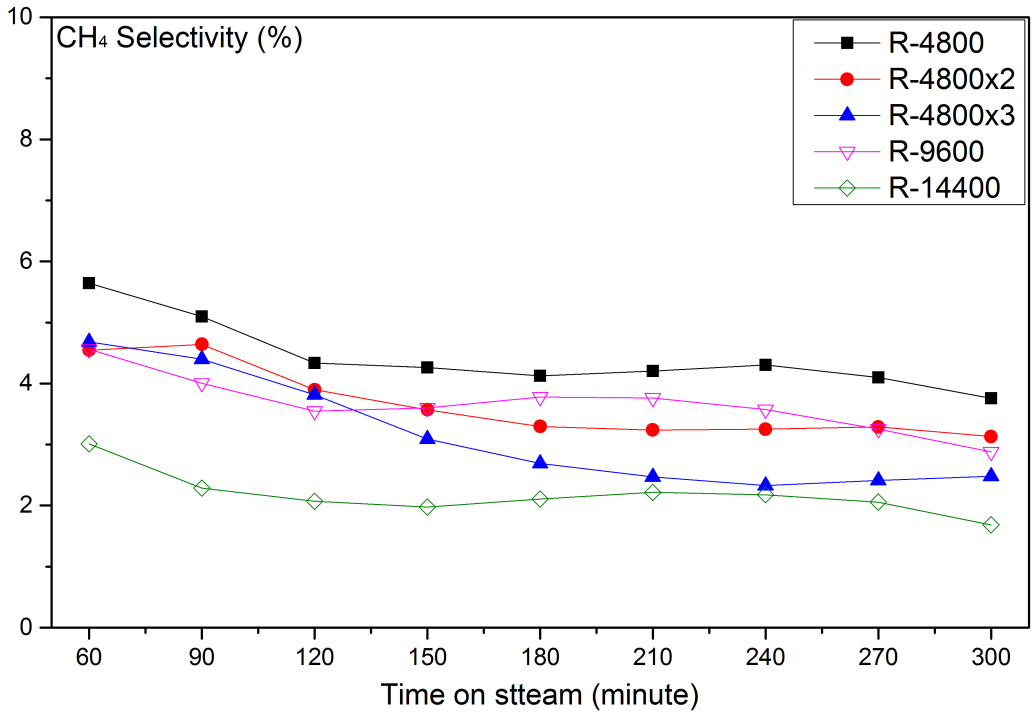

Figure 6.13: Dependence of the CH_4 selectivity with time on stream over 5wt%-Cr_2O_3/ZrO_2 at various C_3H_8 partial pressures and overall GHSV; 500°C and $C_3H_8/CO_2 = 0.5$.

6.3.3.1 On the Changes of C_3H_6 Selectivity

The conversion of reactants and the mass balances of carbon and oxygen elements are shown in Table 6.6. In contrast to the high stability of the C_3H_8 conversion, the CO_2 conversions dropped drastically over the first 5 hours. This may be due to the various and different sites for C_3H_8 and CO_2 to be adsorbed on the catalyst surface respectively; C_3H_8 is usually

attached to Cr species while CO_2 can be adsorbed at the interface between Cr_2O_3 dopant and ZrO_2 support [17]. The high level of $C-$Balance indicates the low generation of solid and liquid $C-$containing product; this confirms the high stability of C_3H_8 conversions in each test. The $O-$balance, which was higher than 100% during the test, indicates additional, extraneous oxygen must have entered into the gaseous phase during the reaction, and the oxygen source can be attributed to the reduction of high valance state chromium species (Cr^{6+}/Cr^{5+}) on the catalyst surface [18]. Weckhuysen et al. claimed that Cr^{6+} plays as a precursor for the Cr dehydrogenation centres, and the reduction of Cr species is assumed to be one of the primary deactivation mechanisms [15].

Table 6.6: Conversion of reactants ($C_{C_3H_8}$,C_{CO_2}) and balance of elements (B_C,B_O) in gaseous products over 5wt%-Cr_2O_3/ZrO_2 at various C_3H_8 partial pressure and overall GHSV; 500℃ and C_3H_8 is 1:2. **To be noticed, the error due to the GC measurement is** ±2.0%.

Reaction code	$C_{C_3H_8}$(%)		C_{CO_2}(%)		B_C(%)		B_O(%)	
	60min	300min	60min	300min	60min	300min	60min	300min
R-4800	14	16	5	2	99	99	107	104
R-4800×2	10	11	3	3	100	99	104	103
R-4800×3	9	8	3	2	100	100	103	101
R-9600	10	10	4	2	99	99	103	102
R-14400	9	10	2	1	99	99	103	102

Table 6.7 is a compilation of the yields and the selectivity of gaseous products. The reduced level of C_2H_x production as compared to that of the selectivity of CH_4 was observed). This experimental trend matched the prediction (highlighted in Figure 4.10) that CH_4 is much more difficult to be thermally cracked at 500℃ than corresponding C_2 molecules. The decrease of CO yield was not as much as the trend of CO_2 conversion; we believe this is due to the carbon gasification reducing the chromium species (Cr^{6+}/Cr^{5+}) on catalyst the surface, which matches the observed increasing $O-$balance.

Table 6.7: Yield of CO (Y_{CO}) and Selectivity of hydrocarbons (S_i) over 5wt%-Cr_2O_3/ZrO_2 at various C_3H_8 partial pressure and overall GHSV; 500℃ and C_3H_8/CO_2 = 0.5. **To be noticed, the error due to the GC measurement is** ±2.0%

Reaction code	Y_{CO}(%)		S_{CH_4}(%)		$S_{C_2H_X}$(%)		$S_{C_3H_6}$(%)	
	60min	300min	60min	300min	60min	300min	60min	300min
R-4800	4	4	6	4	2	1	78	64
R-4800×2	2	2	5	3	2	1	90	72
R-4800×3	2	2	5	2	2	2	92	80
R-9600	2	2	5	3	2	1	73	62
R-14400	2	2	3	2	1	1	70	62

The XRD patterns of 5wt%-Cr_2O_3/ZrO_2 before and after the catalytic tests are displayed in Figure 6.14, and the pattern of the ZrO_2 support is also shown here as reference. The peak at 2θ=36.18° corresponds to the 1-1-0 reflection group of Cr_2O_3 with rhombohedral crystal symmetry. No peak shift or new peaks were observed from the post-reaction catalyst, which indicated that no phase change occurred during the catalytic test. Importantly, this also matched the high stability of C_3H_8 conversions, as shown in Figure 6.12.

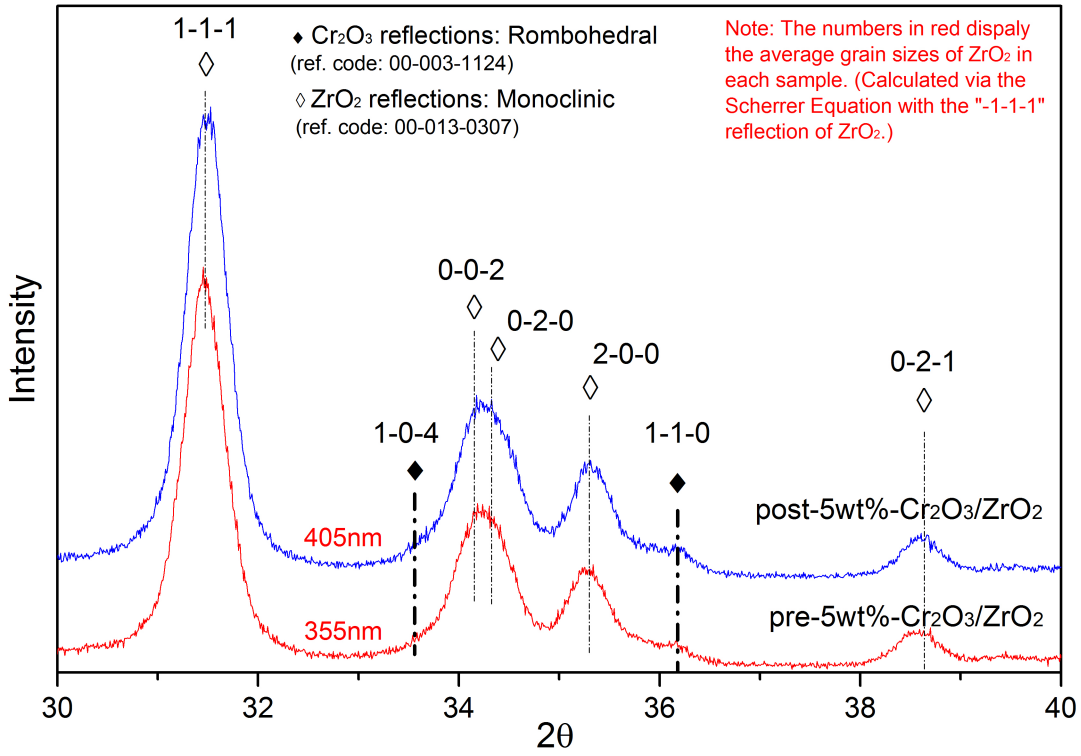

Figure 6.14: X-ray Diffraction (XRD) results over the catalysts both before (pre-5wt%-Cr_2O_3/ZrO_2) and after (post-5wt%-Cr_2O_3/ZrO_2) the catalytic tests.

TGA results and the corresponding Derivative-TGA (D-TGA) plots are displayed in Figure 6.15. The weight losses at 200-355℃ were attributed to the combustion of amorphous carbon in air. The integrated area of the derivative weight equals to the weight loss, which displayed more coke formed with an increase in the C_3H_8 fractional GHSV.

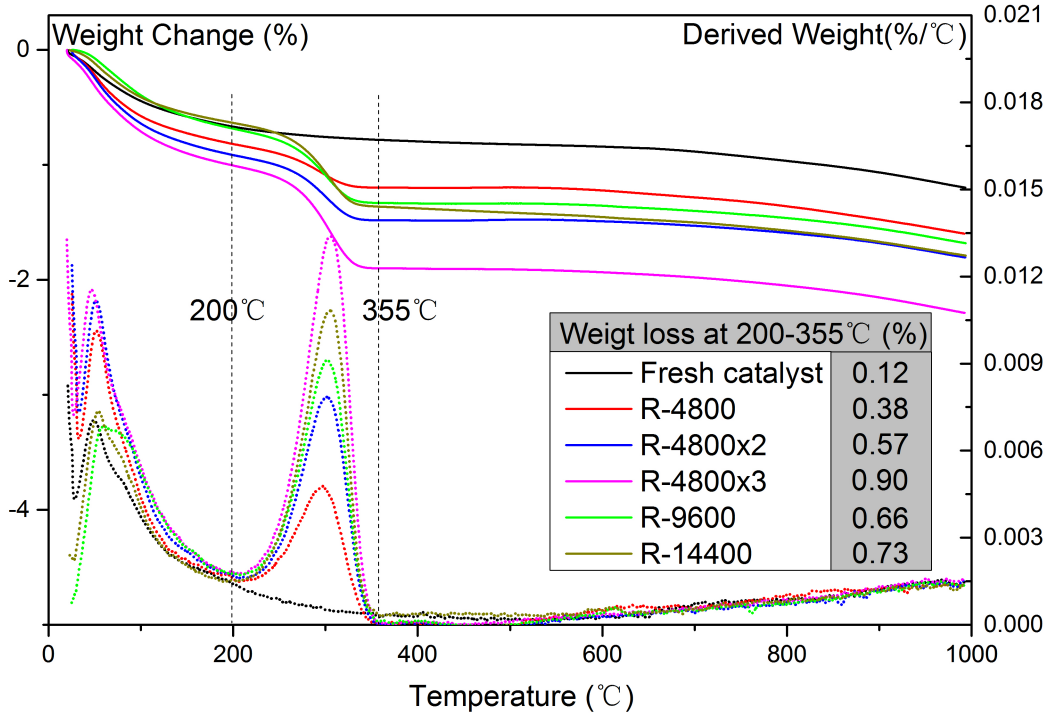

Figure 6.15: TGA (solid lines) and D-TGA (dot lines) results over 5wt%-Cr_2O_3/ZrO_2 at various C_3H_8 partial pressure and overall GHSV; 500℃ and $C_3H_8/CO_2 = 0.5$.

In general terms, the mechanism of DHP by CO_2 process involves the primary activation of C_3H_8 on the catalyst surface, while CO_2 provides a contribution to the reaction equilibrium shift by oxidising H_2 generated from the C_3H_8 dehydrogenation (via the RWGS). From the macro perspective, the average residence time for each C_3H_8 molecule is shortened with the higher C_3H_8 fractional GHSV, and this is the cause of a decreased C_3H_8 conversion by optimising both methods to modify the C_3H_8 fractional GHSV. However, the observed changes of C_3H_6 selectivity indicate that only increasing the partial pressure of reactants can effectively inhibit the further cracking of C_3H_6. This is because the competitive adsorption between C_3H_6 and other substances are strengthened from the micro perspective.

6.3.3.2 A "Dilemma Situation": Competition between Conversion and Selectivity

It is apparent that an acceptable (observable) conversion is the precondition for us to discuss any other kind of performance. However, we sometimes sacrifice a bit of reactivity (interpreted as conversion) to enhance the low selectivity of target products. It is also not difficult to be understood because high selectivity means less by-product generated from another point of view. Just like the DHP by CO_2 process, the dilemma between high conversion and high selectivity often occurs in the reaction system where side-reactions are much more thermodynamically favoured than the target sub-reactions. With an easier way to recognise them, this kind of reactions usually have the target products which are still very reactive under the set conditions. For instance, C_3H_6 is much more reactive than C_3H_8 at 500℃ as referred to the Figure 4.10, which mean a precisely controlled residence time of reactant on catalyst surface is needed.

Real world industrial applications give us an reasonable resolution to this dilemma situation between conversion and selectivity, which is to recycle the inactivated feedstock back to the input pipeline. This recycling design can reach to very high selectivity while save the reactants if they are not cheap, and hopefully we can do it in lab as a further study.

6.4 Conclusions

In this chapter, the reaction of the DHP by CO_2 was discussed from both the aspects of catalyst variety and the influence from process conditions.

Above all, TGA in various kinds of atmosphere and Laser-Raman spectroscopy were applied to check if the redox cycle between $Cr(VI)$ and $Cr(III)$ exists during the catalytic tests. The results suggested that $Cr(VI)$ species was formed but unfortunately cannot prove

the re-oxidation in CO_2 atmosphere if $Cr(VI)$ species was reduced to $Cr(III)$. Despite this, like the formation of $Cr(VI)$ species had strong links with the doping level of Cr_2O_3 on support, and the amount of generated $Cr(VI)$ species had more influence on catalyst's performance than the change of Cr_2O_3 doping level, which is in agreement with the conclusion of Michorczyk et al. [14] Based on the studies on the Cr_2O_3 oxide catalyst itself, we set ZrO_2-supported Cr-based oxide as the reference catalyst, and all other additives were used as potential promoters for this general catalyst.

In order to modify $5Cr/Zr$ from the perspective of surface acidity and basicity, different kinds of rare-earth-doping were introduced. With a improvement of CO_2 chemisorption via surface basicity enhancement, the coke formation was massively inhibited while almost no negative effects on propane conversions and propylene selectivity can be observed. The increased coke resistance can be attributed to the improved CO_2 utilisation, and this will highly stabilize the performance of catalyst in long term reactions. Some additional tests over K and Na added catalysts were carried out, and the poor activation of propane implies both the optimal surface basicity and surface should never be comprised with surface acidity. In another words, the type of critical "balance" is important for ultimate catalyst performance.

From the aspect of reacting conditions, a series of catalytic tests were carried out over $5Cr/Zr$ at various C_3H_8 partial pressure by changing the mixed-flow of feedstock. It was shown that the increase of C_3H_8 partial pressure is highly beneficial for the enhancement of C_3H_6 selectivity. Meanwhile, the C_3H_8 conversion was sacrificed due to the competitive adsorption between the produced C_3H_6 and inactivated C_3H_8 molecules, which was the major reason for inhibition of further cracking of C_3H_6. As a comparison, the increase of the overall GHSV can also decrease the C_3H_8 conversion to the similar extent. However, the further cracking of C_3H_6 cannot be limited because only the residence time of C_3H_8 on the catalyst surface was shortened from this micro perspective.

For the ultimate implementation of this particular CO_2 utilisation processes, we believe that the enhancement of selectivity of the (target) C_3H_6 product, whilst sacrificing some of the reactants' ultimate conversion is acceptable. The efficiency can be improved by a cyclic system involving the reuse of the unconverted feedstock by separating from the outlet mixture and subsequently cycling back to the inlet mixture. It is recognised that this kind of cyclic system is beneficial to the reactions with low conversion but very high selectivity. The high thermo-stability of the present catalyst makes it attractive to scale-up to a moving bed or even a fluid bed reactor for catalyst regeneration.

Bibliography

[1] R. Wu, P. Xie, Y. Cheng, Y. Yue, S. Gu, W. Yang, C. Miao, W. Hua, and Z. Gao. Hydrothermally Prepared Cr2O3-ZrO2 as a Novel Efficient Catalyst for Dehydrogenation of Propane with CO2. *Catalysis Communications*, 39:20–23, 2013.

[2] D. B. Fox, E. H. Lee, and M.-H Rei. Carbon Dioxide as Hydrogen Acceptor in Dehydrogenation of Alkanes. *Industrial and Engineering Chemistry, Product Research and Development*, 11:444–446, 1972.

[3] P. Michorczyk and J. Ogonowski. Dehydrogenation of Propane in the Presence of Carbon Dioxide over Oxide-Sased Catalysts. *Reaction Kinetics and Catalysis Letters*, 78(1):41–47, 2003.

[4] K. Takehira, Y. Ohishi, T. Shishido, T. Kawabata, K. Takaki, Q. Zhang, and Y. Wang. Behavior of Active Sites on Cr-MCM-41 Catalysts during the Dehydrogenation of Propane with CO2. *Journal of Catalysis*, 224(2):404–416, 2004.

[5] M. Chen, J.-L. Wu, Y.-M. Liu, Y. Cao, L. Guo, H.-Y. He, and K.-N. Fan. Study in Support Effect of In2O3/MOx (M=Al,Si,Zr) Catalysts for Dehydrogenation of Propane in the Presence of CO2. *Applied Catalysis A: General*, 407(1-2):20–28, 2011.

[6] P. Michorczyk, P. Kuśtrowski, A. Kolak, and M. Zimowska. Ordered Mesoporous Ga2O3 and Ga2O3-Al2O3 Prepared by Nanocasting as Effective Catalysts for Propane Dehydrogenation in the Presence of CO2. *Catalysis Communications*, 35:95–100, 2013.

[7] T. Shishido, K. Shimamura, K. Teramura, and T. Tanaka. Role of CO2 in Dehydrogenation of Propane over Cr-based Catalysts. *Catalysis Today*, 185(1):151–156, 2012.

[8] B. Xu, B. Zheng, W. Hua, Y. Yue, and Z. Gao. Support effect in Dehydrogenation of Propane in the Presence of CO2 over Supported Gallium Oxide Catalysts. *Journal of Catalysis*, 239:470–477, 2006.

[9] M. M. Bettahar, G. Costentin, L. Savary, and J. C. Lavalley. On the Partial Oxidation of Propane and Propylene on Mixed Metal Oxide Catalysts. *Applied Catalysis A: General*, 145:1–48, 1996.

[10] J. Zhang and D. He. Surface Properties of Cu/La2O3 and Its Catalytic Performance in the Synthesis of Glycerol Carbonate and Monoacetin from Glycerol and Carbon Dioxide. *Journal of Colloid and Interface Science*, 419:31–38, 2014.

[11] Y. C. Wong, Y. P. Tan, Y. H. Taufiq-Yap, I. Ramli, and H. S. Tee. Biodiesel Production via Transesterification of Palm Oil by Using CaO-CeO2 Mixed Oxide Catalysts. *Fuel*, 162:288–293, 2015.

[12] M. A. Vuurman, D. J. Stufkens, A. Oskam, J. A. Moulijn, and F. Kapteijn. Raman Spectra of Chromium Oxide Species in CrO3/A12O3 Catalysts. *Journal of Molecular Catalysis*, 60:83–98, 1990.

[13] M. A. Vuurman, F. D. Hardcastle, and I. E. Wachs. Characterization of CrO3/Al2O3 Catalysts under Ambient Conditions: Influence of Coverage and Calcination Temperature. *Journal of Molecular Catalysis*, 84(2):193–205, 1993.

[14] P. Michorczyk, P. Pietrzyk, and J. Ogonowski. Preparation and Characterization of SBA-1-Supported Chromium Oxide Catalysts for CO2 Assisted Dehydrogenation of Propane. *Microporous and Mesoporous Materials*, 161:56–66, 2012.

[15] B. M. Weckhuysen and R. A. Schoonheydt. Alkane Dehydrogenation over Supported Chromium Oxide Catalysts. *Catalysis Today*, 51(2):223–232, 1999.

[16] A. R. S. Darujati and W. J. Thomson. Stability of Supported and Promoted-Molybdenum Carbide Catalysts in Dry-Methane Reforming. *Applied Catalysis A: General*, 296(2):139–147, 2005.

[17] S. Naito, M. Tsuji, and T. Miyao. Mechanistic Difference of the CO2 Reforming of CH4 over Unsupported and Zirconia Supported Molybdenum Carbide Catalysts. *Catalysis Today*, 77(3):161–165, 2002.

[18] S. Deng, S. Li, H. Li, and Y. Zhang. Oxidative Dehydrogenation of Ethane to Ethylene with CO2 over Fe-Cr/ZrO2 Catalysts. *Industrial & Engineering Chemistry Research*, 48(3):7561–7566, 2009.

Chapter 7

Summary and Outlook

7.1 Dry Methane Reforming (DMR)

By impregnating Co atoms into the Mo_2C lattice, the performance of catalysts in DMR was highly enhanced from all aspects. Besides, the resistance to the oxidation effect from CO_2 was highly improved, which might lead to much longer lifetime for the bi-metallic catalysts. Hence he most important achievement is to prepare catalysts without applying any noble metals, whilst the catalyst performance, both in reactivity and stability, is comparable to the noble metal catalysts as reported by other researchers. Hence, it is worthy to carry out long-term study in this catalyst series to see the lifetime performance. Moreover, the catalyst performance can be carried out in a larger experimental scale, which is an essential step towards industrialisation.

The thermodynamic calculations for single reactions and multi-reaction combinations (using Aspen Plus software) were carried out to compare the DMR with the steam methane reforming (SMR) which is currently the major route of H_2 production in industry. From the results, we can conclude that DMR has more potential to reach higher CH_4 conversions at the conditions for SMR in real world condition, strongly support the possible usage of

flue-gas in a tri- methane reforming (TMR) to be fulfilled.

When taking a further outlook for the future, TMR has the great potential to be a major solution to CO_2 emission problem. As displayed in Figure 7.1, when TMR and the downstream syn-gas reactions (to produce hydrocarbons) are linked, carbon will be cycled as medium between renewable energy and combustion engines, and the released CO_2 from fossil fuels will be much inhibited.

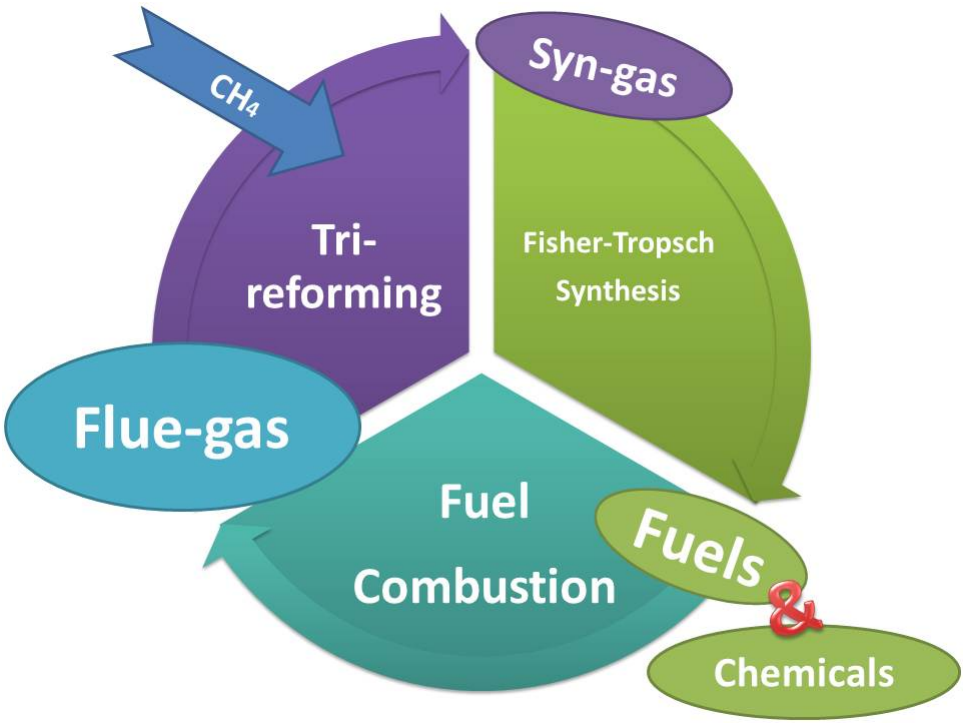

Figure 7.1: Schematic diagram of carbon element to be cycled among TMR, FTS and fuel combustion.

7.2 Dehydrogenation of Propane by CO_2 (DHP by CO_2)

From the overview, the Cr-based catalysts showed low C_3H_8 conversions and continuously decreasing C_3H_6 selectivity. However, by changing the adsorption/attachment of reactants, the competitive adsorption from CO_2 was found to be highly influential the C_3H_8 conversion

and inhibit the further cracking of C_3H_6, which effectively enhanced the selectivity of the target product. This conclusion gives new perspective on judging the merits and demerits of the competitive adsorption phenomena, which is different to the viewpoints from other researchers who only attribute the reactivity inhibition to competitive adsorption. In future work, the feedstock reflux is expected to be effective in improving the yield of C_3H_6 without producing more by-products, and this will be a valuable direction to study with the help of the powerful Aspen Plus software.

In catalyst development for the DHP by CO_2 process, the rare-earth additives resulted in the higher conversions of CO_2 are due to the increased basicity of catalyst from rare-earth promoters. The enhanced CO_2 conversion also inhibited the coke formation on catalyst surface, which would lengthen the lifetime of catalysts.

The thermodynamic calculation results using Aspen Plus software gave a better motivation to the DHP by CO_2 research. The much lower temperature requirement (less than 500℃) made it possible to operate this process under an energy source of sunlight (solar thermal heating). On the other hand, the different results between thermodynamic calculations (for the DHP by CO_2 process) and the practical catalytic tests indicated the huge gap between the thermodynamic potentials and the real world.

Comparing to DMR, the process DHP by CO_2 requires much lower temperature which means it has higher possibility to be conducted by solar thermal heating energy. From my research, it can be concluded that the DHP by CO_2 process has a balanced performance (between reactivity and selectivity) at the temperature level (~500℃) for solar thermal heating to supply continuous and stable energy. Furthermore, the production of propylene in this process is targeted towards the polymer industry, which will be a permanent sequestration of CO_2.

7.3 Future Challenges

From my work, it is mostly criticized that the "catalytic results" and "thermodynamic discussions" are not closely linked. Although I have the argument that "the reaction potentials calculated thermodynamically can roughly guide us to carry out the reactions at an optimal set of conditions", the practical results are often far away from the thermodynamic expectations because it always takes much longer time to reach the equilibrium state in the real world. We must accept that the thermodynamic calculation results illustrate the maximum limit of a reaction extent - no kinetic theory can offer any further help if a reaction has reached to equilibrium. However, if the equilibrium state is still far away in reality due to the slow reaction rate, the kinetic studies would be much more useful if we are still trying to accelerate reactions with catalysts.

The doping level of catalyst on the support surface would be more discussed. It is worthy to turn to small loading of promoters or doping level (such as 0.1-0.5wt.%) on catalysts, which will lead to the diversity of catalyst performance. This study can give further insight into the importance of promoter-support interaction over catalyst performance.

Lifetime tests of catalysts clearly need to be carried out in future work. In industry, in certain cases the stability of a catalyst is more important than the activity – it affects the frequency to pause the reactors in order to change catalysts and/or the types of reactors (fixed-bed, moving-bed or fluid-bed) should be installed. Before industrialisation, it is essential to carry out the catalyst evaluations under normal operation conditions for a long period (1-2 weeks) and then asses its regeneration after a second stability test.

Chapter 8

Appendix: Calibration and Sensitivity Data for Gas Chromatograph (GC)

The calibration of GC is in essence to confirm the relationship between the signals (integration area figures) from a GC detector (FID/TCD, see Chapter 3.3.2) and the actual proportions (in vol.%) of gases in a gas mixture. All the compositions of gases, shown in this thesis, were measured by a fixed GC equipment (PerkinElmer, Clarus 580 GC). The calibration method for data output precision is outlined as follows.

To keep the composition stability of the gas flow resources, the pure-gas cylinders (for H_2, CO_2, N_2 and CH_4) and the gas-mixture cylinders (for H_2, CO, CO_2, N_2, CH_4, C_2H_4, C_2H_6, C_3H_6, andC_3H_8 at various diluting levels) are purchased form BOC (from Linde Group). All the gas compositions (in vol.%) of these standard-gas cylinders had been precisely measured by the manufacturer (Special Gases of BOC) before the purchase and shipment. From these cylinders, various composition figures for each gas substance are

achieved directly. The measuring ranges for all substances are listed in Table A.1 by showing the highest and the lowest proportion in measurements.

Table 8.1: The measuring ranges for H_2, CO, CO_2, N_2, CH_4, C_2H_4, C_2H_6, C_3H_6, andC_3H_8.

Substance	Lowest Proportion (vol.%)	Highest Proportion (vol.%)
H_2	10.0	100.0
CO	10.0	50.0
CO_2	10.0	100.0
N_2	50.0	100.0
CH_4	4.76	100.0
C_2H_4	2.30	4.99
C_2H_6	2.35	5.09
C_3H_6	2.26	9.98
C_3H_8	2.30	4.97

When measuring the standard-gas cylinders in GC, the columns, the detectors and the equipment setting parameters were the same as the description in Chapter 3.2.2. The results achieved from measurements are in the form of integration area of the peaks at the retention time with respect to the substances. Then for every substance, there was an integration area (y) curve on the function of volume proportion in gas mixture (shown in Table A.2). These curves were usually regressed to proportional functions if the received variances were at high levels ($r^2 \geq 0.9998$). Sometimes, the curves are not straight cross the origin occasionally, which resulting to the received variances lower than 0.9998. In such situations, the curves were regressed as quadratic or even cubic functions with 0 intercepts in pursuing of high variances.

Table 8.2: Integration area (y) curves on the function of volume proportions (x, in vol.%) with function variances (r^2) for H_2, CO, CO_2, N_2, CH_4, C_2H_4, C_2H_6, C_3H_6, andC_3H_8 in GC calibrations.

Substance	$y = f(x)$	r^2
H_2	$y = 65233.66x - 81.340952x^2$	0.999825
CO	$y = 86955.76x - 73.6347x^2 + 0.272014x^3$	0.999971
CO_2	$y = 76379.3395x$	0.999923
N_2	$y = 74190.52x$	0.999965
CH_4	$y = 77178.79x$	0.999893
C_2H_4	$y = 149642.17x$	0.999894
C_2H_6	$y = 150228.16x$	0.999912
C_3H_6	$y = 223200.64x$	0.999954
C_3H_8	$y = 221181.45x$	0.999998